FERMILAB-THESIS-1996-80

# A Measurement of the Lepton Charge Asymmetry in $W$ Decays Produced in $p\overline{p}$ Collisions at $\sqrt{s} = 1.8$ TeV

by

Qun Fan

Submitted in Partial Fulfillment
of the
Requirements for the Degree
Doctor of Philosophy

Supervised by Professor Arie Bodek
Department of Physics and Astronomy
The College of Arts and Science

University of Rochester
Rochester, New York

1996

## Curriculum Vitae

The author was born in Tian-Chang, Anhui Province, China on February 27, 1965. He graduated with a Bachelor of Science Degree in Precision Mechanical Engineering in 1986 from the University of Science and Technology of China (USTC). He subsequently entered the graduate program in Particle Physics at the Institute of High Energy Physics, Beijing, China, where he participated in the building of the BES spectrometer. He began working on the L3 experiment at CERN in May 1989 supported by a fellowship from the World Laboratory. In the fall of 1991, he was admitted to the University of Rochester where he started working on the CDF experiment as a graduate student. He received his M.A. degree in May 1989 from IHEP Beijing and in May 1993 from University of Rochester. He finished his Ph.D work under the supervision of Prof. Arie Bodek in December of 1996.

# Abstract

We describe a measurement of the charge asymmetry as a function of lepton rapidity in $W \rightarrow \mu\nu, e\nu$ produced in $p\overline{p}$ collisions at $\sqrt{s} = 1.8$ TeV. The data sample collected by the CDF detector during 1992-1995 consists of $\approx 110k$ events corresponding to $\approx 111$ $pb^{-1}$ of integrated luminosity. This is a five-fold increase in statistics over the previous analysis [1]. A new analysis technique using silicon tracking in conjunction with shower centroid determination is used to extend the measurement to higher lepton rapidity up to $|y_l| = 2.4$. In addition, the forward muon detector yields data at $1.9 < |y_l| < 2.5$. The substantial reduction in the errors and the large increase in the kinematic range have greatly improved the discriminating power over various proton structure functions. The asymmetry data constrain the slope of ratio of the $d/u$ quark momentum distributions in the proton over the $x$ range 0.006 and 0.34 at $Q^2 \approx M_W^2$. Although the data in the central region are reproduced by modern parton distributions, there are differences in the high rapidity regions, which imply that further tuning of the the slope of $d/u$ versus x is required.

# Acknowledgements

The work described in this thesis is the product of team work. It is only possible through the collaboration wide efforts. The maintenance and operation of this giant, complex detector, the collection of data, the verification of data qualities, and the data reconstruction, none of which could be accomplished so successfully without the group of dedicated people on CDF and those of the Fermilab Accelerator Division. All of the people involved have my sincere thanks.

My deepest thanks go to my adviser Prof. Arie Bodek, who provided constant support and encouragement throughout the course of this thesis. His expertise in this field enabled him to see the potential of hadron collider data in understanding proton's structure. This thesis is a direct result of his vision.

I thank Prof. Young-kee Kim and Dr. Larry Nodulman for being fine conveners of the CDF electroweak physics group during the course of this thesis. I am thankful to Drs. Howard Budd and Willis Sakumoto for many discussions about plug part of this analysis. I should give credit to Prof. Alan Sill who suggested that I look at the SVX to complement plug electron tracking in the CTC. This became the starting point of a CTC-less charge determination of plug electrons. Dr. David Stuart has my thanks for getting me familiar with the SVX data reconstruction. I thank Dr. Peter Berge for taking an interest in tracking at high pseudo-rapidities.

I would like to thank all members of Rochester CDF Run II Plug Upgrade group, Pawel de Barbaro, Howard Budd, Willis Sakumoto, Phillip Koehn and Manoj Pillai for sharing the excitement in meeting technical challenges from working with tiles and fibers. This has been my valuable experiences.

I thank Drs. Howard Budd, Takashi Asakawa, and Yasuo Fukui for working together to maintain the plug EM calorimeter and sharing the PEM pager during

the period of 1994-1995 (Tevatron Run 1B) CDF data-taking.

I thank Andrew Gordon and Doug Glenzinski for working together on Run 1B electroweak datasets and data quality monitoring.

My sweet memories of days of working at IHEP Beijing on BES main drift chamber are entirely due to Prof. Ji-mao Ma. He introduced me to this exciting field and believed that I should go abroad to have more experiences.

I thank Prof. Antonio Zichichi and the World Laboratory for giving me the fellowship during the period of my work on the L3 experiment. I am grateful to Prof. Ulrich Becker who always believed in my abilities while I was working in the L3 muon chambers working group, to Prof. Bolek Wyslouch for the help during my final days at CERN.

# Contents

# List of Tables

# List of Figures

# Chapter 1

# Introduction

Particle physics involves studies of the fundamental constituents of matter and nature of interactions between them. Four types of known fundamental interactions between particles exist. These are the electromagnetic, weak, strong and gravitational interactions. The gravitational force between fundamental particles is much weaker in magnitude compared with that of the other three types of forces that it does not contribute significantly to ordinary particle processes. Currently, the collection of theories describing the other three types of interactions between particles is known as the Standard Model. According to the Standard Model, all matter is constructed from leptons and quarks which interact via exchange of gauge bosons. The leptons and quarks have 1/2 unit of spin and are called fermions while the gauge bosons are spin 1 particles. Table 1.1 lists the fundamental particles of the Standard Model. Among theories of the Standard Model, the Quantum Chromodynamics (QCD) describes the strong interaction between quarks. The Quantum Electrodynamics (QED) describes the electromagnetic interaction. The Glashow-Weinberg-Salam theory of electroweak processes is a theory that describes the unification of electromagnetic and weak interactions. Together, these form our

| Fundamental Particles | | | | |
|---|---|---|---|---|
| Fermions | | | | Bosons |
| Quarks | Q ($\lvert e \rvert$) | Leptons | Q ($\lvert e \rvert$) | $W^{\pm}, Z^{o}, \gamma$, |
| **u c t** | +2/3 | $\nu_{\mathrm{e}}$ $\nu_{\mu}$ $\nu_{\tau}$ | 0 | 8 gluons (g) |
| **d s b** | −1/3 | **e** $\mu$ $\tau$ | −1 | Higgs (H) |
| • Quarks and gluons carry color (R,G,B)<br>• Leptons, $W^{\pm}$,$Z^{o}$, $\gamma$ are colorless<br>• The quarks and leptons also have antiparticle counterparts | | | | |

Table 1.1: The fundamental particles of the Standard Model grouped by generation. Only the existence of the Higgs boson remain in doubt.

current understanding of basic interactions between fundamental particles.

Like any other successful theories of nature, the theories of particle physics have always been driven by experimental results. Experimental research is carried out in a variety of experiments designed to test our understanding of matter and to capture new phenomena. Over the years, the results of increasingly more accurate measurements continue to confirm the predictions of the Standard Model. The early *ep* deep inelastic scattering experiments (DIS) in 1970 at Stanford Linear Accelerator Center (SLAC) established the existence of structure in the proton. The recent discovery of the Top quark at Fermilab concluded the long journey of the verification of the existence of all leptons and quarks in Table 1.1. A little over a decade after their experimental discoveries at CERN, tens of thousands of $W$ bosons and millions of $Z$ bosons have been produced. Today, these data samples become the testing ground of precision studies of the Standard Model predictions. The existence of gluons is best illustrated by the process of $e^+e^- \rightarrow$ *three jets* events at high center-of-mass energies, where the third jet comes from the Bremsstrahlung gluon from either final state $q$ or $\overline{q}$. There are a great deal of experimental evidence for the color degree of freedom of three colors in the quarks and gluons. If the Pauli Principle is to be maintained for baryons like $\Delta^{++}(uuu)$, an additional degree of freedom is needed in order to antisymmetrize the wavefunction for these three identical fermions. The experimental cross section for producing lepton pairs in hadron collisions (the Drell-Yan process) is consistent with the prediction of quark-antiquark annihilation when a factor of 1/3 is included in the cross section formulae. The measured $\pi^o$ lifetime agrees with the calculation of $\pi^o \rightarrow quark\ loop \rightarrow \gamma\gamma$ if there are three quark colors. Though the Higgs particle, whose existence is required to explain the origin of mass of particles, is yet to be found, the picture of particle physics has never been more complete. It is accurate to say that the standard model, although not believed to be the ultimate theory of particle physics, is built on the basis of overwhelming experimental evidence.

The study of particle physics requires the use of high energy particle accelerators. The interactions between higher energy particles probe structures at smaller distance scale. New particles, whose existence is usually excluded below some mass level, can only be produced at higher center-of-mass energy. Hadron colliders have been at the energy frontier during the past decades. Fermilab's Tevatron collider is currently world's highest energy $p\overline{p}$ collider at $\sqrt{s} = 1.8$ TeV. The next generation of hadron collider, the Large Hadron Collider (LHC) at CERN, will be colliding protons and anti-protons at $\sqrt{s} = 14$ TeV sometimes after year 2005. For these $p\overline{p}$ experiments and other experiments that involve hadrons in the initial state, experimentalists need to use parton distribution functions (PDFs) to calculate the cross sections of all physical processes. The PDFs are parameterized distributions of momentum densities of constituent quarks and gluons in a hadron. Typically these distributions are measured from deep inelastic experiments where a high energy lepton ($e$,$\mu$ or $\nu$) scatters off a nuclear target. This thesis describes study of PDFs using $W$ bosons produced in the $p\overline{p}$ collisions at the Tevatron Collider.

## 1.1 The Hadronic $W$ Production and its Leptonic Decay

Before the recent turn-on of the LEP2 run at CERN with $e^+e^-$ center-of-mass energy of 161 GeV, $W$ bosons have been produced only in hadron colliders. In a $p\overline{p}$ collider at Tevatron energy ($\sqrt{s} = 1.8$ TeV), $W$ bosons are produced mainly by quark anti-quark annihilations. Contributions from valence-valence and valence-sea annihilations amounts to about 85% of the cross section [2] with the rest from sea-sea quark-antiquark annihilations.

At $\sqrt{s} = 1.8$ TeV, $W$ bosons are mainly produced by the annihilation of $u$ and $d$ quarks. At the lowest order, the differential cross section of $W^+$ bosons in $p\overline{p}$ collisions can be described in the following,

$$\frac{d\sigma}{dy}(p\overline{p} \to W^+X) = K(y)\frac{2\pi G_F}{3\sqrt{2}}x_1x_2\{cos^2\theta_c[u(x_1)d(x_2) + \overline{d}(x_1)\overline{u}(x_2)]$$

$$+sin^2\theta_c[u(x_1)s(x_2) + \overline{s}(x_1)\overline{u}(x_2)]\},$$

where $y$ is the rapidity of the $W$ (defined as $y = ln\frac{E+P_z}{E-P_z}$), $\theta_c$ is the Cabibbo mixing angle, $G_F$ is the weak coupling constant. The partons from the proton (antiproton) carry momentum fraction $x_1$ ($x_2$). The $u(x)$, $d(x)$ and $s(x)$ are all evaluated at $Q^2 = M_W^2$. Here the $K(y)$ factor includes first order QCD correction to the cross section,

$$K \approx 1 + \frac{8\pi}{9}\alpha_s(M_W^2),$$

similar to $K$ factor in the Drell-Yan process.

At lowest order and from direct momentum and energy conservation, $x_1$ and

$x_2$ satisfy the following relationships:

$$x_1 x_2 = \frac{M_W^2}{s}$$

and

$$x_1 - x_2 = x_W,$$

which yield:

$$x_{1,2} = \frac{M_W}{\sqrt{s}} e^{\pm y}.$$

This indicates that the momentum fraction of $u$ and $d$ quarks are related to the rapidity of produced $W$'s.

In a hadron collider, $W$ bosons are primarily reconstructed from $W \rightarrow \mu\nu$ or $e\nu$ leptonic decays. The $W \rightarrow q\overline{q}$ hadronic decay is usually buried inside large QCD background ($p\overline{p} \rightarrow jets$), as are the $\tau$'s in $W \rightarrow \tau\nu$ process. As shown in Figure 1.1, $W$ bosons produced at $p\overline{p}$ collisions in leading order (LO) are polarized in the $\overline{p}$ direction. In the $W$ rest frame, the differential cross section for the process $u\overline{d} \rightarrow l^+\nu$ can be written as:

$$\frac{d\hat{\sigma}}{d\cos\hat{\theta}} = \frac{|V_{ud}|^2}{8\pi} \left( \frac{G_F M_W^2}{\sqrt{2}} \right)^2 \frac{\hat{s}(1 + \cos\hat{\theta})^2}{(\hat{s} - M_W^2)^2 + (\Gamma_W M_W)^2},$$

where $\hat{s}$ is the subprocess kinematic invariant $\hat{s} = (u + \overline{d})^2$, $\hat{\theta}$ is the angle between the $\overline{d}$ and the $l^+$ (in the $W$ rest frame), $V_{ud}$ is the CKM matrix element and $\Gamma_W$ is the $W$ width. In a hadron collider, the longitudinal momentum of the neutrino from the $W$ decay is not measured. At Tevatron energies, the constraint $M_W^2 = (E_l + E_\nu)^2 - (\vec{P}_l + \vec{P}_\nu)^2$ does not result in single solutions. The four momentum of $W$ can not be determined. Therefore, it is not possible to work in the $W$ rest frame. In terms of the pseudorapidity of the $W^+$ decay lepton

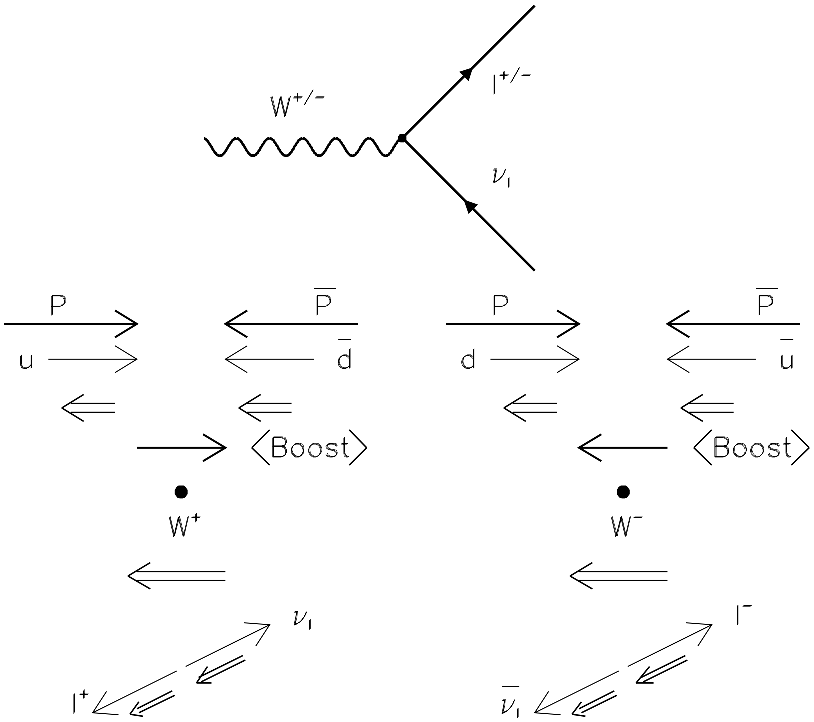

Figure 1.1: $W^{\pm} \to l^{\pm}\nu$. Arrows represent momenta and double arrows represent helicities (spin in the case of the $W$).

$(y_l \equiv 1/2 \ln \frac{|\vec{P}|+P_z}{|\vec{P}|-P_z} = -\ln tan(1/2\hat{\theta})$ in the lab frame, the angular distribution is:

$$\frac{d\sigma^{+}(\eta_l)}{d\eta_l} = 1/3 \int_0^1 dx_1 \int_0^1 dx_2 \{cos^2\theta_c[u(x_1)d(x_2) + \overline{d}(x_1)\overline{u}(x_2)]$$

$$+sin^2\theta_c[u(x_1)s(x_2) + \overline{s}(x_1)\overline{u}(x_2)]\} \left[\frac{d\hat{\sigma}}{d\cos\hat{\theta}} \sin^2\hat{\theta}\right],$$

where $\eta_l$ is related to $\hat{\theta}$, $x_1$ and $x_2$ by:

$$eta_l = -\ln\tan(\frac{\hat{\theta}}{2}) + \frac{1}{2}\ln(x_1/x_2).$$

Therefore, the lepton pseudo-rapidity measured in the lab frame is the sum of the pseudo-rapidity due to the V-A decay of the $W$ and the rapidity of the $W$ boson production.

## 1.2 The $W$ Charge Asymmetries

At Tevatron energies, $W^+$ ($W^-$) bosons are produced in $p\overline{p}$ collisions primarily by the annihilation of $u$ ($d$) quarks in the proton and $\overline{d}$ ($\overline{u}$) quarks in the antiproton. Because $u$ quarks carry on average more momentum than $d$ quarks, the $W^+$'s tend to follow the direction of the incoming proton and the $W^-$'s that of the antiproton. Therefore, a $W$ production charge asymmetry exists. Figure 1.2 shows the $W^+$ and $W^-$ rapidity distributions from ResBos [5] Monte Carlo simulation of $p\overline{p}$ collision at $\sqrt{s} = 1.8$ TeV.

We define the $W$ Production Charge Asymmetry as:

$$A(y_W) \equiv \frac{\sigma_W^+(y) - \sigma_W^-(y)}{\sigma_W^+(y) + \sigma_W^-(y)},$$

where $\sigma_W^\pm(y)$ is the cross section for $W^+$ or $W^-$ as a function of $W$ rapidity. We utilize the fact that $W^+$ ($W^-$) bosons are primarily produced by the annihilation of $u$ and $d$ quarks and take an approximation of $\sigma_W(y) \propto ud$.

$$A(y_W) \approx \frac{u(x_1)d(x_2) - u(x_2)d(x_1)}{u(x_1)d(x_2) + u(x_2)d(x_1)}$$

$$\equiv \frac{d(x_2)/u(x_2) - d(x_1)/u(x_1)}{d(x_2)/u(x_2) + d(x_1)/u(x_1)}.$$

It is clear that $A(y_w)$ is related to the slope of the $d/u$ ratio at high $Q^2$ and in the $x$ region of $W$ production at Tevatron.

Because the rapidity of $W$ bosons is not experimentally measured, we measure

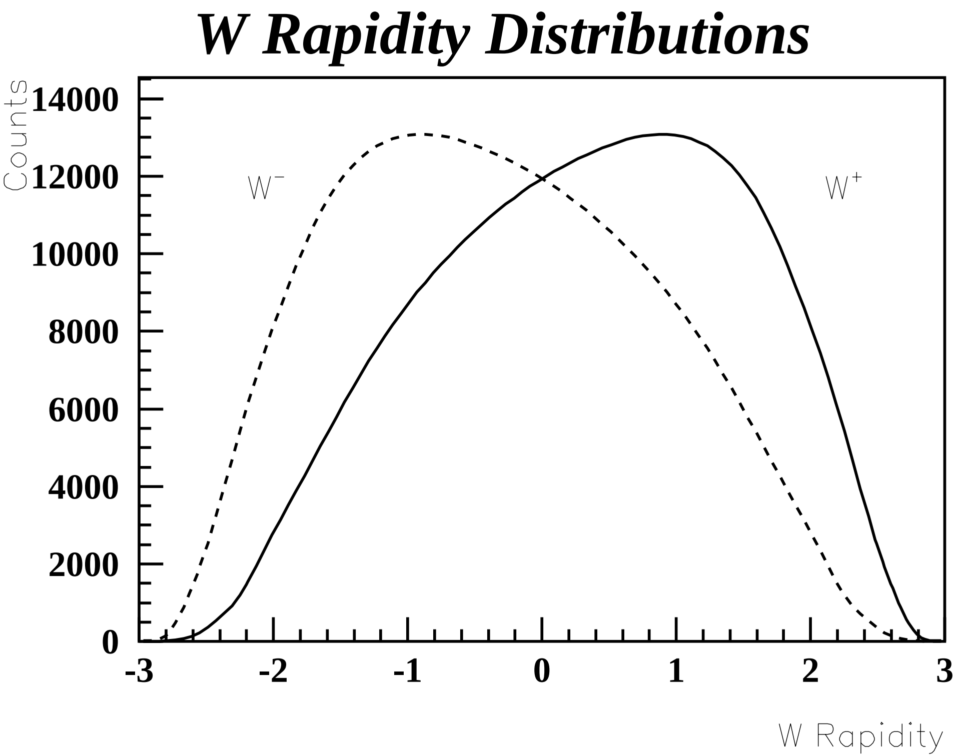

Figure 1.2: The $W$ rapidity distributions in $p\overline{p}$ collisions at $\sqrt{s} = 1.8$ TeV as simulated by ResBos Monte Carlo. The $W$ production charge asymmetry exists because $u$ quarks carry on average more momentum than $d$ quarks.

the lepton asymmetry which is a convolution of the $W$ production charge asymmetry and the well known asymmetry from the $V-A$ $W$ decay. The two asymmetries are in opposite directions and tend to cancel, especially in the forward direction. However, since the $V-A$ asymmetry is well understood, the lepton asymmetry is equally sensitive to the parton distributions. The lepton charge asymmetry is defined as:

$$A(y_l) = \frac{d\sigma^+/dy_l - d\sigma^-/dy_l}{d\sigma^+/dy_l + d\sigma^-/dy_l}, \tag{1.1}$$

where $d\sigma^+$ ($d\sigma^-$) is the cross section for $W^+$ ($W^-$) decay leptons as a function of lepton rapidity, with positive rapidity being defined in the proton beam direction.

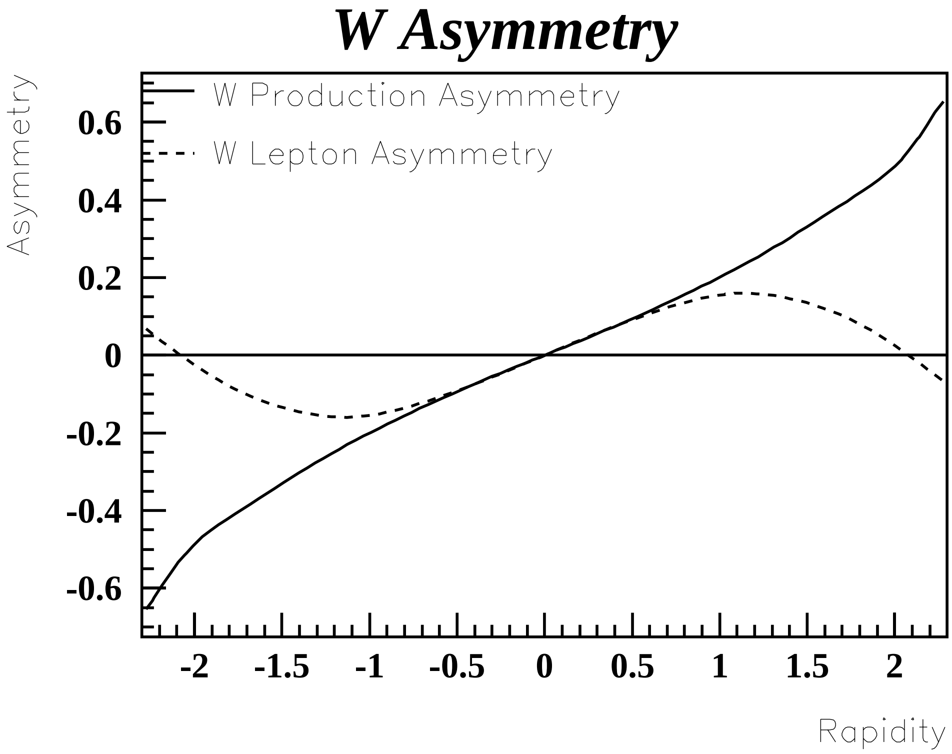

Figure 1.3: The *W* production charge asymmetry as a function of *W* rapidity compared with *W*-decay lepton charge asymmetry which is a convolution of the *W* production charge asymmetry and the effect of the *W* V-A decay.

Figure 1.2 compares the difference between the *W* production charge asymmetry and the *W* lepton charge asymmetry. Note that in the Monte Carlo, we have applied the lepton kinematic cuts as we do in the analysis of *W* data. While the *W* production charge asymmetry is not a function of lepton kinematic cuts, the lepton charge asymmetry does depend on the cuts. This effect is fully estimated from the Monte Carlo. This is discussed in Chapter 5 of this thesis.

## 1.3 Parton Distribution Function (PDF) Constraint

Information on the $d/u$ ratio in the nucleon mainly comes from measurements done in deep inelastic scattering experiments (DIS). In these experiments, the cross section ratio of lepton scattering off Hydrogen and Deuterium targets is measured. In particular, both the NMC [7] and the recent E665 [8] experiments perform measurements of $F_2^{\mu n}/F_2^{\mu p} = 2F_2^{\mu d}/F_2^{\mu p} - 1 \approx \frac{u+4d}{4u+d}$, which is correlated to the magnitude of $d/u$ ratio in the proton. This measurement, however, is subjected to theoretical uncertainties from unknown higher twist and nonperturbative effects at low values of $Q^2$ [9] and from uncertainties in the corrections for deuteron binding effects [10].

In the early papers [3] [4], the lepton charge asymmetry in the $W$ boson decays produced in $p\overline{p}$ collisions at $\sqrt{s} = 1.8$ TeV was shown to be sensitive to the slope of the ratio of $d$ and $u$ quark distributions in the nucleon versus $x$, the fraction of momentum carried by $d$ or $u$ quarks. The $W$ asymmetry data at the Tevatron $(Q^2 \approx M_W^2)$ are free from the theoretical uncertainties that affect the DIS data.

Figure 1.3 shows that various PDFs predict different $d/u$ slopes in the $x$ region of CDF $W$ production. This is compared with predictions of $W$ lepton charge asymmetry calculated using the DYRAD Monte Carlo [6] with various PDFs as input. There is strong correlation between the slope of the $d/u$ quark distributions in the proton and the $W$ lepton charge asymmetry.

The CDF 1992-1993 $W$ charge asymmetry data [1] demonstrated for the first time the sensitivity of $W$ charge asymmetry to the slope of $d/u$ ratio. The use of these previous data resulted in a reduction in the uncertainty from PDFs in the $W$ mass measurement [11] from 75 to 50 $MeV/c^2$.

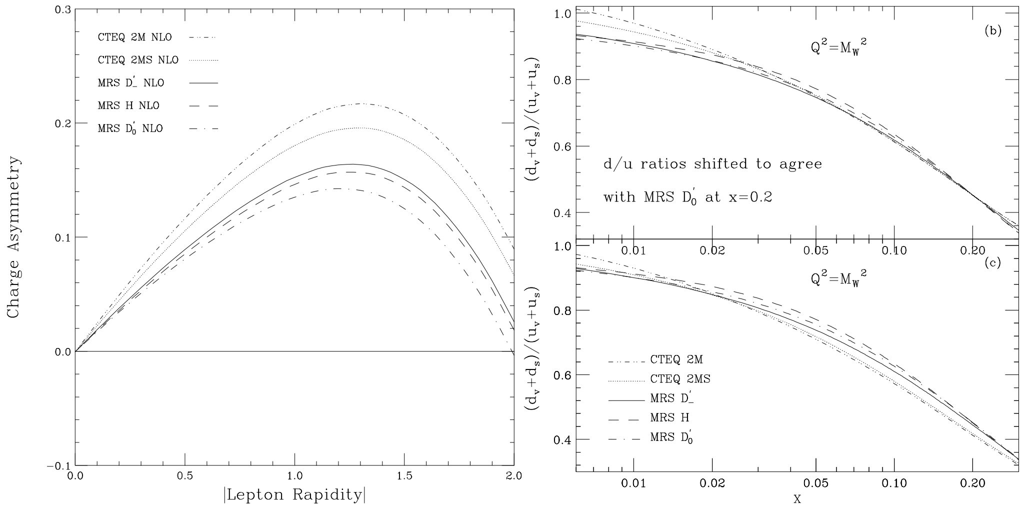

Figure 1.4: In the left plot, the $W$ lepton charge asymmetry as a function of $W$ rapidity calculated using the DYRAD Monte Carlo for various PDFs. In the right plot, the $d/u$ ratio of various PDFs. These calculations indicate that PDFs with higher slope of $d/u$ predict bigger $W$ lepton charge asymmetry.

## 1.4 The Analysis Overview

In chapter 2, we briefly discuss the the experimental setup and data collection. The data analysis using central e, central $\mu$ and plug e data samples are discussed in Chapter 3 and 4. A brief summary is presented for the forward muon analysis in Chapter 5. Chapter 6 discusses the $W$ lepton charge asymmetry measurements and the comparison between CDF data and predictions from various PDFs.

# Chapter 2

# Experimental Apparatus

The data used in this analysis were recorded by the CDF (Collider Detector at Fermilab) detector during the 1992-1995 Tevatron runs. We describe the experimental apparatus in the following sections.

## 2.1 The Accelerator

The Fermilab Tevatron is currently the world's highest energy accelerator. It is a synchrotron employing a ring of superconducting magnets two kilometers in diameter. When it works in collider mode (as it was during 1992-1995 collider runs), the Tevatron provides proton-antiproton collisions at center of mass energy $\sqrt{s} = 1.8$ TeV ($10^{12}$ eV).

The protons and antiprotons undergo a staged acceleration in energy leading to a final beam energy of 900 GeV. Figure 2.1 shows a schematic view of the facilities. The whole process starts with a bottle of hydrogen gas. Inside a Cockroft-Walton apparatus at the base of the Linear Accelerator (Linac), hydrogen atoms are ionized with one extra electron and accelerated to an energy of 750 keV. These charged

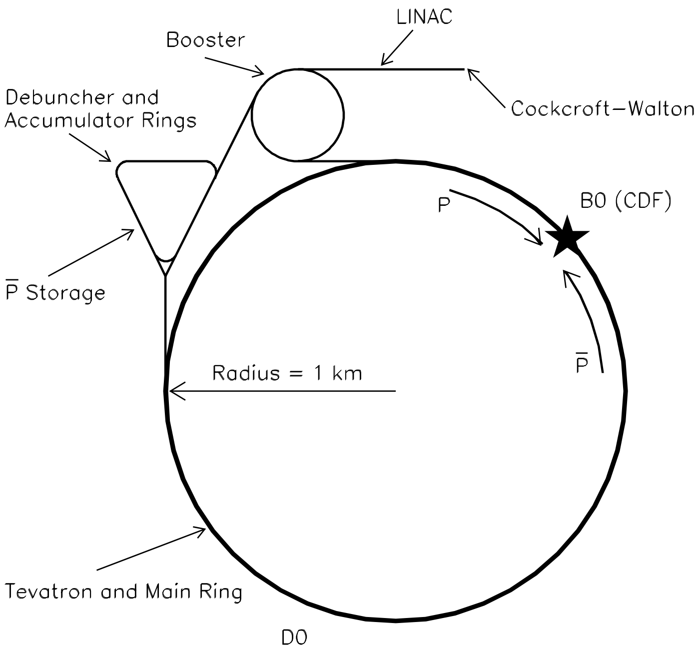

Figure 2.1: A schematic view of the layout of the facilities used to provide $p\overline{p}$ collisions at a center of mass energy of 1.8 TeV.

hydrogen atoms are accelerated to an energy of 400 MeV by a 150 meter long linear accelerator (Linac). At the exit of Linac, the ions are stripped of their electrons by passing through a carbon foil and become protons. The resulting proton beam is passed to the Booster Synchrotron Ring where the energy of protons is boosted to 8 GeV. Inside the Booster, the protons are also coalesced into discrete bunches for injection into the Main Ring.

The Main Ring and Tevatron are both located inside the same tunnel. The Main Ring synchrotron accelerates proton bunches to 150 GeV in energy. In the next stage, protons are directed either to the Tevatron or to a tungsten target to produce secondary particles. In the latter case, protons accelerated in the Main Ring to 120 GeV and are extracted, transported to the target area, and focused on the target. The collisions in the target produce a wide range of secondary particles including antiprotons. Antiprotons are collected and transported to the Debuncher Ring where they are reduced in momentum spread by a process called stochastic cooling. Antiprotons are then transferred to the Accumulator Ring for storage. Once a sufficient number of antiprotons is reached, they are reinjected to the Main Ring to be accelerated to an energy of 150 GeV and are passed into the Tevatron in the opposite direction of the proton beam. Both beams are finally accelerated to 900 GeV inside the Tevatron. They circulate inside the same magnetic and RF fields of Tevatron but in different trajectories.

The two trajectories intersect at four points along the circumference of the ring. The places where the beams intersect are called collision points. At two collision points (B0 and D0) where the two major colliding-beam experiments are located, four special quadrupole magnets are placed several meters on both sides of the collision points. They focus the beams to a transverse size of $\approx 40\ \mu m$ transversely in size thus boosting the luminosity of collisions. At two other points where no experiments exist, electrostatic separators are used to prevent the collisions from happening in order to extend the beams' lifetime. During 1992-1995 collider runs, there were six bunches in each beam. As a result, proton and antiproton beams collide at the CDF detector at a rate of once every 3.5 $\mu s$. Typically there are a few $10^{12}$ protons and a few $10^{11}$ antiprotons inside a bunch. The average instantaneous luminosity was $\approx 9 \times 10^{30} cm^{-2} s^{-1}$ during 1994-1995 Runs and $\approx 3 \times 10^{30} cm^{-2} s^{-1}$ during 1992-1993 Runs.

## 2.2 The CDF Detector

The CDF detector is a general purpose detector built to exploit the Fermilab Tevatron collider machine. The CDF detector has been described extensively in

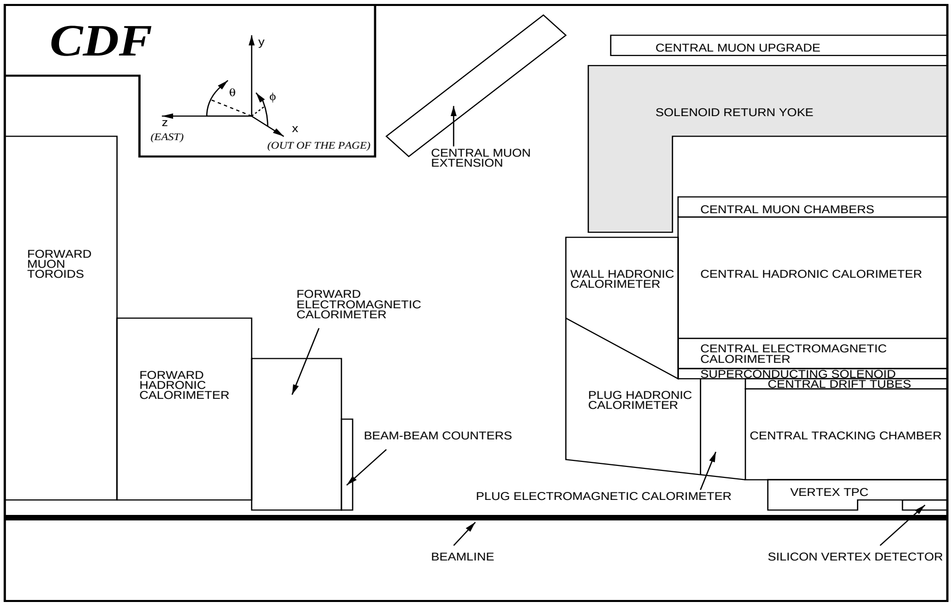

Figure 2.2: A cut-away diagram of the various components of the CDF detector (the interaction point is in the lower right corner). The coordinate system is defined by the proton beam being in the $+z$ direction.

many publications and is summarized in reference [12]. Here we concentrate on describing the relevant parts of the detector for the detection of high transverse momentum $P_T$ leptons (the electrons, muons, and neutrinoes in this case) at CDF. This is important for the $W$ charge asymmetry analysis as described in the later parts of this thesis. We start with a general overview of the detector followed by more detailed descriptions of detector systems such as tracking, muon detection, calorimetry, trigger, and data streaming.

### 2.2.1 Overview of the Detector

Figure 2.2 shows a cutaway view of a quarter of the CDF detector. Here only the upper east quadrant of the detector is shown. The $(x, y, z)$ axes and the $(\theta, \phi)$

angles of the global coordinate system are also shown in the figure. The origin of the coordinates is defined to be the center of the detector which is close to the center of the $p\overline{p}$ interaction region. The right-handed co-ordinate system has its positive $z$ direction (east) defined along the proton beam direction and its positive $x$ axis points outwards (north) of the Tevatron ring. As a result, positive $y$ axis points upwards. We define the azimuthal angle ($\phi$) as the angle around the beam line and the polar angle ($\theta$) is defined as the angle relative to the proton direction. Because the "natural" phase space for energetic hadronic collisions is described in rapidity, transverse momentum and azimuthal angle, the detector components are chosen to be an approximately uniform segmentation in the $(\eta, \phi)$ space, where $\eta$ is called pseudorapidity and is defined as:

$$\eta = -ln(tan\tfrac{\theta}{2}).$$

The CDF detector is essentially symmetric in $\phi$ and is also forward-backward symmetric. It is divided into a central detector ($10^o < \theta < 170^o$) including the end-plugs, and the forward/backward regions ($\theta < 10^o$). The CDF detector is particularly suited for the study of leptons with high transverse momentum. The detector subsystems that are important for this analysis are described below.

### 2.2.2 Tracking

There are three separate tracking systems in the CDF detector in its 1992-1995 configuration. Beginning at the collision point, particles traverse the Silicon Vertex Detector (SVX), the Vertex Time Projection Chambers (VTX) and the Central Tracking Chamber (CTC).

### The Silicon Vertex Detector (SVX)

The Silicon Vertex Detector (SVX) is located immediately outside the beam pipe. The SVX is designed to track particles near the interaction point and has the capability to distinguish sequential decay vertices at the tens of microns level in the $x-y$ plane. As is discussed later, it is an essential device for electron tracking and charge determination at high pseudorapidity.

After the Tevatron 1992-1993 collider run (Run 1A) and prior to the 1994-1995 collider run (Run 1B), the SVX was replaced by the SVX' (SVX prime) because of the radiation doses that the SVX accumulated during the Run 1A. The radiation damage resulted in increased leakage currents and the hit efficiency was significantly degraded near the end of Run 1A. The SVX' and SVX are very similar. The upgrade from the SVX to the SVX' involves the following changes: (1) DC-coupled devices have been changed into AC coupled to reduce leakage current and coherent noise; (2) the readout chips have been upgraded to be more radiation hard for the increased luminosity of Run 1B; (3) the radius of the inner most layer has been reduced from 3.00 cm to 2.86 cm to eliminate some geometrical cracks in the inner most layer.

The SVX consists of two identical barrels placed at both sides of $z = 0$. Figure 2.3 shows an overall lay-out of one of its barrels. Each barrel is constructed with four concentric radial layers of silicon strip detectors. These detectors are arranged as a twelve sided barrel at each radial position. The inner layer starts at $r = 2.86$ cm from the beamline, and the outer layer at a radius of $r = 7.87$ cm. The detectors are electrically bonded to each other along beam direction in groups of three. A group of three connected detectors is called a "*ladder*". As shown in Figure 2.4, it is the basic subdivision of the device. These bonds are made with 25 $\mu m$ Aluminum wire which is ultrasonically fused to pads on the detector

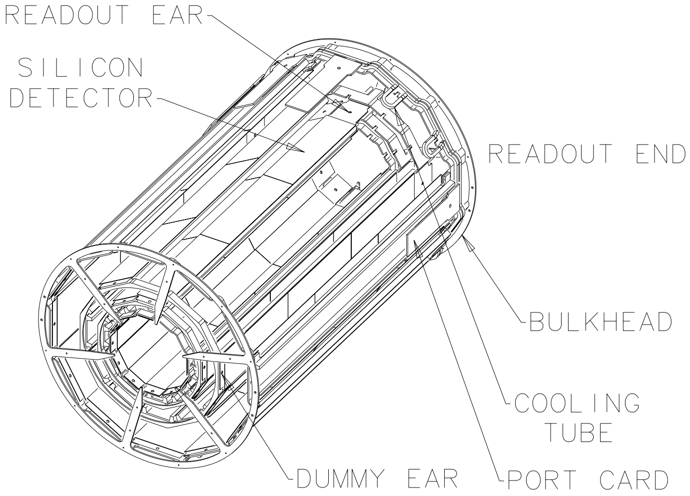

Figure 2.3: An overall lay-out of one of the two barrels of the SVX detector.

surface. Each detector is 8.5 cm long so that an individual readout channel sees 25.5 cm long strip. A 30° wedge consists of four such ladders with increasing width from the inner layer to outer layer. The axial readout strips of each detector is 60 $\mu m$ in width except the outer layer which has 55 $\mu m$ strips. There are a total of 46080 channels for the whole SVX detector. A typical SVX hit is a cluster of several neighboring strips (usually two or three) and the charge weighted position of the cluster has a position resolution $\sigma \approx 10$ $\mu m$. Because $p\overline{p}$ interactions are spread along the beamline with standard deviation $\sigma \approx 30$ cm, the geometrical acceptance of the SVX includes about 60% of $p\overline{p}$ interactions. The SVX covers the pseudorapidity region $|\eta| < 1.9$ if four hits are required in a SVX track. The coverage extends to $|\eta| < 2.3$ when three hit SVX tracks are included.

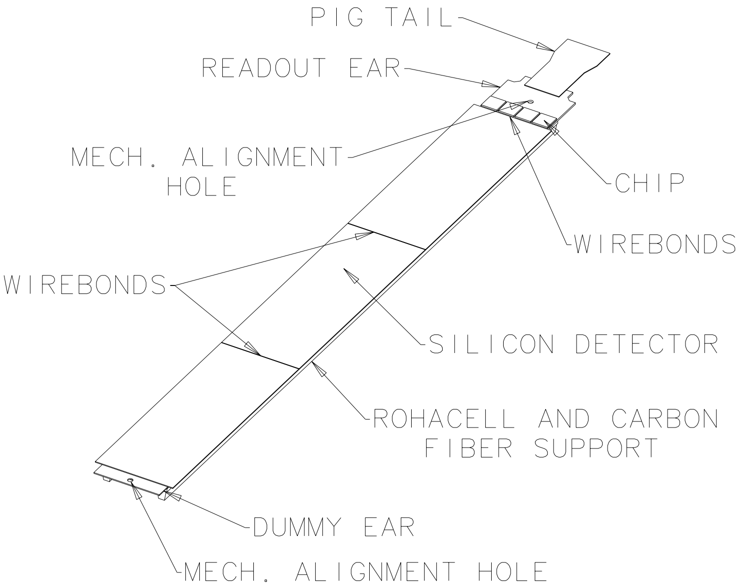

Figure 2.4: Schematic view of a ladder.

### The Vertex Time Projection Chambers (VTX)

The SVX is mounted inside the Vertex Time Projection Chambers (VTX). It provides tracking information up to a radius of 22 cm and $|\eta| < 3.25$. The VTX consists of a set of drift chambers organized into eight modules mounted end-to-end along $z$ axis and each module is segmented azimuthally into 8 wedges. The primary goal of the VTX is to measure the location of $p\overline{p}$ interaction vertex along the $z$ axis. The wires are perpendicular to the beam line and the radial centerline of the wedges. The radial and $z$ position of sense wires combined with measured drift distance along $z$ axis provide track information in $r - z$ view. A resolution of 1 mm along the $z$ axis for $p\overline{p}$ interaction vertices is achieved.

### The Central Tracking Chamber (CTC)

The Central Tracking Chamber (CTC) is the main tracking device at CDF. Completely immersed in a 1.4116 Tesla superconducting solenoidal magnetic field, it provides excellent momentum measurement of charged particles. The CTC is a 1.3 m radius and 3.2 m long cylindrical drift chamber which contains 84 layers of sense wires grouped into nine "super layers". Five of the super layers consists of

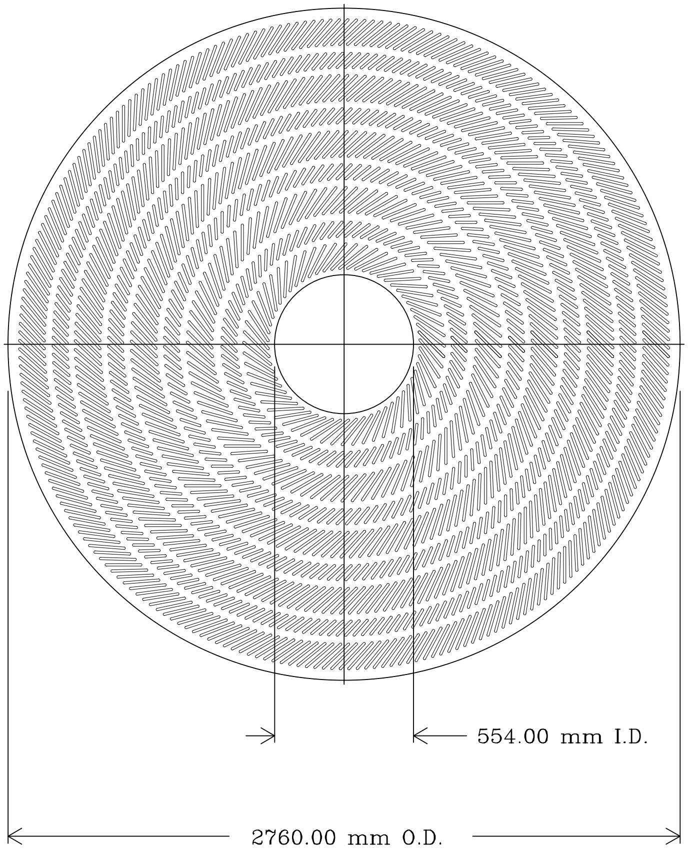

Figure 2.5: The end view of the Central Tracking Chamber showing the grouping of stereo and axial cells into nine superlayers.

12 axial sense wires each; four stereo superlayers consist of six sense wires each tilted by $\pm 3^o$ relative to the beam direction. Figure 2.5 shows the endplate of the chamber displaying $45^o$ tilt of the superlayers to the radial direction to correct for the Lorentz angle of the electron drift in the magnetic field. The drift trajectories are approximately azimuthal inside the magnetic field. The resulting transverse momentum resolution for CTC track alone is $\frac{\delta P_T}{{P_T}^2} \approx 0.002 GeV^{-1}c$. It is improved to $\frac{\delta P_T}{{P_T}^2} \approx 0.001 GeV^{-1}c$ when the beam position information is additionally used in the track fit.

### 2.2.3 Muon Detection

At CDF, muons are identified by a track in the CTC which is matched to a good-quality track stub in one of the CDF muon detectors. These muon detectors are divided according to their pseudorapidity coverage and are named accordingly the central muon drift chambers (CMU), the central muon upgrade (CMP), the central muon extension chambers (CMX) and the forward muon system (FMU) as shown in Figure 2.2.

#### Central Muon Chambers (CMU & CMP)

The CMU and CMP muon detectors cover the pseudo-rapidity region ($|\eta| < 0.6$). Both detectors consist of four layers of single wire drift chambers which measure muon position in $r - \phi$ plane from drift time information. Figure 2.6 shows a sectional view of the CMU chambers. The actual wire measures 2.3 meters long. The position resolution in $r - \phi$ view is $\approx 250\ \mu m$. The CMU additionally determines track $z$ position by charge division. The CMU is placed between the central hadronic calorimeter and the magnet return yoke, and the CMP is placed outside the magnet return yoke. The amount of material before the CMU and CMP is 5

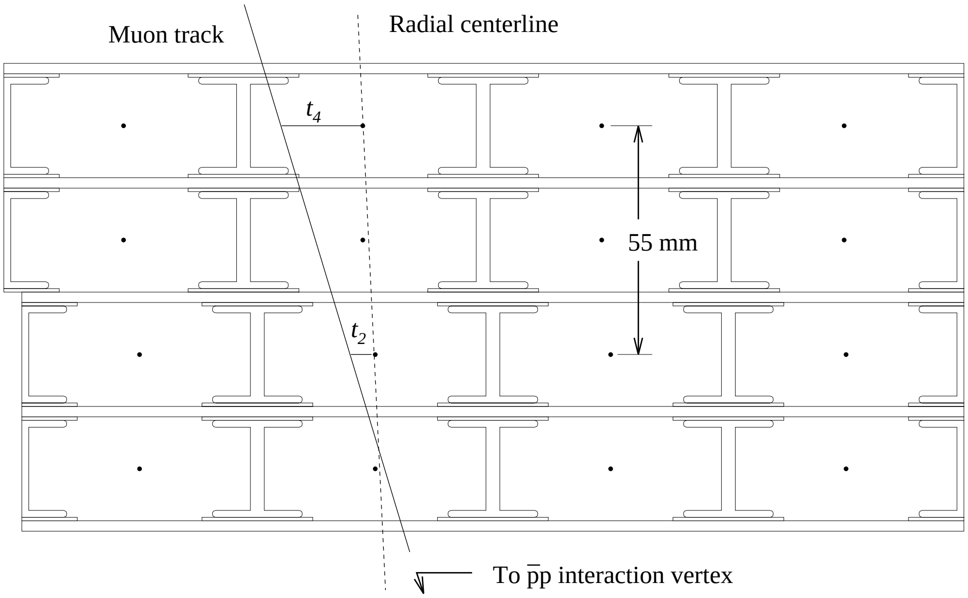

Figure 2.6: The sectional view of the Central Muon Chambers. A muon track stub traverses four layers of muon chambers.

and 8 interaction length, respectively.

### Central Muon Extension (CMX)

The muon coverage is extended by additional muon chambers in the pseudorapidity range $0.6 < |\eta| < 1.0$. These are again constructed from single wire drift chambers. There are scintillators on both sides of the CMX which are used for the CMX muon trigger.

### Forward Muon Detector (FMU)

The forward muon detector (FMU) consists of three sets of drift chambers sandwiched with two steel magnets (toroids) on each side of the detector. The analysis of the FMU data are described is a separate paper [13]. The FMU covers the pseudorapidity region of $1.9 < |\eta| < 3.6$. Because of large backgrounds at $2.5 < |\eta| < 3.6$, only data from $1.9 < |\eta| < 2.5$ regions of the FMU are used in the $W$ asymmetry analysis.

### 2.2.4 Calorimetry

The CDF detector is equipped with both electromagnetic and hadronic calorimeters which together provide a $2\pi$ azimuthal coverage and a pseudorapidity coverage of $|\eta| < 4.2$. The calorimeters have a projective tower geometry with a fine granularity. They are separated into three regions: central, plug and forward. The pseudorapidity coverage for each of these regions is $|\eta| < 1.1$, $1.1 < |\eta| < 2.4$ and $2.4 < |\eta| < 4.2$ separately. In all, seven calorimeter systems are involved, Central Electromagnetic Calorimeter (CEM), Central Hadron Calorimeter (CHA), Endplug Electromagnetic Calorimeter (PEM), Endplug Hadron Calorimeter (PHA), Wall Hadron Calorimeter (WHA), Forward Electromagnetic Calorimeter (FEM) and Forward Hadron Calorimeter (FHA). The Wall Hadron Calorimeter (WHA) fills the rapidity gap between Endplug Hadron Calorimeter (PHA) and Central Hadron Calorimeter (CHA). An overview of the different calorimeter components is given in Table 2.1

#### Central Calorimeters

The central calorimeters cover a polar angle region of $39^o < \theta > 141^o$ ($|\eta| < 1.1$). They are azimuthally segmented into $15^o$ wedges. There are 48 wedges in all, with 24 wedges on each side of $z = 0$ plane. Each wedge consists of an electromagnetic part and a hadronic part and is divided into 10 towers with $\Delta\eta = 0.11$. For the electromagnetic part, lead sheets are interspersed with scintillator as the active detector medium, and the hadronic calorimeter part consists of steel

| Calorimeter Component | Geometric Coverage $\eta$ Range | Energy Resolution | Depth |
|---|---|---|---|
| CEM | $0.0 < \|\eta\| < 1.1$ | $13.5\%\sqrt{E_T} \oplus 2\%$ | $18X_o$ |
| PEM | $1.1 < \|\eta\| < 2.4$ | $22\%\sqrt{E} \oplus 2\%$ | $18-21X_o$ |
| FEM | $2.4 < \|\eta\| < 4.2$ | $26\%\sqrt{E} \oplus 2\%$ | $18X_o$ |
| CHA | $0.0 < \|\eta\| < 0.8$ | $50\%\sqrt{E_T} \oplus 3\%$ | $4.7\lambda_{abs}$ |
| WHA | $0.8 < \|\eta\| < 1.3$ | $75\%\sqrt{E} \oplus 4\%$ | $4.5\lambda_{abs}$ |
| PHA | $1.3 < \|\eta\| < 2.4$ | $106\%\sqrt{E} \oplus 6\%$ | $5.7\lambda_{abs}$ |
| FHA | $2.4 < \|\eta\| < 4.2$ | $137\%\sqrt{E} \oplus 3\%$ | $7.7\lambda_{abs}$ |

Table 2.1: The coverage and resolution of the CDF calorimeters.

plates interspersed with scintillator layers. Figure 2.7 shows a CEM wedge with its light collection system. Placed near the shower maximum position of the CEM, the central strip chambers (CES) determine the shower position and transverse shower profile at shower maximum. The position resolution for 50 GeV electrons is ≈ 2 mm in both $r-\phi$ and $z$ directions. The information from the CES is used for electron identification in the central region.

### Plug and Forward Calorimeters (PEM,FEM)

The plug and forward calorimeters cover the polar angle region of $1.7^o < \theta < 36^o$ and $144^o < \theta < 178.3^o$. The segmentation is roughly 0.1 in pseudorapidity unit and $5^o$ in $\phi$. These calorimeters are all based on gas proportional chambers with cathode readout. The cathodes are constructed with pads and strips etched on printed circuit board in the chambers. For this analysis, only the central and plug electron data are utilized. There was no trigger for FEM electrons because of the high trigger rate. In addition, electrons in the FEM region are not covered by tracking chambers.

The PEM consists of two 50 cm thick disc-shaped modules, covering both ends

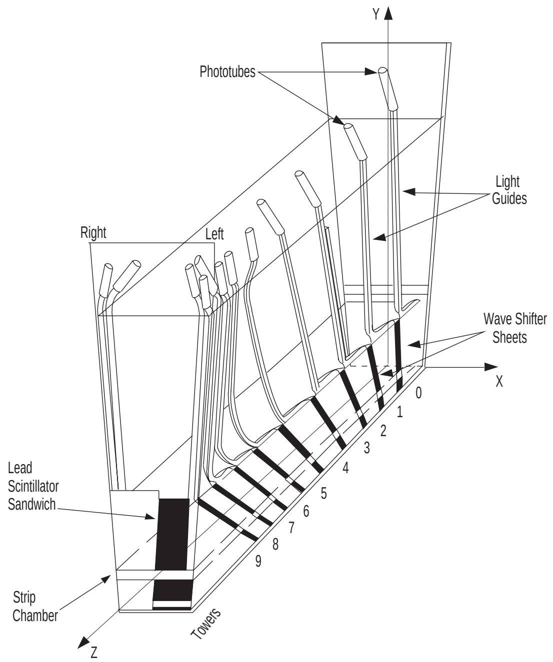

Figure 2.7: A wedge of CEM and its light collection system.

of the 3 m long solenoid in the CDF central detector (see Figure 2.2). Each of the two PEM modules is formed by four quadrants of $\Delta\phi = 90^o$ and each quadrant consists of 34 layers of proportional tube arrays sandwiched between lead panels. Figure 2.8 illustrates the construction of the proportional tubes. These tubes were made of conductive plastic tubes of a square inner cross section of 7 $mm \times 7$ $mm$. Figure 2.9 shows the construction of one quadrant of the PEM. The pads are etched out of the copper plating clad on G-10 panels on one side of every proportional tube panel. They are segmented with boundaries defined by the polar coordinates $\eta$,$\phi$, and $z$ as shown in the top sketch in Figure 2.9. The segmentation in $\eta$ is roughly 0.1 unit of pseudorapidity and $5^o$ in $\phi$. Longitudinally these pads are ganged together at each of the polar coordinates ($\eta$,$\phi$) into three projective towers. Besides the pads, the first ten layers of the second longitudinal segment have strips

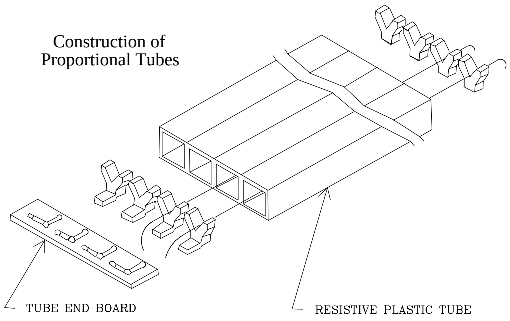

Figure 2.8: The PEM's sensitive layer is made of conductive plastic proportional tubes sandwiched between lead absorber panels. The anodes of each layer are ganged together in unit of a quadrant.

of in both $\eta$ and $\phi$ directions on the other G-10 panel of proportional tubes. These strips cover between $1.2 < |\eta| < 1.8$ and are segmented in $\Delta\eta \times \Delta\phi = 0.02 \times 1^o$. The pads and strips on printed circuit board are positioned to 0.1 mm. This is important for precision position measurement of plug electrons. The energy in each of the 34 layers of a quadrant is read out and provides measurement of the plug electron's longitudinal shower profile. This information is used in the plug electron trigger to suppress high rate due to neutron-induced large energy deposits in a single PEM layer. All gas calorimeters employ a "gas gain control" system to stabilize the gain variation from pressure and temperature changes.

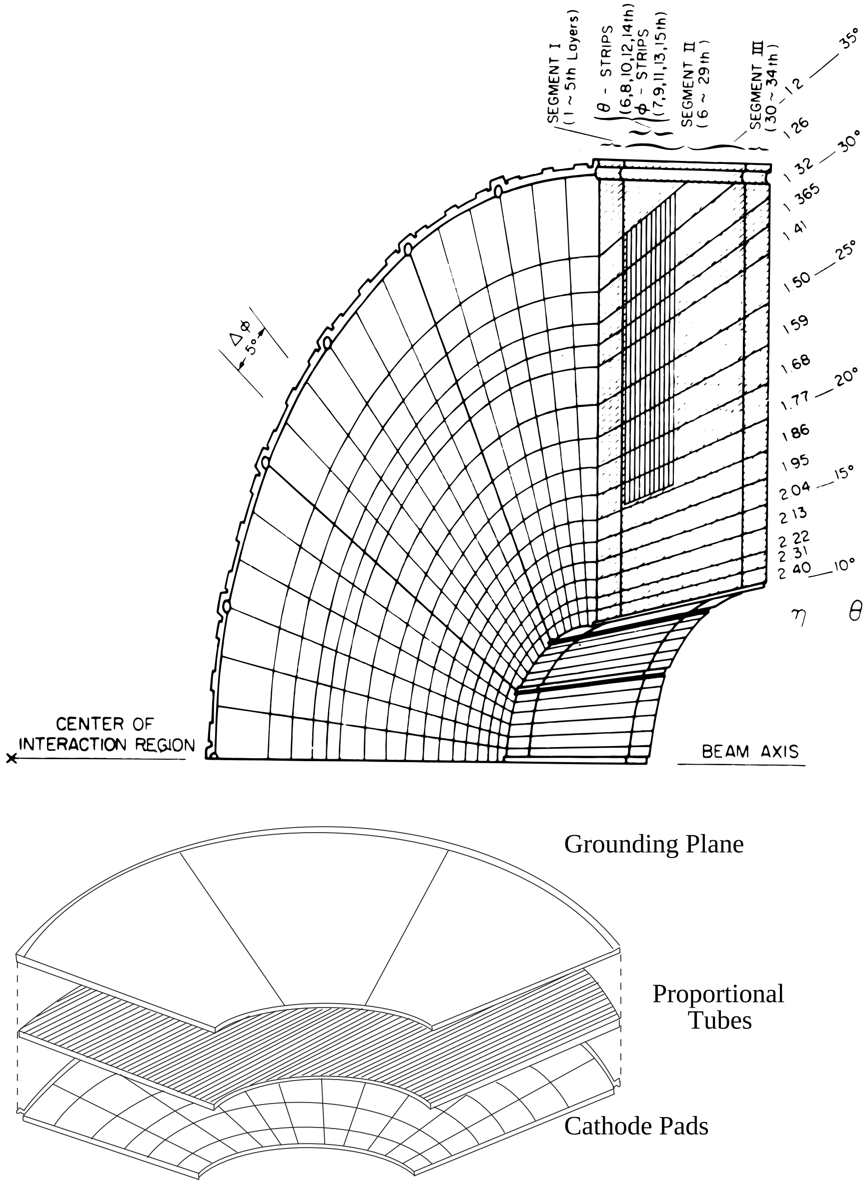

Figure 2.9: View of a PEM quadrant. Pads are segmented in 5 degree unit in $\phi$ and strips in 1 degree unit covering $1.2 < |\eta| < 1.8$.

### 2.2.5 Trigger and Data Streaming

At the Tevatron, bunch crossings at CDF happen at a rate of roughly once every 3.5 $\mu s$. With a $p\overline{p}$ total inelastic cross-section of 60 mb [14] at $\sqrt{s} = 1800$ GeV and a typical luminosity of $1.0 \times 10^{31} cm^{-2} s^{-1}$, the total inelastic interaction rate is $\approx 0.6 MHz$. This is almost two interactions per bunch crossing. In contrast, the CDF detector is only capable of writing to tape up to 10 events per second. Note the events from physics processes of interest occur at a much lower rate (less than a few events per second). Both factors dictate the use of an online trigger in the data taking. At CDF, a three level trigger is employed. Each level of trigger consists of a set of logically OR'ed triggers. The levels of sophistication and the decision time increase with the trigger level. The triggers are designed to select interesting events while minimizing the dead time incurred during the decision process.

At level 1, the decision is made within the 3.5 $\mu s$ time and therefore incurs no dead time. The level 1 decision is based on the presence of energy cluster above some energy thresholds in the $\Delta\eta \times \Delta\phi = 0.2 \times 15^o$ trigger towers of calorimeters, and on the presence of muon track segments in the muon chambers. This reduces the event rate down to about a few $kHz$. The events that pass Level 1 trigger are turned to the level 2 trigger processor.

At level 2, the decision time per event is about 20 $\mu s$ and this incurs $\approx 5\%$ dead time as events that come through level 1 triggers during the level 2 decision time are ignored. Level 2 decisions are based on the presence of calorimeter energy clusters, missing transverse energy in the calorimeters, stiff central tracks inside CTC, and matching of CTC and level 1 muon chamber track stubs. The decision is made by an Alpha processor which is fed with the above information. The energy cluster information is gathered by a hardware cluster finder, which searches in the calorimeters for a seed tower with energy over a threshold and adds in neighboring tower energies above a lower threshold. The $E_T$ and mean $\eta$ and $\phi$ are calculated for each cluster found. A rough missing transverse energy is calculated by the vector sum of $E_T$ of all energy clusters in the calorimeter. The Central Fast Tracker (CFT) finds a list of stiff tracks with momentum resolution of $\delta P_T / {P_T}^2 = 3.5\%$. Furthermore, level 1 muon stub information is matched to CFT tracks to identify muons. The event rate out of level 2 is typically $20 - 25Hz$ depending on the instantaneous luminosity. A level 2 trigger pass initiates a full detector readout which takes of the order a few ms per event. This results in a data acquisition (DAQ) deadtime of about 5%.

Once a full event is read out and assembled in the event builder, it is passed to one of a farm of Silicon Graphics processors for level 3 processing. The level 3 trigger is a software trigger, written in FORTRAN and running a scaled down version of the CDF offline reconstruction code. Details of the event are calculated and more complex triggers of a variety of physics interests can be constructed from the calculated event characteristics. Level 3 rejects $60-80\%$ of events passing Level 2 triggers. The event rate written to tape is of the order of a few $Hz$.

Events that pass Level 3 triggers are recorded separately into different streams depending on which sets of Level 3 triggers they pass. The data from different streams are processed separately offline. For Run 1B, there are two main streams, the Stream A and Stream B. The Stream A, also called the EXPRESS stream, usually contains events that pass the essential triggers. The event record for these events is small enough that they can be processed offline a couple of days after data-taking. The timely processing of the data allows for a quick identification of problems, as well as a prompt data analysis. The Stream B contains triggers with much looser requirements and as a result, the event record is much bigger in size. More detailed studies usually have to be done with the Stream B data.

# Chapter 3

# Central $W \rightarrow l + \nu$ Analysis

When either the $e$ or $\mu$ are detected by the central electromagnetic calorimeter (CEM) or central muon detectors (one or more of CMU, CMP and CMX), the $W \rightarrow l + \nu$ ( $l = e$ or $\mu$) event is called a central $W$. In this chapter, the central $W$ data sample and event selection are discussed. Backgrounds in the central $W$ data samples are listed and their magnitude is estimated separately. The uncertainty in the momentum scale of the CTC, the energy scale of the CEM, and the rate of charge mis-identification in the CTC for central tracks are discussed. The offline reconstruction does not correct for CTC wire misalignment, which if left uncorrected may potentially cause a charge-dependent momentum mis-measurement. A correction is derived from the central $W$ electron data and is applied to the data. Finally the CTC tracking, central $e/\mu$ triggers, and the lepton identification requirements are verified to be charge independent, and therefore not bias the charge asymmetry measurement.

## 3.1 Data Sample

The $W \rightarrow l + \nu$ events are signaled by the presence of a high $E_T$ lepton and large missing transverse energy. We identify the central $W \rightarrow e + \nu$ events by requiring the presence of a large electromagnetic energy cluster in the central electromagnetic calorimeter (CEM) associated with a high $P_T$ CTC track, and presence of large missing transverse energy in the event. The Run 1A and 1B central electron triggers are similar. The central $W$ electron analysis is based on the central $W$ electron dataset. For Run 1B, this dataset contains events in the express data stream passing Level 3 triggers "CEM_22_W" and "CEM_25GeV_W_Notrk". The "CEM_22_W" trigger requires $E_T > 22$ GeV, $\not{E}_T > 22$ GeV and CTC track $P_T > 13$ GeV. The "CEM_25GEV_W_Notrk" requires $E_T > 25$ GeV and $\not{E}_T > 25$ GeV but no CTC track requirement. The two triggers form two highly overlapping data samples. The second trigger does not have CTC track requirement and this provides an independent high $E_T$ electron sample for CTC tracking studies. The $W$ events mostly come in through Level 2 trigger "MET_20_CEM_16_XCES" which requires $\not{E}_T > 20$ GeV and $E_T > 16$ GeV. The $88 pb^{-1}$ of Run 1B data contain about 223 $k$ Level 3 electron triggers. In the offline analysis, these events are pre-selected by the following requirements:

$E_t(uncorrected) > 22$ GeV
$E_{Had}/E_{EM} < 0.125$
$P_T$(not beam constrained) $> 13$ GeV
$\not{E}_T > 20$ GeV

where the above cuts are made on variables calculated in the offline data reconstruction. About 87 $k$ $W$ electron candidate events remain in the electron data sample.

The central $W \rightarrow \mu + \nu$ events are flagged by a muon track stub in one of the CDF muon detectors, a high $P_T$ CTC track which matches the muon stub, and large missing transverse energy. In addition, the energy deposits in both EM and hadron calorimeter towers should be consistent with that of a single minimum ionizing particle. The analysis is based on the inclusive high $P_T$ central $\mu$ dataset. The dataset is made from the express stream with events passing Level 3 triggers and requiring $\mu$ candidate events with $P_T > 18$ GeV. There are a total of 628 $k$ events in the muon dataset. In the offline analysis, the events are pre-selected by requiring:

$P_t(corrected) > 20$ GeV
$E_{Had} < 6$ GeV
$E_{EM} < 2$ GeV
$E_{Had} + E_{EM} > 0.5$ GeV
$\not{E}_T > 20$ GeV $|\delta X| < 2$ or 5 or 4 cm if CMU or CMP or CMX.

A total of 124 $k$ $W$ muon candidate events remain in the sample.

## 3.2 Event Selection

### Central $W \rightarrow e\nu$ Event Selection

The following selection cuts are made to form the final central $W$ electron sample:

**$E_T > 25$ GeV:** $E_T$ is the electron cluster energy transverse to the beam direction,

$$E_T = Esin(\theta), \tag{3.1}$$

where $\theta$ is the polar angle of the associated CTC track and E is the cluster energy.

**$\not{E}_T > 25$ GeV:** $\not{E}_T$ is the missing transverse energy $E_T$ in the event defined by,

$$\vec{\not{E}}_T = -\sum_i E_T^i \hat{\mathbf{n}}_\mathbf{i}, \tag{3.2}$$

where $\hat{\mathbf{n}}_\mathbf{i}$ is a unit vector perpendicular to the beam axis and pointing at the center of the i$^{th}$ calorimeter tower. The sum is over all calorimeter towers with $|\eta| < 3.6$.

**$E_T^{jet} < 20$ GeV:** The $E_T$ refers to the biggest transverse energy of a jet. The jet is measured in a cone of $R = 0.7$ (where $R = \sqrt{(\Delta\eta)^2 + (\Delta\phi)^2}$). This reduces the di-jet background in the $W$ sample.

**$P_T^{high} < 10$ GeV:** The highest $P_T$ track not associated with the electron is required to be less than 10 GeV. This cut removes $Z$ events as well as some QCD background.

**$E_{Had}/E_{EM}$:** The ratio of the energy in the hadronic and electromagnetic sections of the calorimeter associated with the energy cluster is required to satisfy,

$$E_{Had}/E_{EM} < 0.055 + \frac{0.045 * E\ (GeV)}{100\ GeV}, \tag{3.3}$$

where $E$ is the energy of the cluster. The linear term takes into account of the additional leakage associated with high energy electrons.

**$LShr < 0.2$:** This variable measures the energy sharing between the adjacent towers and the CEM tower with the most of the energy in the electron showers. It is defined as

$$LShr = C\frac{\sum_i (E_i - T_i)}{\sigma} \tag{3.4}$$

where $E_i \equiv$ Energy in Adjacent Towers, $T_i \equiv E_i$ is the adjacent tower energy as predicted by the measured lateral shower profile at testbeam and the measured $z$ location from the CES, $\sigma_i$ is the combined characteristic fluctuation of the energy excess ($\equiv E_i - T_i$), $C \equiv Scale\ Factor = 0.14$, and $i$ is over all adjacent towers in the electron shower.

$\boldsymbol{Isolation} < \mathbf{0.1}$**:** The isolation variable is a measure of the energy surrounding the electron. It is defined as,

$$Isolation = \frac{E_T(0.4) - E_T}{E_T} \tag{3.5}$$

where $E_T(0.4)$ is the energy in a cone of $R = 0.4$ in $\eta - \phi$ space, and $E_T$ is the electron's transverse energy.

$\boldsymbol{\chi_s^2} < \mathbf{10}$**:** The $\chi^2$ of the lateral shower shape measured by the strip chambers is required to be consistent with that of electrons measured at the testbeam.

$\mathbf{0.5} < \boldsymbol{E/P} < \mathbf{2.5}$**:** The ratio of the cluster energy and the momentum of the CTC track associated with the energy cluster is required to be consistent with that of a single charged particle. On average this is 1.0 for electrons, but because of the possibility for an electron to radiate photon, there is a long tail in the distribution.

$\mathbf{15\ GeV} < \boldsymbol{P_T} < \mathbf{200\ GeV}$**:** The transverse momentum ($P_T$) is required to be consistent with a $W$ decay electron as well as in a range where the charge can be reliably determined. $P_T$ is measured relative to the beam line and is determined by the track's curvature in the CTC.

**$CurSig > 2.0$:** The curvature significance is defined as,

$$CurSig = Cur/\sigma_{cur} \tag{3.6}$$

where $Cur$ is the curvature of the CTC track and $\sigma_{cur}$ is the error on the curvature measurement. This cut requires that charge is determined with high certainty.

**$|\delta X| < 1.5$ cm:** The difference between the $X$ position measured by the strip chambers and the extrapolation of the CTC track is required to be less than 1.5 cm.

**$|\delta Z| < 3.0$ cm:** The difference between the $Z$ position measured by the strip chambers and the extrapolation of the CTC track is required to be less than 3.0 cm.

**$|D_0| < 0.2$ cm:** The absolute value of the impact parameter $|D_0|$ is the distance of the closest approach of the track to the beam axis. This cut removes events which are not consistent with originating from the interaction region (such events are most likely decays in flight or cosmic rays).

**$|Z_0| < 60$ cm:** The event vertex, as determined by the VTX, is required to be within approximately $2\sigma$ of the center of the detector.

**$|Z_0^{CTC} - Z_0| < 5$ cm:** The difference between the $Z_0^{CTC}$ measured by the CTC track and that measured by the VTX is required to be less than 5 cm. This makes sure that the event vertex is determined correctly in the environment of high instantaneous luminosity.

In addition, the electron candidate is required to be in the fiducial region of the calorimeter wedge. The electron candidate is further required to pass the conversion cuts which reduce the QCD background. Also the runs are checked against a list of known bad runs (i.e. runs where there were detector or DAQ failures). After the above cuts, a total of 44196 events remain in the final electron data sample. Figure 3.1 shows the transverse mass spectrum of the central electron $W$ candidate events ($M_T^2 = 2E_T^e E_T^\nu(1 - cos\Delta\phi^{e\nu})$, where $\phi^{e\nu}$ is the angle between the electron and neutrino).

The $Z \rightarrow ee$ sample is frequently used in this analysis to check for effects that may influence the asymmetry measurement. It originates from the $Z$ electron datasets passing the following Level 3 $Z$ electron trigger, "CEM_22_Z". They are selected by requiring:

**First electron candidate:**
$Found\ in\ the\ CEM$
$E_T > 22\ GeV$
$P_T > 13\ GeV$
$E_{Had}/E_{EM} < 0.10$
**Second electron candidate:**
$E_T > 20,\ 15,\ 10\ GeV$ in CEM, PEM or FEM respectively
$\chi^2_{PEM} < 3.0$ if in the PEM
$E_{Had}/E_{EM} < 0.05$.

Both $W$ and $Z$ events are corrected for CTC wire mis-alignment determined from central $W \rightarrow e\nu$ events. This correction is discussed in a later section of this chapter.

## Central $W \rightarrow \mu\nu$ Event Selection

The cuts made on the event variables $E_T^{jet}$, $P_T^{high}$, $CurSig$, $Z_0$ and $Z_0^{CTC}$ are the same as in the central $W \rightarrow e\nu$ analysis. In the following, we only list the variables

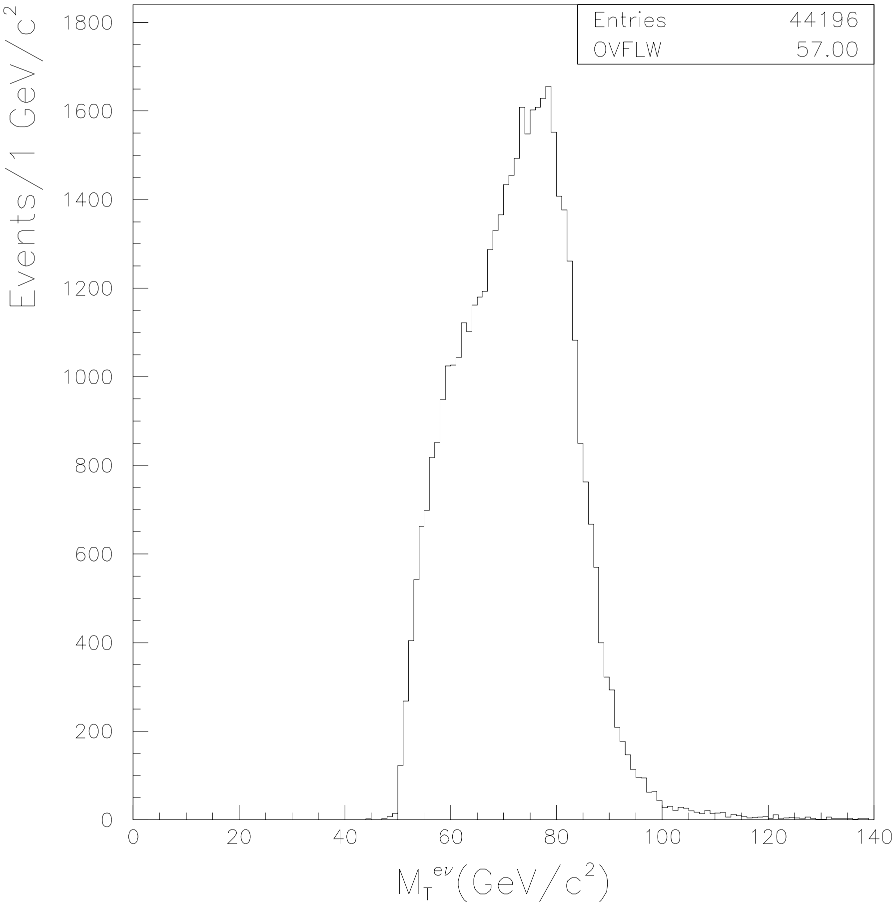

Figure 3.1: The transverse mass spectrum of central electron $W$ candidate events.

that are specific for muon analysis.

**25 GeV $< P_T <$ 150 GeV:** The momentum of the CTC track is required to be less than 150 GeV to allow the charge to be determined with high certainty. This is slightly lower than electron analysis since cosmic ray background which are rarely present in the electron sample, tend to appear in the muon sample as high $P_T$ tracks.

**$\not{E}_T >$ 25 GeV:** The $\not{E}_T$ is calculated (see Equation 3.2) after removing the energy contained in the calorimeter tower traversed by the muon and then adding the muon's $P_T$, as measured by the CTC, to the $E_T$ in the calorimeter.

**$Isolation <$ 0.1:** Isolation is defined as

$$Isolation = \frac{E_T(0.4) - E_T^{\mu tower}}{P_T^{\mu}} \tag{3.7}$$

where $E_T(0.4) - E_T^{\mu tower}$ is the energy in a cone of radius $R = 0.4$ in $\eta - \phi$ space minus the energy in the tower traversed by the muon. $P_T^{\mu}$ is the muon's transverse momentum.

**$E_{Had} <$ 6 GeV, $E_{EM} <$ 2 GeV and $E_{EM} + E_{Had} >$ 0.5 GeV:** The energy in the calorimeter tower (both EM and hadronic sections) traversed by the muon is required to be consistent with a minimum ionizing particle.

**CMU $|\delta X| <$ 2.0 cm, CMP $|\delta X| <$ 5.0 cm and CMX $|\delta X| <$ 4.0 cm:** The difference between the position in $X$ of the reconstructed muon stub and the extrapolated CTC track is required to be less than 2.0, 5.0 and 4.0 cm when the muon is found in the CMU, CMP and CMX respectively.

**$|Z_0^{VTX} - Z_0^{track}| <$ 5 cm:** The $z$ coordinate of the intercept of the track and the beamline is required to be within 5 cm of the event vertex as determined by the VTX. This cut helps remove cosmic rays and decays in flight.

After the above selection, a total of 25538 events remain in the central $W \rightarrow \mu\nu$ sample. Figure 3.2 shows the transverse mass spectrum of the central muon $W$ candidate events.

## 3.3 $W$ Backgrounds

$W$ candidates are selected with a signature of an isolated electron and $\not{E}_T$. This signature can also be mimicked by other physics processes. The QCD process ($p\overline{p} \rightarrow\ 2\ jets$) can lead to $W$ backgrounds when a hadron jet containing the electron or muon fluctuates so that it appears to be an isolated electron or muon, the $\not{E}_T$ comes about if the other jet is mismeasured (its energy is measured low) or it falls into an uninstrumented region of the detector. The decays of $Z \rightarrow l^+l^-$ or $Z \rightarrow \tau^+\tau^- \rightarrow l^\pm\nu\nu X$ can be misidentified as $W$'s if one lepton (muon or electron) is detected and the other lepton falls into an uninstrumented region of the detector (or the neutrinoes from $\tau$ decays are sufficiently energetic). The $W \rightarrow \tau^\pm\nu \rightarrow l^\pm\nu\nu$ can also fake $W \rightarrow l^\pm$ signals.

### QCD Backgrounds

The electron in the hadron jets fall into three categories: (1) electrons which come in $e^+e^-$ pairs, either from a photon conversion or from Dalitz decays; (2) electrons from heavy quark decays such as $b \rightarrow ce\nu\ or\ c \rightarrow se\nu$; (3) hadrons that fake electrons, for example, a charged particle track ($\pi^\pm$) overlapping with $\pi^o$. Note the conversion electrons have been explicitly removed by searching for a second track which, when combined with the primary electron track, is consistent with coming from the conversion of a photon into an $e^+e^-$ pair. This condition is determined by

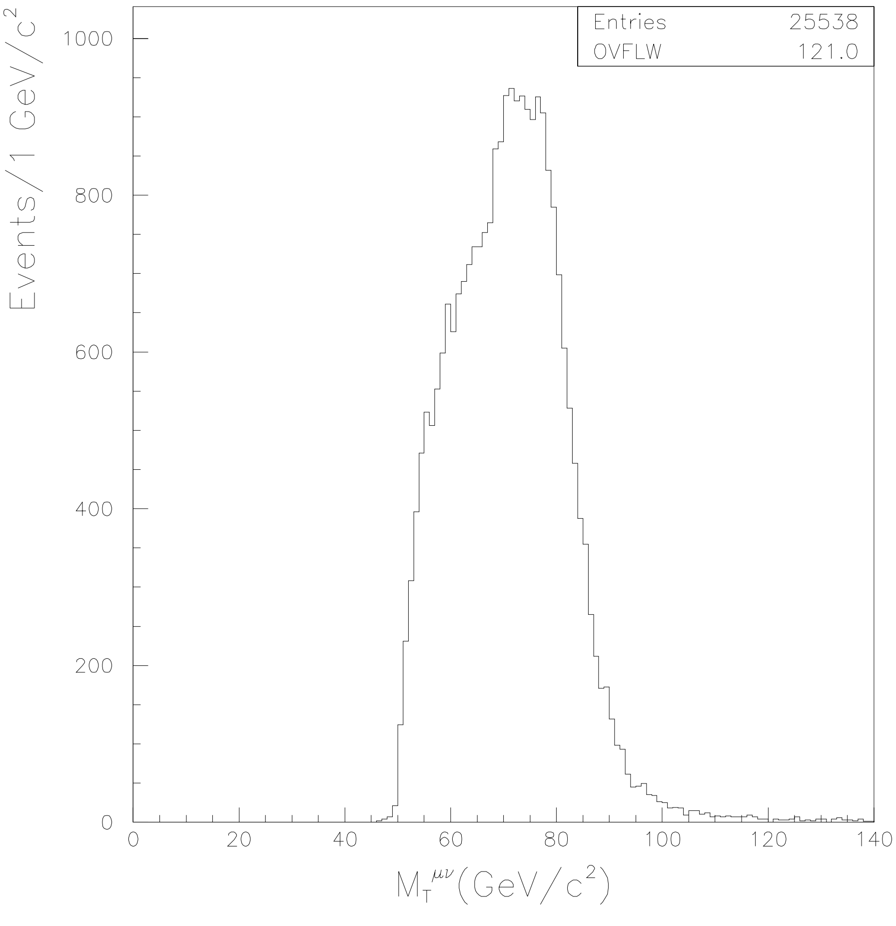

Figure 3.2: *The transverse mass spectrum of central muon W candidate events.*

pairing the electron track with all other tracks of opposite charge. Two conditions are then checked for each pair of tracks: the difference $|\Delta cot(\theta)| < 0.06$ radians, and $S < 0.2$ cm, where $S$ is the distance, in the $x$-$y$ plane, between the tracks at the point where the two helixes are tangent.

The muon detectors are located behind 5 absorption length of material (CMP is after 8 absorption length of material). Muons contained inside a hadron jet are primarily from the decay-in-flight of charged pions or kaons into muons or charged hadron's "punch-through". Photon conversions into muons are much less likely than to electrons because of the high muon mass.

The method of estimating the QCD background in the central $W$ electron sample is explained in the following. The same method is used to estimate the QCD background in the central $W$ muon sample. We start by selecting a sample of non-$W/Z^o$ electrons from the inclusive central electron sample. Events which have a second cluster which passes cuts of $Had/EM < 0.1$ and $Isolation < 0.1$ are removed in order to reject electrons from $Z \rightarrow e^+e^-$ and Drell-Yan pair production. Figure 3.3 shows the isolation vs $\not{E}_T$ distribution in the sample. Events which have $\not{E}_T >$ 10 GeV are rejected in order to remove electrons from $W \rightarrow e\nu$ or $W \rightarrow \tau\nu \rightarrow e\nu\nu\nu$ events. In addition, we require a hadronic jet with $E_T > 10$ GeV and electromagnetic fraction less than 0.8. This reduces the fraction of electrons from weak boson decays. This is the first control sample. For reasons which will be clear in the following section, we require further the hadronic jet with $E_T > 20$ GeV to form a second control sample which is a subset of the first control sample. We estimate the QCD background by extrapolating the isolation variable for the electron from a region away from the $W$ signal into the $W$ signal region. We identify four regions in the plot of isolation vs missing $E_T$ in Figure 3.3,

1) $Isolation < 0.1$ and $\not{E}_T < 10$ GeV and at least one other jet

2) $Isolation > 0.3$ and $\not{E}_T < 10$ GeV and at least one other jet

3) $Isolation > 0.3$ and $\not{E}_T > 25$ GeV

4) $Isolation < 0.1$ and $\not{E}_T > 25$ GeV.

The region 4) is the $W$ signal region. The requirement of one other jet in regions 1) and 2) is that one jet besides the jet containing the electron exists in the event. The cut, $Isolation > 0.3$, defines a region which is supposed to be signal free. In principle a $W$ decay electron could radiate at a large angle and thus appear non-isolated, resulting in an overestimate of the QCD background. This effect was investigated and it was found that the background estimation was stable with regard to this non-isolation criteria. The background in the signal region was then determined by:

$$\frac{QCD\,contamination}{\#Events\,in\,region\,3} = \frac{\#events\,in\,region\,1}{\#events\,in\,region\,2}(\quad From\,control\,samples)$$

under the assumption that $\not{E}_T$ and $Isolation$ are independent variables. Figure 3.3 shows the $Isolation$ distributions for the control samples and the signal sample. The same distributions for muons are shown in Figure 3.4 The average isolation for low $\not{E}_T$ is essentially flat, supporting the assumption used in this background estimation.

We create two control samples in order to take into account of the fact that the isolation of the electron on the one side of the QCD jet events is correlated with the magnitude of the jet $E_T$ on the other side of the event. Because the mismeasured jet $E_T$ is unknown, we average the results from two samples. The two control samples yielded backgrounds of $(0.88 \pm 0.11)\%$ and $(0.56 \pm 0.09)\%$ for central electrons. Taking the average of these numbers and interpreting the spread as a systematic uncertainty, the QCD related background was found to be $(0.7 \pm 0.2)\%$ of the central electron data sample. For the central muon sample, the two control samples give

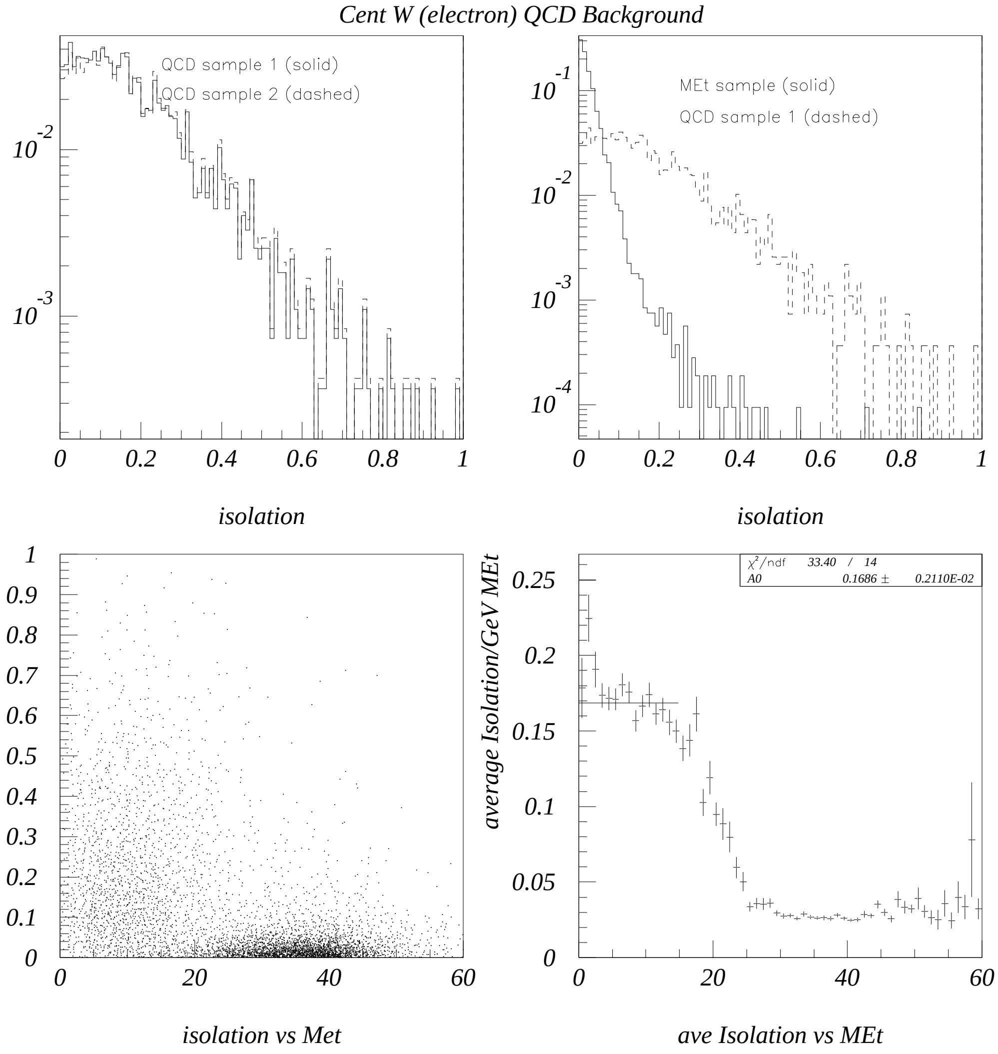

Figure 3.3: a) Isolation in a cone of $R$=0.4 (*Isolation*) for the two central $W$ QCD background samples, b) for the signal sample (minus the isolation cut) and the control sample 1. c) A scatter plot of *Isolation* vs $\not\!\!E_T$ in the inclusive central electron sample and d) the average *Isolation* as a function of $\not\!\!E_T$.

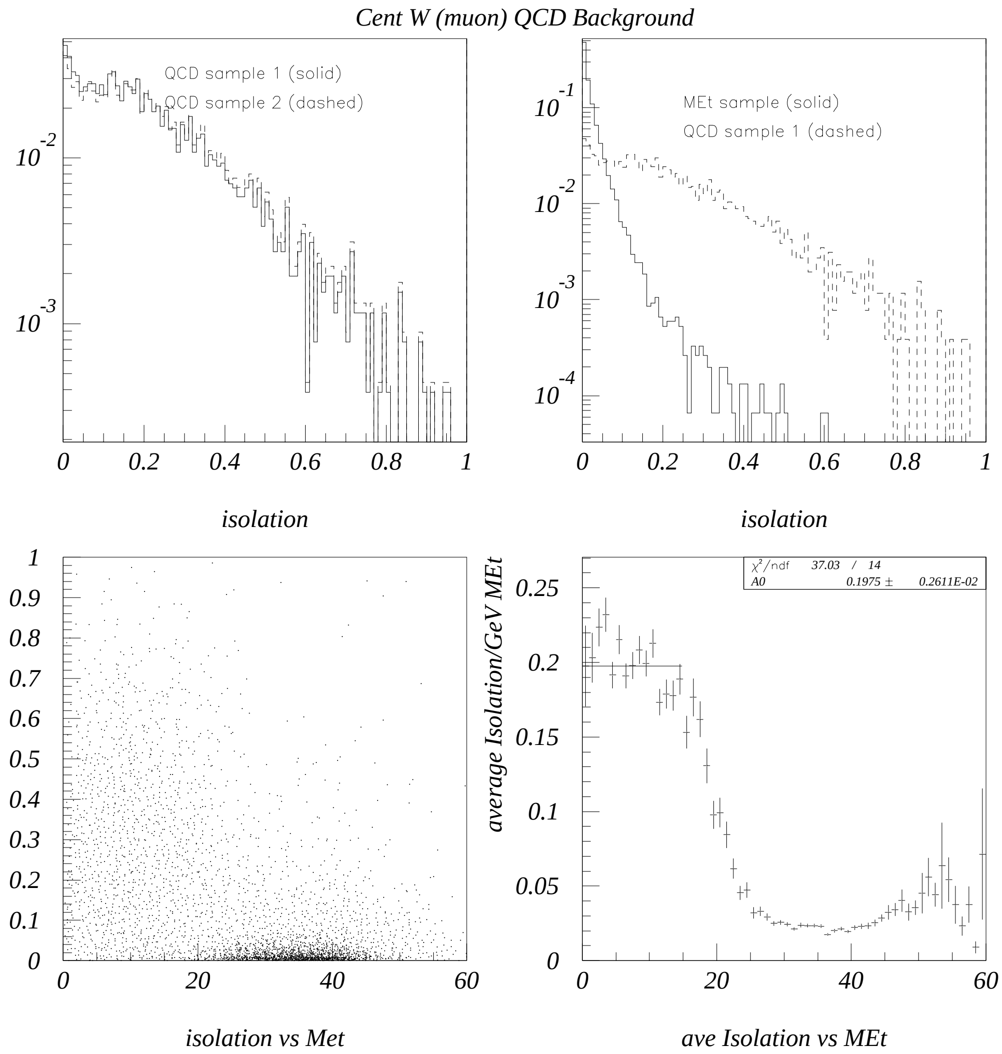

Figure 3.4: a) Isolation in a cone of $R$=0.4 (*Isolation*) for the two central $W$ QCD background samples, b) for the signal sample (minus the isolation cut) and the control sample 1. c) A scatter plot of *Isolation* vs $\not\!\!E_T$ in the inclusive central muon sample and d) the average *Isolation* as a function of $\not\!\!E_T$.

fractions of backgrounds as $(0.77 \pm 0.09)\%$ and $(0.42 \pm 0.07)\%$ respectively. The QCD background in the central $W$ muon sample is $(0.6 \pm 0.2)\%$.

### $W \rightarrow \tau\nu$

The fraction of background from the process $W \rightarrow \tau\nu \rightarrow l\nu\nu$ was estimated by a Monte-Carlo calculation. It correctly handled the polarization of the $\tau$ and $W$ and includes a simple detector simulation [15]. The same number of $W \rightarrow e/\mu + \nu$ and $W \rightarrow \tau\nu$ events are generated. The ratio of events passing the kinematic requirements in $\tau$ and $e/\mu$ samples defines the fraction of $W \rightarrow \tau\nu$ background. The fraction of $W \rightarrow \tau\nu$ background in the central $W$ electron and muon samples are estimated to be $(2.0 \pm 0.2)\%$. The 0.2% systematic error is due to choice of input PDFs.

### $Z \rightarrow ll$

The fraction of background from $Z \rightarrow l^+l^-$ $(l = \mu \; or \; e)$ is estimated by a Monte Carlo generator, HERWIG [16], plus the CDF detector simulation. In the $W$ electron data analysis, the events with invariant mass of the electron candidate and any other EM cluster between 60 GeV and 120 GeV are already removed. The additional requirement of $P_T^{high} < 10$ GeV greatly reduces $Z \rightarrow ee$ events. These cuts are very effective considering the large calorimeter coverage for electrons $(|\eta| < 4.2)$. For $Z \rightarrow \mu\mu$ events, muons at high detector rapidities are not fully detected by the CTC tracking. The cut $P_T^{high} < 10$ GeV becomes less effective for detecting muons at high detector rapidities $(|\eta| > 1.2)$ (The CTC tracking efficiency falls quickly as a function of detector rapidity $|\eta|$). As a result, a higher background in the muon sample is expected. We generate $W \rightarrow l\nu$ and $Z \rightarrow ll$ events in equal luminosity. The fraction (%) of $Z$ events passing all requirements relative to $W$ events is determined. It is found that the $Z \rightarrow ee$ background is $(0.18 \pm 0.01)\%$ of the central $W$ electron sample. The $Z \rightarrow \mu\mu$ background is $(4.7 \pm 0.7)\%$ of the central $W$ muon sample.

### $Z \rightarrow \tau^+\tau^-$

$Z \rightarrow \tau^+\tau^-$ events can fake a $W$ when one of the $\tau$'s decays to an electron (or muon) or its hadronic decay fakes an electron (muon). Again the HERWIG Monte Carlo generator and detector simulation were used and the total number of $Z \rightarrow \tau^+\tau^-$ events passing the selection cuts normalized to the generated $W$ sample. The background is estimated to be $(0.07 \pm 0.01)\%$ of the central $W$ sample.

## Cosmic Ray

If a cosmic ray muon passes near the beam line, it can look like a dimuon event. Such events are characterized by two back-to-back tracks which are out of time as measured by hadron calorimeter TDC's, because they do not originate from the $z$ axis. Often one of the muon tracks (entering track) is not found or has its momentum badly mismeasured because reconstruction code thinks it as originating from the $z$ axis thus time of flight correction is backwards. This results large missing transverse energy and therefore the cosmic ray muon can fake a $W$ muon event. The muon candidates in the central $W$ muon sample are further required to pass the CDF cosmic ray filter [17, 18]. The CDF cosmic ray filter removes the cosmic ray by rejecting events with a 2D or 3D CTC track $P_T > 10$ GeV and track azimuthal $\phi$ within $2^o$ of the identified muon track. This removed most of the cosmic ray background. The cosmic ray background in the central $W$ muon sample is further reduced by the offline cuts $P_T^{high} < 10$ GeV, the CTC track impact parameter $|D_o| < 0.2$ cm cut, and $|Z^o_{vtx} - Z^o_{track}| < 5$ cm cut.

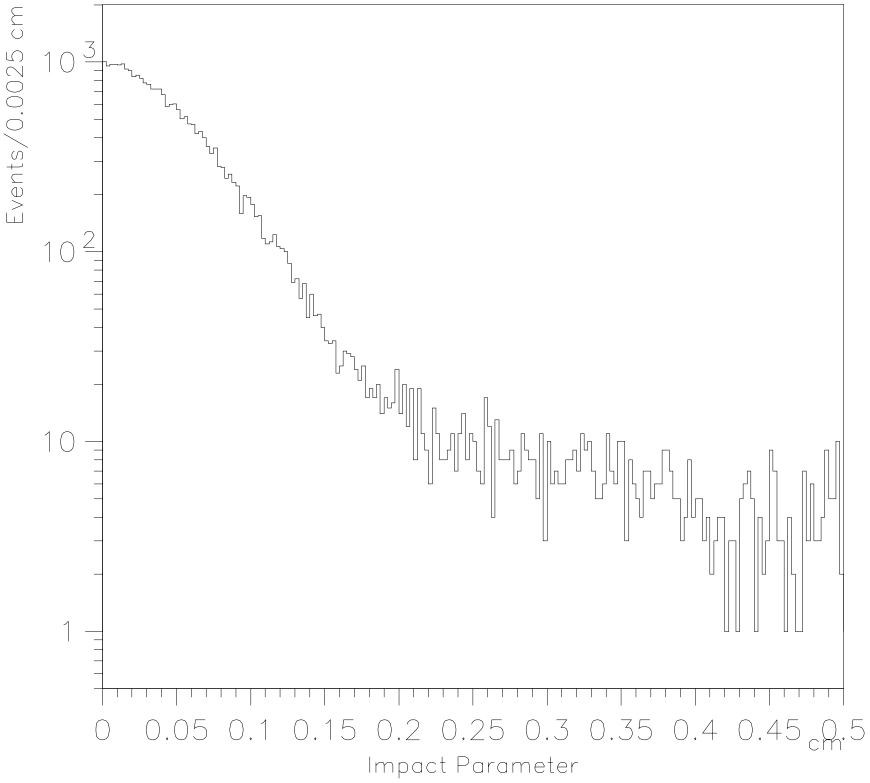

Figure 3.5: *The impact parameter distribution of central $W$ muon candidate events.*

Because the cosmic ray muons do not originate from the $z$ axis. The track impact parameter $D^o$ has a flat distribution while the real $W$ muon events tend to peak at $z$ axis. This fact is used to estimate the fraction of cosmic ray muons remaining in the $W$ muon sample. Figure 3.5 shows the impact parameter distribution of the $W$ muon events after releasing the impact parameter cut. Because the real $W$ muon events with poorly measured associated CTC tracks can have large impact parameter value, these events appear at the tail in Figure 3.5. This can result in an over-estimate of the cosmic ray background. To identify these events from the cosmic ray muons, a sub-sample of events with $|D^o| > 0.2$ cm in the $W$ muon sample were visually inspected. Out of 240 events with $|D^o| > 0.2$ cm scanned (the total number is 835), only 24 were identified as cosmic ray background. The number of cosmic ray events in the $W$ muon data sample is estimated to be $(33 \pm 7)$. The fraction of the background in the $W$ sample is $(0.13 \pm 0.03)\%$ and thus its effect to the charge asymmetry is negligible.

## 3.4 Momentum and Energy Scale

We note in chapter 1 that the $W$ lepton charge asymmetry is a function of lepton transverse energy cut. The transverse energy of central electrons ($E_T$) is measured by the CEM, and that of the central muons ($P_T$) is measured by the curvature of the associated CTC track inside the solenoidal magnetic field. Here the approximation $P_T \approx E_T$ for muons is made as the mass of muons is negligibly small compared to the energy of the leptons from $W$ decays. The uncertainty in both the CTC momentum scale and the CEM's energy scale will affect the lepton charge asymmetry measurement. The CTC momentum scale depends on the magnetic field which is monitored by the electric current in the solenoid. It is checked using $J/\psi \to \mu\mu$ events against the the world average value. A fit to the $J/\psi$ mass shows that it is known to be accurate to 0.1% [11]. It is worth noting that the $\gamma$ radiated by muons traversing the detector material is not measured in the CTC track momentum. This results in a muon momentum which is systematically lower by an average of 100 MeV. Most of the $\gamma$ radiation by electrons, however, is accepted by the calorimeter towers. This effect is fully taken into account by the quoted momentum scale uncertainty.

The electron shower produces light in the scintillator. The light is collected from either side of the tower in azimuth and measured by phototubes. For each CEM tower, the geometric mean of the charge from the two phototubes is used as the measure of energy. This reduces gain dependence on local shower position due to light attenuation in the scintillator. The central electron energy cluster is formed by a "seed" tower which has the biggest transverse energy in the cluster and two "shoulder" towers on either side in the polar direction. In the case when the cluster crosses the $\eta = 0$ boundary, only one "shoulder" tower is included in the cluster. The energy of the cluster is the sum of "seed" and "shoulder" tower energies. A few corrections are made on the cluster energy. The mapping correction derived from the testbeam data flattens out the energy response within an individual tower. A tower-to-tower gain variation is corrected based on the E/P calibration using central $W$ electron data. The same E/P calibration is also used to derive CEM's time dependence due to aging effects present in the scintillator. After these corrections, a global energy scale correction factor determined from Central-Central $Z \rightarrow ee$ events is applied to bring CEM's overall energy scale to within 0.5% of $Z$ mass. Figure 3.6 shows the $Z$ mass distributions measured from a sample of Central-Central $Z \rightarrow ee$ events after the above energy corrections. The mean from a fit to the $Z$ mass distribution is $91.42 \pm 0.08$ GeV suggesting that the CEM energy scale is correct to within 1% (the PDG $Z$ mass value is at $91.187 \pm 0.007$ GeV).

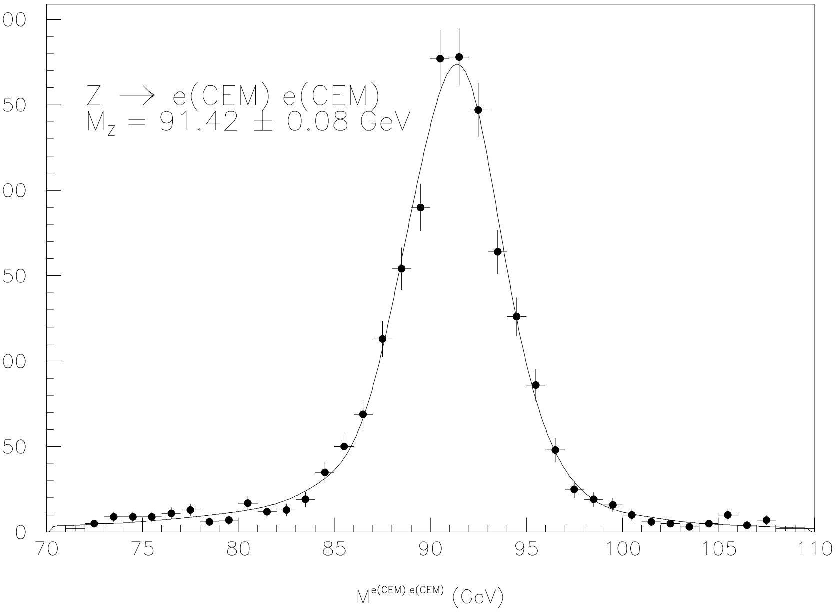

Figure 3.6: The invariant mass distribution measured from a sample of Central-Central $Z \rightarrow ee$ events. The data are fit with $Z \rightarrow ee$ Monte Carlo with radiative correction taken into account. The detector simulation is included in the Monte Carlo.

A 1% energy scale uncertainty is taken knowing that for muons the momentum scale is known to be better than 1%. This is to be consistent with the electron analysis as this 1% uncertainty causes only small systematic error in the lepton charge asymmetry.

## 3.5 The Charge Identification

The charge of central electrons and muons is identified by the direction in $\phi$ (increasing or decreasing $\phi$ direction) in which their associated CTC track bends.

| Variable | Cut value |
|---|---|
| $Z$ mass | $> 81$ and $< 101$ |
| **First Leg:** | |
| $E_T$ | $> 25$ GeV |
| $P_T$ | $> 13$ GeV |
| $E_{Had}/E_{EM}$ | $< 0.055 + 0.00045 * E$ |
| $Isolation$ | $< 0.1$ |
| $LShr$ | $< 0.2$ |
| $\chi^2_s$ | $< 10$ |
| $E/P$ | $< 1.8$ |
| $E/P$ | $> 0.5$ |
| $\delta X$ | $< 1.5$ |
| $\delta Z$ | $< 3.0$ |
| **Second Leg:** | |
| $W$ cuts | |
| **Both legs:** | |
| $\|Z_0\|$ | $< 60$ cm |
| common vertex | $\|\Delta Z_0\| < 10$ cm |
| $CurSig$ | $< 2.0$ |
| Conversion Cut | |

Table 3.1: $Z \to e^+e^-$ I.D. Cuts.

Because of the fine CTC momentum resolution ($\frac{\delta P_T}{P_T} = 0.0010 \times P_T$ in GeV/c with beam constraint track fit), the charge of leptons from $W$ decay is determined with high certainty. However, a small rate of charge mis-identification is expected for electrons from the mis-association of CTC tracks to the energy cluster. These tracks typically come from $e^+e^-$ pair conversion of radiated photons which tend to be close to the primary electron. Because the existence of charge mis-identification dilute the asymmetry, the rate needs to be estimated. The Central-Central $Z$ sample is used to estimate the rate of charge mis-identification. The events passed the cuts listed in Table 3.1. From the rate of same-sign $Z \to ee$ events, the charge mis-identification rate in the central region is determined to be $(0.2 \pm 0.1)\%$, which is of negligible effect on the asymmetry measurement.

## 3.6 CTC Wire Misalignment Correction

The charge asymmetry may be introduced by a charge dependence of lepton $P_t$ measurement. This happens when there is "false curvature" in the tracking chamber from a residual misalignment of the CTC wire positions. The result is to increase the measured momentum of one charge while decreasing the other charge thus introducing the asymmetry via lepton $P_t$ cut. In the electron case, this effect is minimal because $P_t$ cut is at 13 GeV away from the $E_T > 25$ GeV cut. In the muon analysis, $P_t$ cut is 25 GeV and therefore a correction is needed.

The following equations were used to correct the measured $P_T$ and $E/P$ for the false curvature in the CTC:

$$\begin{aligned} P_T^{cor} &= P_T/(1 - charge * P_T * KdC(x)) \qquad (3.8) \\ \left(\frac{E}{P}\right)^{cor} &= \frac{E}{P} * (1 - charge * P_T * KdC(x)) \\ KdC(x) &= \frac{1}{2\langle E_T\rangle}\Delta\langle E/P\rangle^{\pm}(x) \end{aligned}$$

where $\langle E_T\rangle = 36.0$ GeV is the average $E_T$ of the $W$ leptons, and $KdC(x)$ is a constant, $K = 1/(0.0000149898 * 14.116)$, times the false curvature, $dC$, which is a function of $\eta$ and $\phi$. The false curvature coefficients $KdC(\eta)$ and $KdC(\phi)$ were derived from the central $W$ electron data sample using the $E/P$ method. The top two plots in Figure 3.7 show the measured CTC false curvature as a function of $\eta$ (pseudo-rapidity) and $\phi$ from the difference in $E/P$ for positive and negative charges from central electrons in the asymmetry sample. A linear approximation is used to describe the "false curvature" as a function of $\eta$ which is believed to have come from a twist of the CTC endplates in $\phi$ . The $\phi$ dependence

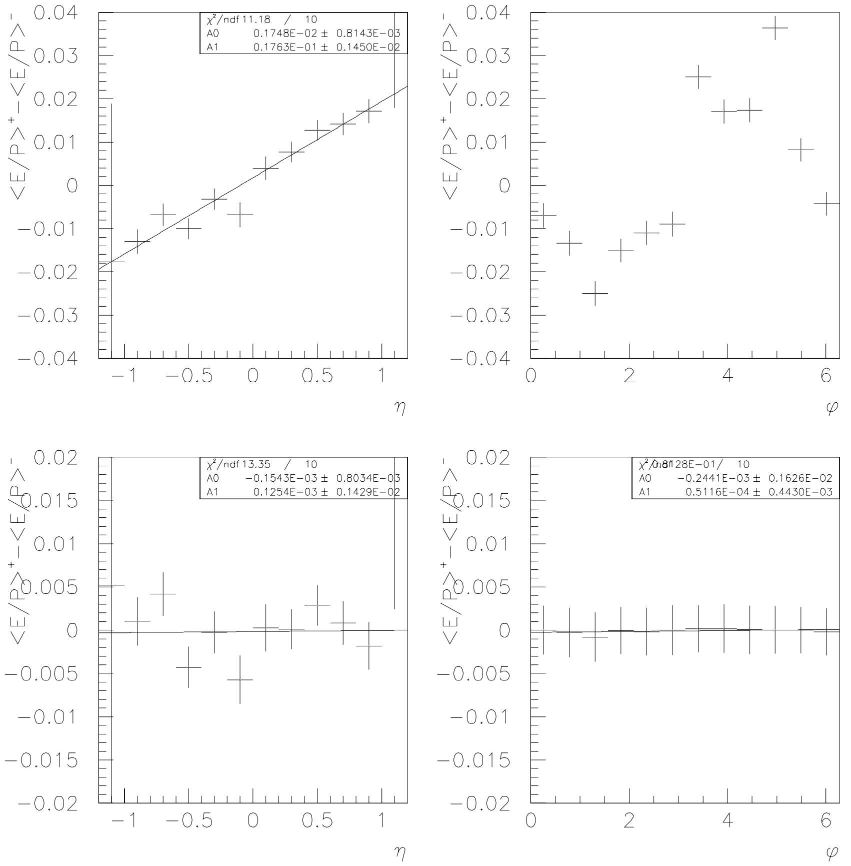

Figure 3.7: The difference $\langle E/P^{+}\rangle - \langle E/P^{-}\rangle$ , as a function of $\eta$ and $\phi$, is directly related to the false curvature. The top two figures show the false curvature before any corrections while the bottom two show the false curvature after the $\phi + \eta$ dependent corrections.

| $\phi^o$ | $\Phi(\phi)$ | $\phi^o$ | $\Phi(\phi)$ |
|---|---|---|---|
| 0-30 | -0.00739 | 180-210 | 0.02657 |
| 30-60 | -0.01537 | 210-240 | 0.01890 |
| 60-90 | -0.02691 | 240-270 | 0.01925 |
| 90-120 | -0.01644 | 270-300 | 0.04010 |
| 120-150 | -0.01190 | 300-330 | 0.00971 |
| 150-180 | -0.01018 | 330-360 | -0.00463 |

Table 3.2: The coefficients determined from the difference in the $E/P$ distributions for central $e^+$ and $e^-$ in the asymmetry sample.

of the "false curvature" is thought to have originated from mis-alignment of 12 $30^o$ segments during the construction phase of the CTC. These CTC segments in $\phi$ corresponds to 12 precision alignment holes on CTC. A look-up table of 12 $\phi$-dependent coefficients is constructed from the data. Table 3.2 lists the magnitude of the false curvature in $\phi$ . The bottom two plots in Figure 3.7 shows that the $\eta$ and $\phi$-dependent CTC false curvatures are removed after the corrections. It's worth noting that the corrections in $\phi$ and $\eta$ are actually independent of each other. The magnitude of this correction to the measured CTC momentum is less than 1.5%.

## 3.7 Charge Independence Verifications

Experimentally the lepton charge asymmetry (defined in Equation 1.1) is calculated as:

$$A(y_l) = \frac{N^+ - N^-}{N^+ + N^-} \qquad (3.9)$$

where $N^+$ ($N^-$) are number of positively (negatively) charged leptons in a particular lepton rapidity bin. This is based on the assumption that acceptance and efficiency are independent of lepton charge. It is important to verify that the assumption is valid.

### Detector Acceptance

The detector acceptance of leptons is mainly a function of detector rapidity. The charge dependence of detector acceptance for leptons can come if positively and negatively charged leptons populate different detector rapidity region. Tables 3.3 and 3.3 compares the mean and rms of detector rapidity $\eta$ distributions for positively and negatively charged leptons in the final asymmetry sample. No charge dependence of detector acceptance is evident.

### Identification Efficiencies

A charge asymmetry may be caused by a charge-dependent lepton identification requirements. To verify that the lepton identification cuts are independent of charge, a pure sample of $W$ events is selected by requiring $\not{E}_T > 30$ GeV, $E_T > 30$ GeV, $M_T^W < 100$ GeV and the highest $E_T$ jet $< 5$ GeV as well as fiducial cut in the electron case. No charge dependence of the identification cuts is evident from the distributions of the electron and muon identification variables for this sample of good $l^+$'s and $l^-$'s from $W$ decays as shown in Figure 3.8 and Figure 3.9.

### Central $W$ $e/\mu$ Triggers

The central $e/\mu$ triggers affect the asymmetry measurement in two ways. First, if the trigger efficiency is charge-dependent, a charge asymmetry would arise. Secondly, an $E_T$ or $P_T$-dependent lepton trigger efficiency can change the lepton asymmetry through the asymmetry dependence on the transverse energy cut of leptons.

The Level 1 triggers for central $W$ electrons have small $E_T$ threshold (8 GeV)

| *Event $\eta$* | *Detector $\eta$* | | | |
|---|---|---|---|---|
| | *Positive Charges* | | *Negative Charges* | |
| | *mean* | *rms* | *mean* | *rms* |
| 0.0~ 0.2 | 0.129 | 0.159 | 0.130 | 0.150 |
| 0.2~ 0.4 | 0.315 | 0.132 | 0.318 | 0.130 |
| 0.4~ 0.6 | 0.508 | 0.134 | 0.505 | 0.134 |
| 0.6~ 0.8 | 0.699 | 0.121 | 0.702 | 0.122 |
| 0.8~ 1.0 | 0.862 | 0.087 | 0.860 | 0.088 |
| 1.0~ 1.2 | 0.946 | 0.044 | 0.944 | 0.046 |
| 0.0~ -0.2 | -0.111 | 0.159 | -0.115 | 0.158 |
| -0.2~ -0.4 | -0.302 | 0.136 | -0.310 | 0.132 |
| -0.4~ -0.6 | -0.489 | 0.136 | -0.489 | 0.135 |
| -0.6~ -0.8 | -0.686 | 0.123 | -0.689 | 0.124 |
| -0.8~ -1.0 | -0.861 | 0.091 | -0.852 | 0.094 |
| -1.0~ -1.2 | -0.947 | 0.045 | -0.939 | 0.046 |

Table 3.3: Comparison of the mean and rms of detector rapidity distributions for positively and negatively charged electrons in the final asymmetry sample.

| *Event $\eta$* | *Detector $\eta$* | | | |
|---|---|---|---|---|
| | *Positive Charges* | | *Negative Charges* | |
| | *mean* | *rms* | *mean* | *rms* |
| 0.0~ 0.2 | 0.146 | 0.145 | 0.139 | 0.146 |
| 0.2~ 0.4 | 0.312 | 0.143 | 0.308 | 0.144 |
| 0.4~ 0.6 | 0.454 | 0.117 | 0.456 | 0.125 |
| 0.6~ 0.8 | 0.722 | 0.116 | 0.724 | 0.113 |
| 0.8~ 1.0 | 0.861 | 0.087 | 0.864 | 0.083 |
| 1.0~ 1.2 | 0.928 | 0.054 | 0.911 | 0.046 |
| 0.0~ -0.2 | -0.117 | 0.152 | -0.130 | 0.147 |
| -0.2~ -0.4 | -0.285 | 0.144 | -0.284 | 0.145 |
| -0.4~ -0.6 | -0.441 | 0.125 | -0.443 | 0.123 |
| -0.6~ -0.8 | -0.705 | 0.117 | -0.712 | 0.117 |
| -0.8~ -1.0 | -0.852 | 0.092 | -0.855 | 0.090 |
| -1.0~ -1.2 | -0.926 | 0.046 | -0.917 | 0.047 |

Table 3.4: Comparison of the mean and rms of detector rapidity distributions for positively and negatively charged muons in the final asymmetry sample.

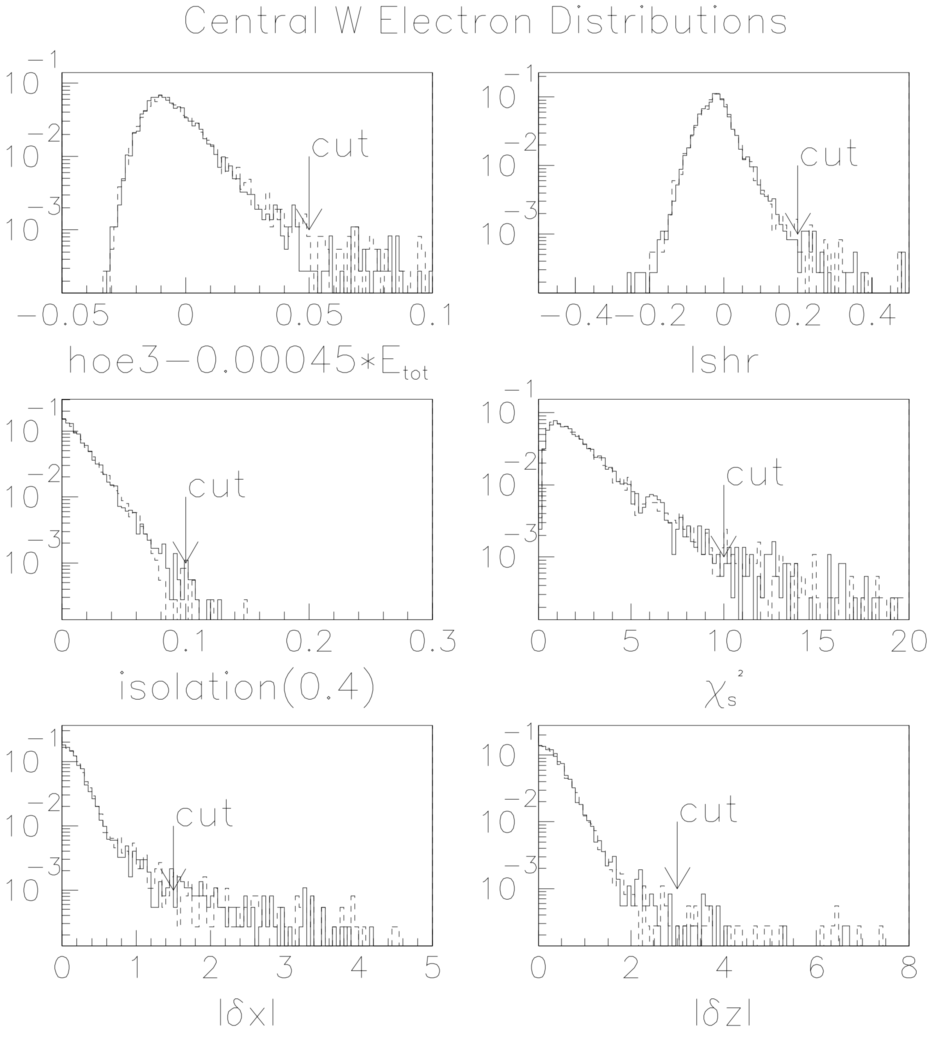

Figure 3.8: Distributions of the central $e$ identification variables for a pure sample $W$ decay electrons. The solid histograms are for $e^+$ and the dashed for $e^-$, as expected the distributions are the same for the two charges.

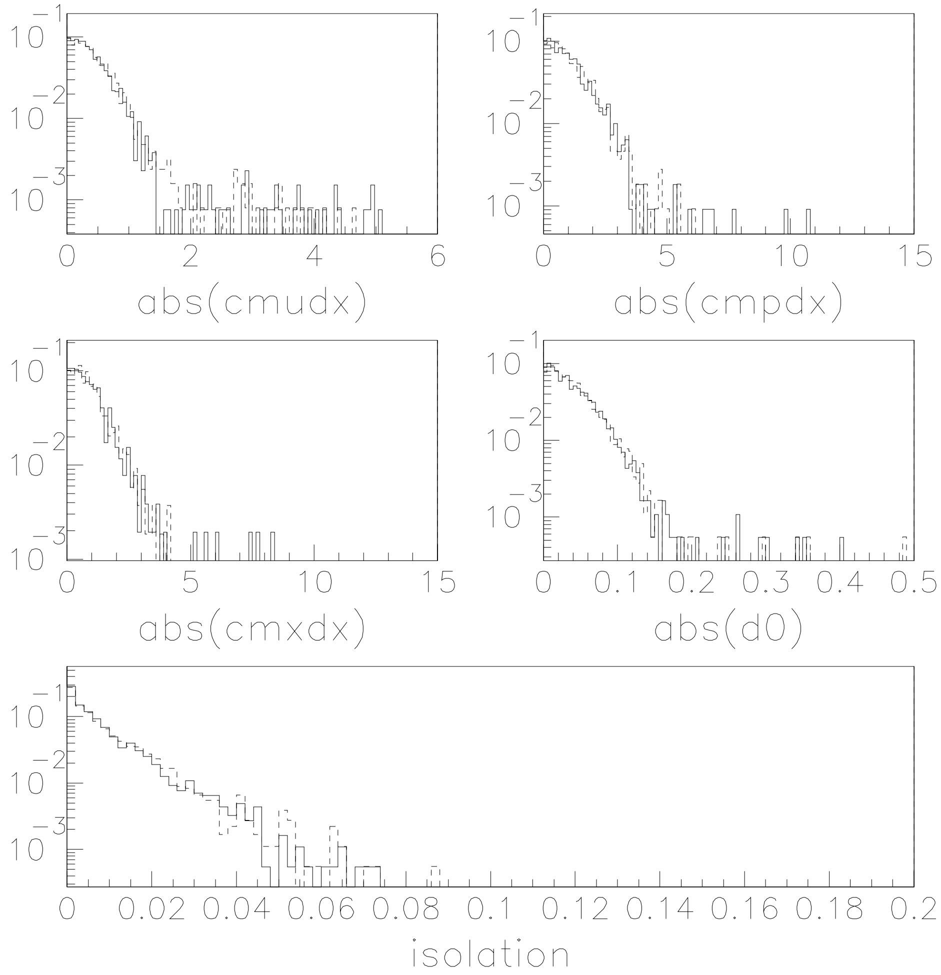

Figure 3.9: Distributions of the central $\mu$ identification variables for a pure sample of $W$ decay muons. The solid histograms are for $\mu^+$ and the dashed for $\mu^-$, as expected the distributions are the same for the two charges.

and only muon stub information is employed in the muon Level 1 triggers. Therefore, the above factors are not expected to affect the lepton asymmetry.

The primary $W$ electron trigger at Level 2 is "MET_20_CEM_16" which requires $\not{E}_T > 20$ GeV and $E_T > 16$ GeV. No charge dependence is expected because only calorimetry information is used. Figure 3.10 shows the $E_T$ dependence of trigger "MET_20_CEM_16". For electrons with $E_T > 25$ GeV, it is not fully efficient near the threshold. However, because Level 2 electron triggers are logically "OR-ed" with a few low $E_T$ electron triggers. The actual Level 2 trigger efficiency is flat as a function of $E_T$ as shown in Figure 3.11 The primary $W$ muon triggers at Level 2 require the CFT $P_T > 12$ GeV. There is a backup central electron trigger "CEM_16_CFT_12" which requires electron $E_T > 16$ GeV and CFT $P_T > 12$ GeV. Figure 3.12 shows the measured CFT trigger efficiencies from central $W$ electrons. The overall trigger efficiency is about 92% and it is flat as a function of track $P_T$ and there is no observed charge-dependence.

The Level 3 $W$ triggers have also been checked for any $E_T$ and charge dependence and no such dependence is found [19]. As a result, no corrections for a possible charge bias in the triggers are needed.

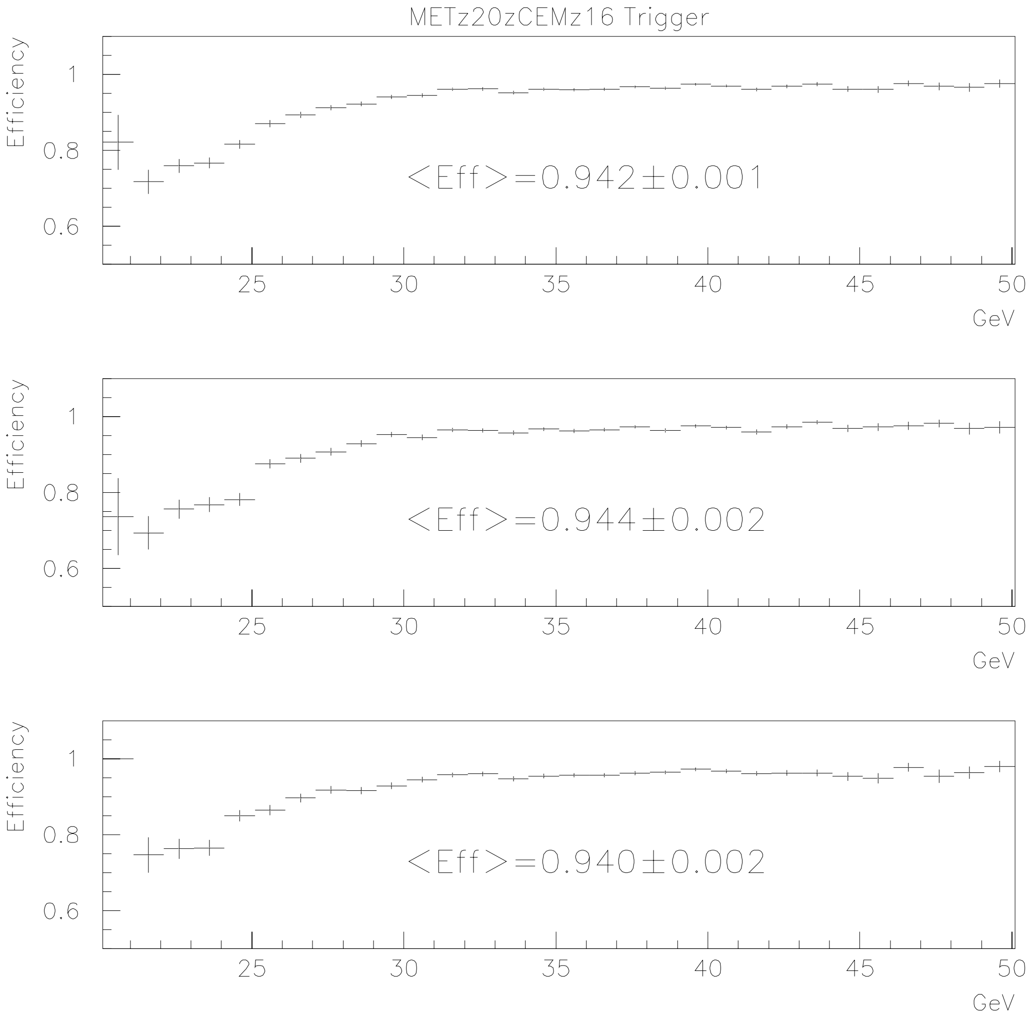

Figure 3.10: The efficiency of "MET_20_CEM_16" trigger. The bottom two plots are the corresponding trigger efficiencies for electrons on East ($\eta > 0.$) and West ($\eta < 0.$) detectors separately. No systematic differences are found for East and West part of the detectors.

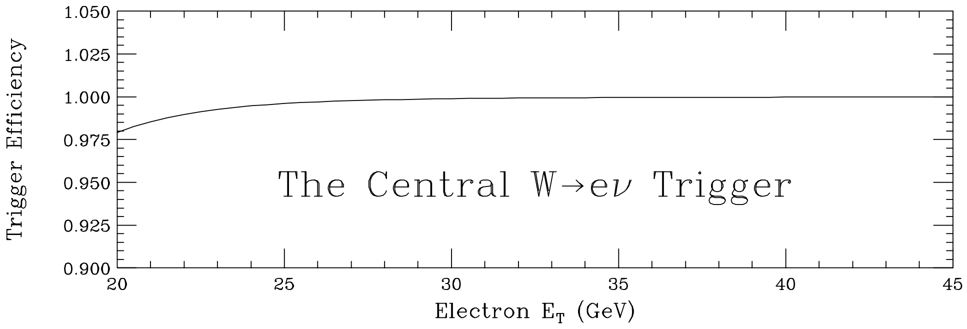

Figure 3.11: The efficiency of logically "OR-ed" central electron triggers is essentially flat as a function electron $E_T$.

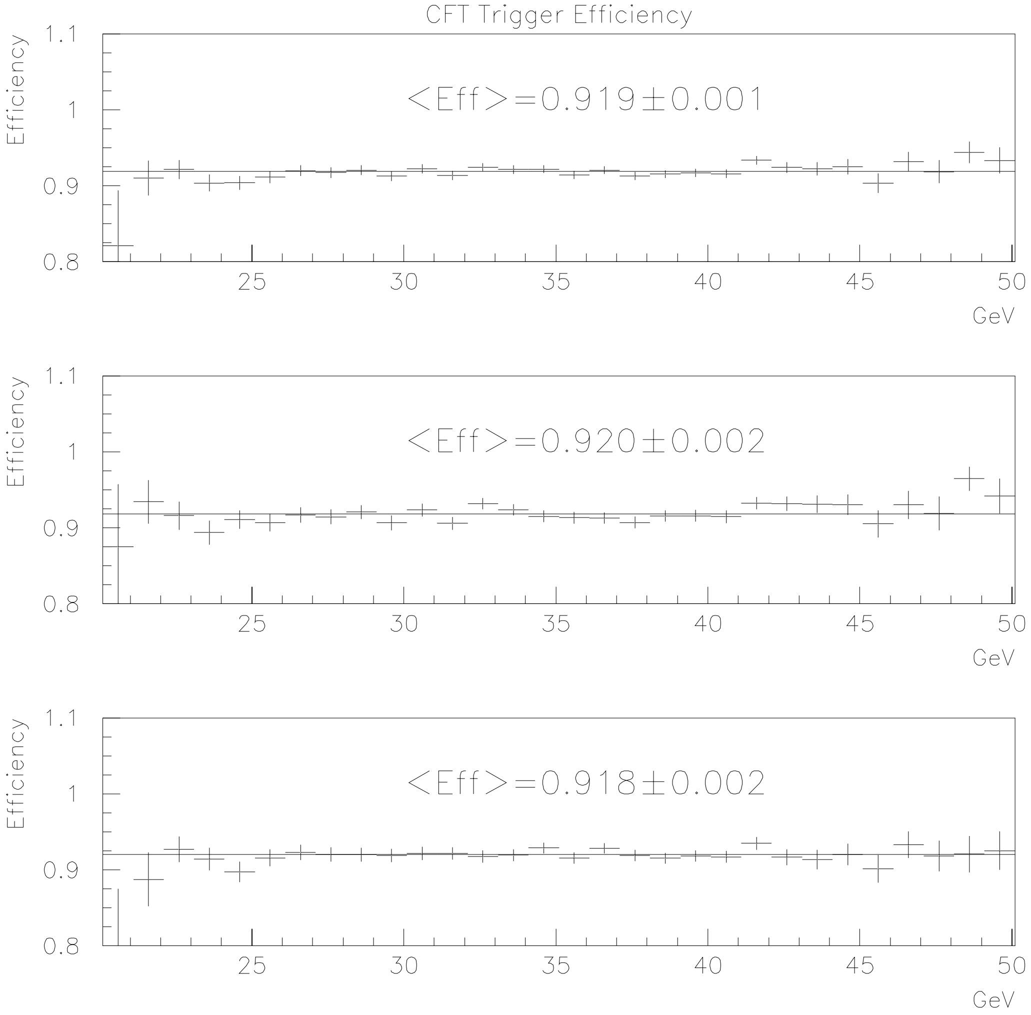

Figure 3.12: The efficiency of "CFT_12" trigger. The top plot shows the trigger efficiency for the combined plus and negative charges. The Bottom two are for the positively and negatively charged tracks. They are flat as a function track $E_T$, and there is no charge dependence in the efficiencies.

# Chapter 4

# Plug $W \rightarrow e + \nu$ Data Analysis

The plug $W$'s are used for which the decay electrons (or positrons) are detected by the Plug Electromagnetic Calorimeter (PEM). The plug data are important for the asymmetry analysis, because plug electrons from $W$ decays are at higher lepton rapidity than central electrons. The charge asymmetry at high lepton rapidity contains information about proton structure functions at smaller values of $x$. Furthermore, the plug data cover over 1 unit of lepton rapidity, about the same range of rapidity covered by the central $W$ data.

In addition to the five fold increase in data over that of the previous analysis [20], introduction of a new charge determination technique using the SVX in conjunction with the PEM shower centroid measurement doubles the amount of usable plug data and extends the measurement to higher lepton rapidity (up to $|y_l| = 2.4$). This is because the charge determination method using only CTC tracks suffers from a steeply falling track finding efficiency at high detector rapidity and can not be used for electrons or positrons with $|\eta| > 1.8$.

## 4.1 Plug Electron Reconstruction

A typical plug $W$ event, as shown in Figure 4.1, consists of a large, isolated PEM energy cluster plus missing transverse energy. Therefore, the principal part of the plug $W$ event analysis is the reconstruction of the plug electron. This includes finding the energy cluster, measuring the cluster energy and the cluster locations in both $\eta$ and $\phi$, and determining the lepton charge.

### 4.1.1 Plug Electron Clustering

The offline reconstruction of plug electrons starts with the PEM towers that have energy deposits above a certain preset energy threshold. "Seed" towers – towers with $E_T$ bigger than some threshold (typically 3 GeV) and with hadronic to electromagnetic energy ratio less than 0.125 are first identified and ordered according to the magnitude of their transverse energy ($E_T$). The cluster-finder starts with the tower with the biggest $E_T$, forming clusters by adding adjacent towers to the seed tower till the cluster reaches a preset cone size ($3 \times 3$ towers in $\eta - \phi$ for the PEM clusters). Towers that are already added to the clusters are removed from the seed tower list. The procedure repeats until all towers on the seed tower list are accounted for. A PEM energy cluster is formed by $3 \times 3$ towers in $\eta - \phi$ space.

### 4.1.2 Electron Energy Measurement

Once the cluster is identified, the energy of the electron is just the sum of $3 \times 3$ tower energies. However, before the tower energies are actually added, the following corrections need to be applied. The first correction is the so-called PEM tower mapping correction. It is designed to take out tower gain variations between towers. The tower gain variations (up to 10% between towers) are mostly due to variations

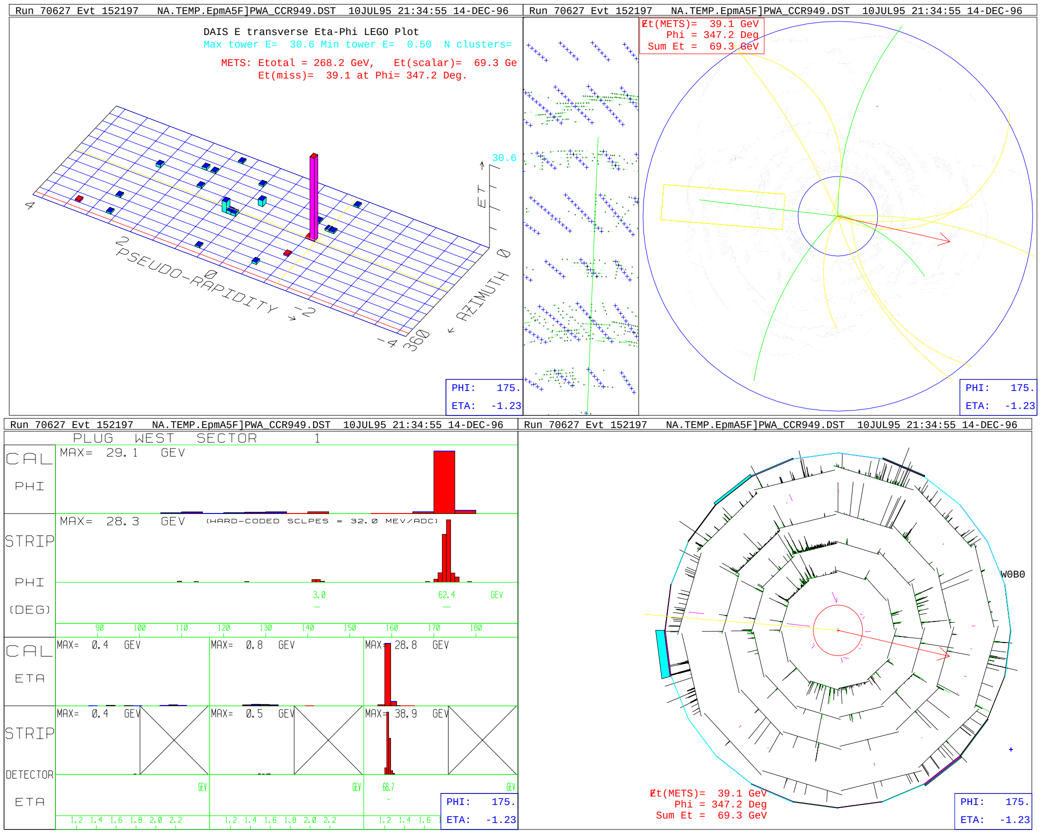

Figure 4.1: A typical plug $W$ candidate event with an isolated PEM energy cluster ($E_T$ = 32 GeV) at $\eta$ = 1.23. The direction of the missing transverse energy ($\not\!\!E_T$ = 39 GeV) is indicated by the arrow in the $r - \phi$ view. The strip cluster energy profiles are shown in the bottom left plot. For this particular event, an associated CTC track is expected and found, also a 4-hit SVX track pointing to the PEM cluster as shown in the two plots on the neighbouring side.

in the thickness of glue between the pad (copper plating clad on the G-10 panel) and the proportional tubes inside the PEM. The tower gain constants have been measured for each PEM module using an electron test beam [21] [22]. The second correction is the PEM's "dead layer" correction. Over the course of the PEM construction and during the Tevatron runs, a few PEM layers have been electrically disconnected because of high voltage (HV) problems. This results in a lower energy measurement in the PEM quadrants that have disconnected layers. Therefore it is necessary to correct for the effect of "dead layers" in the PEM quadrants based on the average longitudinal shower shape measured with test beams [23]. The non-linearity correction is applied to the measured energy to account for the PEM's non-linear response at high energy due to the limited longitudinal depth of the PEM. The last correction is for a quadrant-dependent energy scale. It arises from the fact that the PEM quadrants have independent gas gain controls and high voltage (HV) sources. Therefore, the quadrants can be different. The scale factors for the PEM quadrants are derived from a sample of Central-Plug $Z$'s which has one electron (or positron) in the CEM and one positron (or electron) in the PEM. The invariant mass distribution of a sample of Central-Plug $Z$'s is shown in Figure 4.2. The mean $Z$ mass ($M_Z = 90.84 \pm 0.08$ GeV) from a fit to the invariant mass distribution with a $Z \rightarrow ee$ Monte Carlo indicates that the overall PEM energy scale is within 1% of the known $Z$ mass value of 91.17 $GeV/c^2$.

The same central-plug $Z$ sample is also used to check the PEM energy scale as a function of time. As shown in Figure 4.3, the $Z$ mass is stable to within 1% over the course of the run. This is an independent check on the PEM gas gain system, which controls gas gain through a high-voltage feedback in response to temperature and pressure changes. The gas gain system is also equipped with $Fe^{55}$ source mounted inside proportional tubes which closely monitor the gas gain for each PEM quadrant. Data from the gas gain system show that there was a 2%

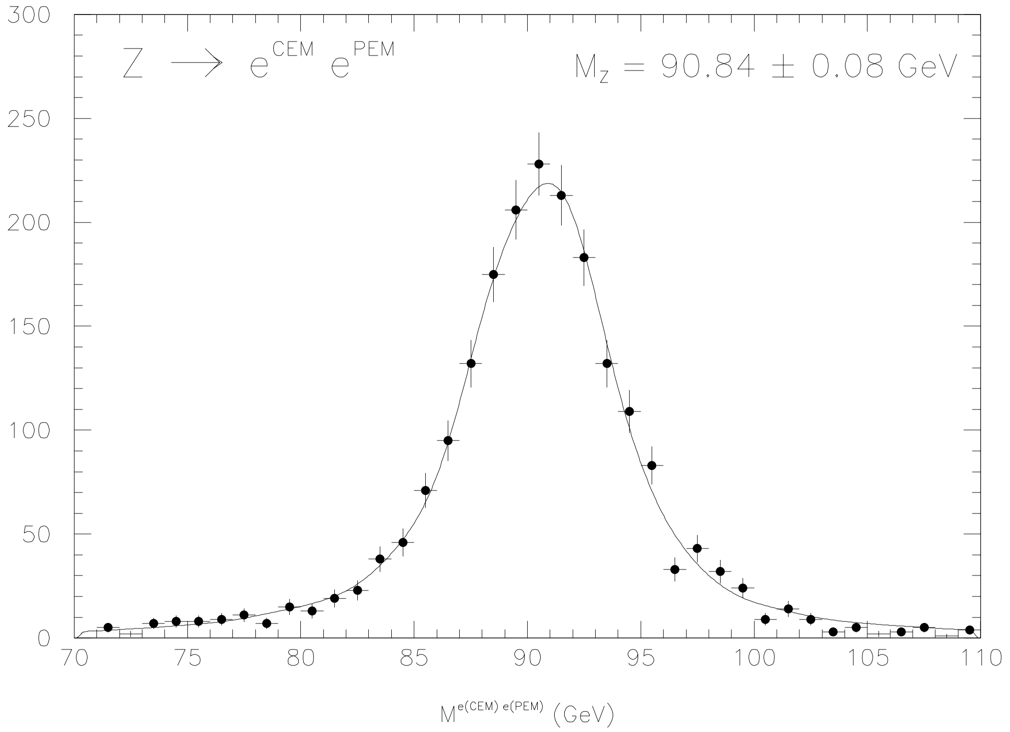

Figure 4.2: The invariant mass distribution measured from a sample of Central-Plug $Z$'s. The data are fit with $Z \rightarrow ee$ Monte Carlo which takes into account of radiative correction. The detector response is also included in the simulation.

drop in gain at the beginning of Run 1B compared with that of Run 1A, which remained stable to within 1% during the Run 1B data taking periods. This agrees with results of the $Z$ mass measurement from the Central-Plug $Z$ sample.

### 4.1.3 Plug Electron Position Measurement

The electron shower centroid position measurements are important for two reasons. The location of electrons in the PEM and at the primary interaction vertex

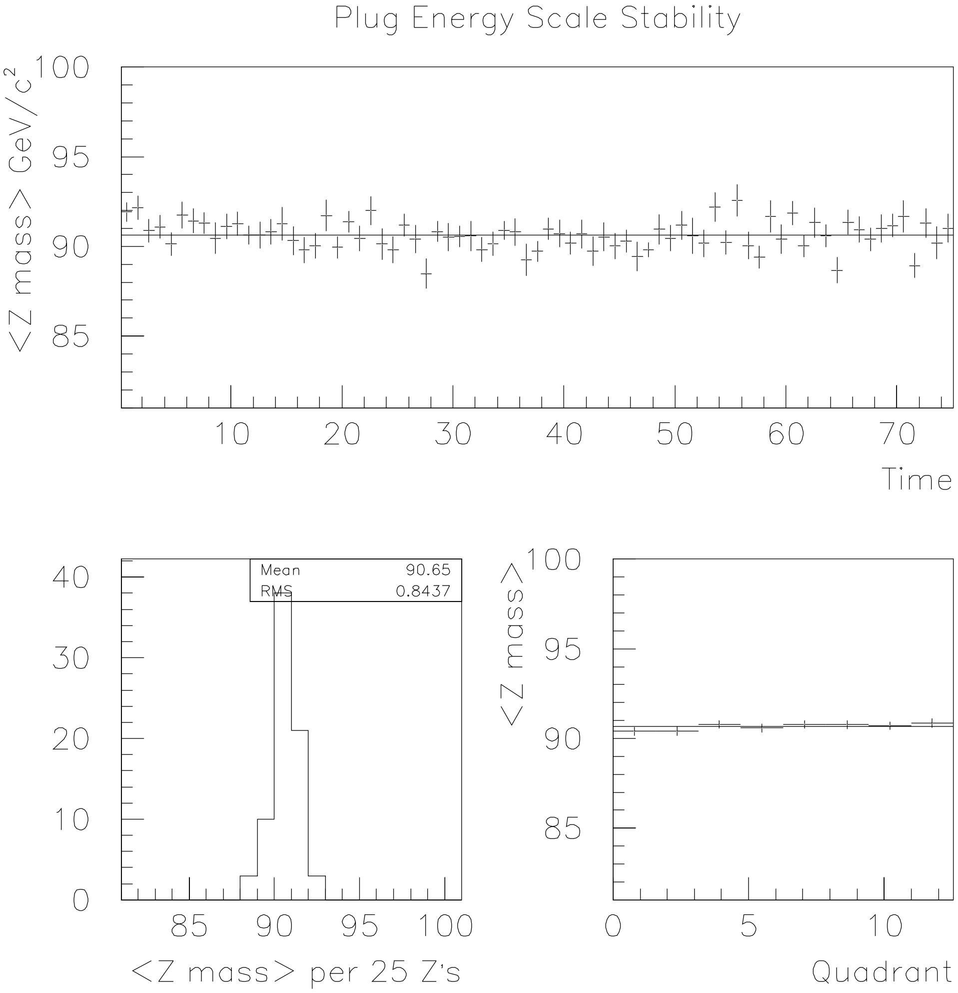

Figure 4.3: In the top plot, $Z$ mass measured from Central-Plug $Z$'s is flat as a function of time. Each data point is the average of 25 Central-Plug $Z$'s. The bottom left plot shows that variation of the average is within 1%. The quadrant dependence of energy scale (4 quadrants on each side) is removed by the energy corrections as indicated in the bottom right plot.

determine the direction of the plug electron momentum. The plug electron position information is crucial to identify charge of plug electrons in conjunction with the associated SVX tracks. In the latter case, the precise position measurement is essential to reduce charge misidentification of plug electrons or positrons.

The plug electron position in the PEM, or the shower centroid location, is determined from the PEM transverse tower energy profile as the location of the PEM towers are known. For electrons with the detector pseudo-rapidity $|\eta| < 1.8$, the plug electromagnetic strip detector measures the strip cluster energy profiles in both $\eta$ and $\phi$ thus providing electron position measurements as well.

### Electron Position Measurement Using PEM Tower Energies

There are a number of ways to extract shower centroid information from measured tower energies of an electromagnetic energy cluster. The method of energy weighted mean (also frequently called center-of-gravity method) is often used. The energy weighted mean position of shower $\vec{X_o}$ is defined as:

$$\vec{X_o} = \frac{\sum_{i=1}^{9} E_i \vec{X_i}}{\sum_{i=1}^{9} E_i} \qquad , \tag{4.1}$$

where $E_i$'s are the tower energies in the cluster and the $\vec{X_i}$'s are the center positions of the towers. The energy weighted mean is equal to the true shower centroid only when the transverse shower shape is uniform. The transverse EM shower, however, is sharply peaked at the centroid (see discussions about transverse shower shape later in this section). As a result, the shower centroid given by Equation 4.1 is biased towards the center of the tower that has the biggest energy deposit. A position resolution of the order of $\approx$ 5 mm can be achieved for a tower of $\approx$ 5 cm or so [24]. As discussed in [24], a correction to the energy weighted mean can be derived by assuming that the shower follows an exponential functional form. After this correction is applied, the positron resolution can be improved to of order of $\approx 2 - 3$ mm.

The optimal way to use the tower energies is to fit the measured tower energies with expected from a known shower profile. The electromagnetic (EM) showers are formed by cascade of secondary particles (secondary electrons and photons) produced in the Bremsstahlung and pair production processes when primary electrons or photons traverse dense calorimeter materials (e.g. Pb). The transverse shower shape, which is usually expressed as the differential energy fraction as a function of distance from the shower centroid, is mainly determined by the calorimeter construction (which depends on the amount and composition of calorimeter materials and the geometrical parameters). EM showers with energy bigger than 20 GeV have stable transverse shower shapes which are almost independent of the energy of the incident electron or photon. The amount of energy in the towers is just the integrated energy over the towers' physical dimensions and is only dependent on the location of the shower centroid when the shower profile and the tower dimensions are known. Therefore by comparing the measured tower energies and the expected ones and varying the shower location, the precise shower centroid position can be derived.

Because plug electrons land at the PEM at different angles thus traversing different amount of calorimeter materials, the plug electron shower shape is a function of pseudo-rapidity. Here we specifically look at position measurement for the plug electrons with $|\eta| > 1.8$ where there is no strip detector coverage. Inside this pseudo-rapidity region, the electron incident angle (with respect to the norm of calorimeter surface) varies only between $11^o - 18^o$. For simplicity, a single shower shape is used in the fit.

Although theorectical shower shape can be calculated with the EGS Monte Carlo and a detector simulation, the complexity of putting in all minute details, i.e. from shower development to collection of charge, indicates that it is better use a shower shape directly measured from real electron data. Since no deliberate efforts were made with test beam to measure the shower shape to the required precision for this analysis, it is determined from the plug $W$ electron data. Because the transverse shower shape of high energy electrons is stable, only a handful of events are needed for the shower shape tuning.

We start with an approximate functional form:

$$f(r) = \frac{1}{(r^2 + R_M^2)^\beta} \qquad , \tag{4.2}$$

where $f(r)$ is the differential energy fraction of the shower and $r$ is the distance in cm from the shower centroid. The $R_M$ and $\beta$ are shower shape parameters where $R_M = 1.7$ cm (close to the Moliere radius of electron showers in the PEM) and $\beta = 1.8$. The shower curve is shown in solid line in Figure 4.4.

We first describe how the fit is done. For the position measurement, we employ a $5 \times 5$ tower array in $\eta - \phi$ space instead of a $3 \times 3$ tower array in the energy measurement. This reduces correlation between the $\eta$ and $\phi$ directions, especially for high $|\eta|$ energy clusters where the tower size is smaller. For simplicity, we fit the $\eta$ and $\phi$ profiles separately. Taking the fit in $\phi$ direction as an example, energies from five towers with the same $\phi$ are summed to form $\phi$ energy blocks. We fit the shower position by minimizing the following $\chi^2$ function:

$$\chi^2 = \sum_{i=1}^{5} \frac{(E_i^{measured} - E_i^{expected})^2}{\sigma_i^2} \quad , \tag{4.3}$$

where $E_i$'s are measured or expected $\phi$ or $\eta$ block energies and $\sigma_i$ is the error on the measured energies. Note that $E_i^{expected}$ is calculated by integrating the shower shape over the actual tower areas. These are functions of both the location of the

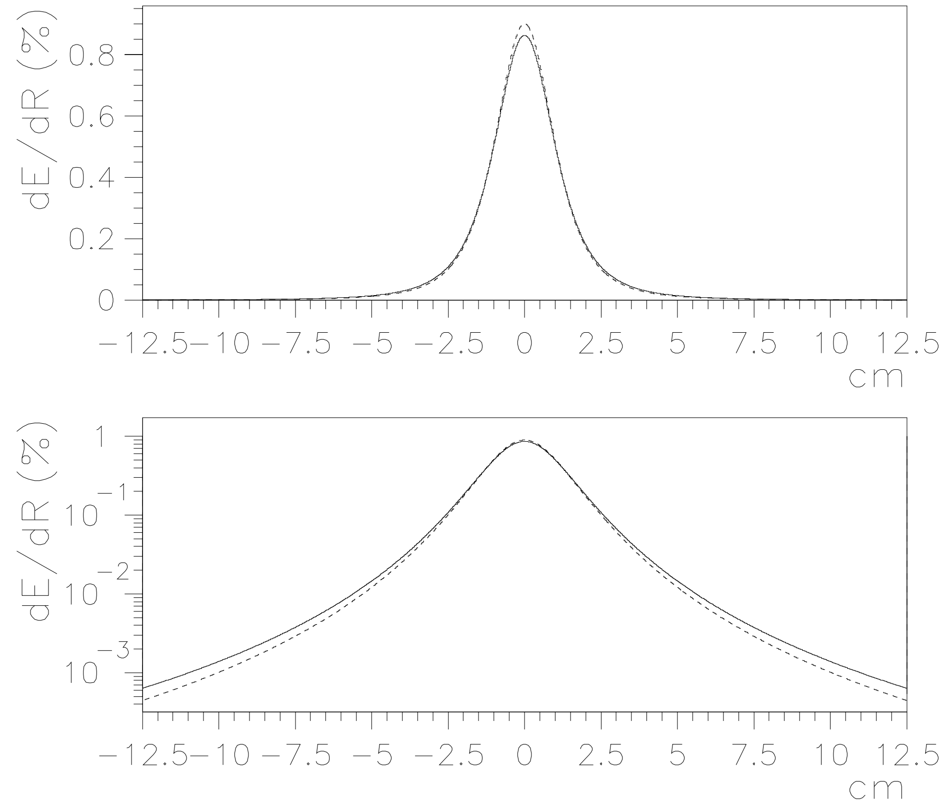

Figure 4.4: The comparison between shower profiles. The solid line is the profile defined in Equation 4.2 and the dashed line is the one tuned to data with pseudorapidity between 1.8 and 2.2. The plots are shown in log scale in the bottom plot.

shower centroid and the shower shape defined in Equation 4.1. The total sum of the expected 5 energies is normalized to the corresponding measured energy sum over the $5 \times 5$ towers. Here, $\sigma_i$ is the error on $E_i^{measured}$.

The shower shape is tuned in the following way. Starting with a shower shape, we fit the measured tower energies by minimizing $\chi^2$ as defined in Equation 4.3. We compare event by event the measured and expected block energies and adjust the shower shape accordingly. After several iterations, we reach the tuned shower shape in Figure 4.4.

Note that the energy block with the biggest energy is most sensitive to imprecision of the shower shape. The position information comes from imbalance of energies on two sides of the center block rather than the center block energy. Therefore, in the actual shower fit, we remove it from the $\chi^2$ calculation in Equation 4.3 to further reduce the sensitivity to the shower shape. As will be shown later in the later sections of this chapter, this procedure yields the position resolution of $\approx$ 1 mm for an average tower size of $5 \times 5$ $cm^2$.

There are many factors which may affect the position measurement of EM showers. In practice, the total expected shower energy is normalized to the measured total. This removes to first order the sampling energy fluctuations. The electronics noise for the PEM for a typical $3 \times 3$ cluster is around 0.2-0.3 GeV. However it is mostly coherent and is removed by the normalization thus its effect on the energy balancing (which determines the position of EM showers) is small. The variation in individual tower gain is mainly a function of time rather than across towers (the mapping correction takes out tower variation to better than 0.2%) and thus it is also taken out by the normalization. A 1 mm position shift in the shower centroid in the transverse plane causes a relatively stable shift in energy deposition between two neighbouring towers in opposite direction by the amount of $\approx 0.2GeV$. The current PEM energy measurement has energy sensitivity on this order.

### Electron Position Measurement Using the PEM Strips

The PEM strip detector is available in the pseudo-rapidity region between $1.2 < |\eta| < 1.8$. It is divided into two parts, strips in $\phi$ and $\eta$ directions. The clustering of strips is similar to that of towers. After a PEM energy cluster is found, we look for strips with energy above some energy threshold in the vicinity. These strips are ordered according to their energy deposits. The 11-strip energy cluster is formed with the biggest energy strip at the center. Using the similar procedure, we fit the strip energy profile with that calculated from the shower shape. Again, as is shown later the average position resolution is of $\approx$ 1.7 mm for strip width of 1.7 cm. Although the strips are 5 times finer in segmentation, the position resolution is not as good as that with pads (towers). This is because the strips sample only a part of the shower thus the shower profile is sensitive to the longitudinal fluctuations in EM showers.

## 4.2 SVX Standalone Tracking

The SVX is a precision tracking device that measures track position of charged particle to better than $\approx$ 10 $\mu m$. One benefit of the SVX is its very fine double track resolution ($\approx$ 200 $\mu m$) compared with that of the CTC ($\approx$ 5 mm). This is extremely useful in a high luminosity environment where the CTC suffers from a high density of soft tracks curling along the $Z$ axis. Furthermore, the SVX covers a pseudo-rapidity region up to $|\eta| = 2.3$. In contrast, the CTC only covers a pseudorapidity range up to $|\eta| = 1.8$ and has a steeply falling track finding efficiency at large $|\eta|$. This makes the SVX attractive for the high $|\eta|$ electron tracking.

The standard SVX tracking at CDF starts with a CTC track and searches for SVX hits by extrapolating the CTC track into the SVX geometrical region. Here we describe a track finding procedure for electrons (or positrons) using only SVX hits. We are interested in finding a SVX track for electrons. The SVX Standalone Tracker starts by collecting all SVX hits inside a 0.1 radian $\phi$ cone centered on the EM shower centroid. It then takes the beam position in the $r - \phi$ plane and calculates the $\phi$ for each hit. The track searching begins with outer layer hits. For each hit in layers 1, 2, and 3 (layer 0 is the inner most SVX layer), a 300 $\mu m$ wide road along the hit and the vertex is formed in the other layers and the closest hit in each layer to the prediction within this road is selected. This defines a candidate track. The candidate track is then fitted with a straight-line. The straight line is a good approximation to circle, as the sagitta of a high $Pt$ ($> 10GeV$) track is on the order of a few microns within the $\sim$ 5 cm radial span of the SVX layers. If there is a hit with a residual bigger than 50 $\mu m$ (the position resolution of SVX device is $\approx$ $10\mu m$), it is removed and a new line fit is done with the rest of the hits. The impact parameter, which is defined as the distance from beam position to the fitted line is required to be less than 150 $\mu m$ for 3 and 4 hit SVX tracks and 100 $\mu m$ for 2 hit tracks. Tracks sharing at least one SVX hit are merged according to fit $\chi^2$ because it is unlikely that a SVX hit is shared between two real SVX stubs.

In Figure 4.5, the SVX track residual distributions as measured from a sample of plug $W$'s are shown. The individual hit position resolution of $\approx$ $10\mu m$ is consistent with the expected SVX position resolution. Figure 4.6 shows the impact parameter distribution. The spread with a standard deviation of $\approx$ $50\mu m$ is a combination of uncertainty in beam $X - Y$ position of $\approx$ $40 - 50\mu m$ plus SVX track impact parameter resolution estimated to be $\approx$ $10\mu m$. Figure 4.6 indicates a small background for three and four hit SVX stubs. Figure 4.7 shows

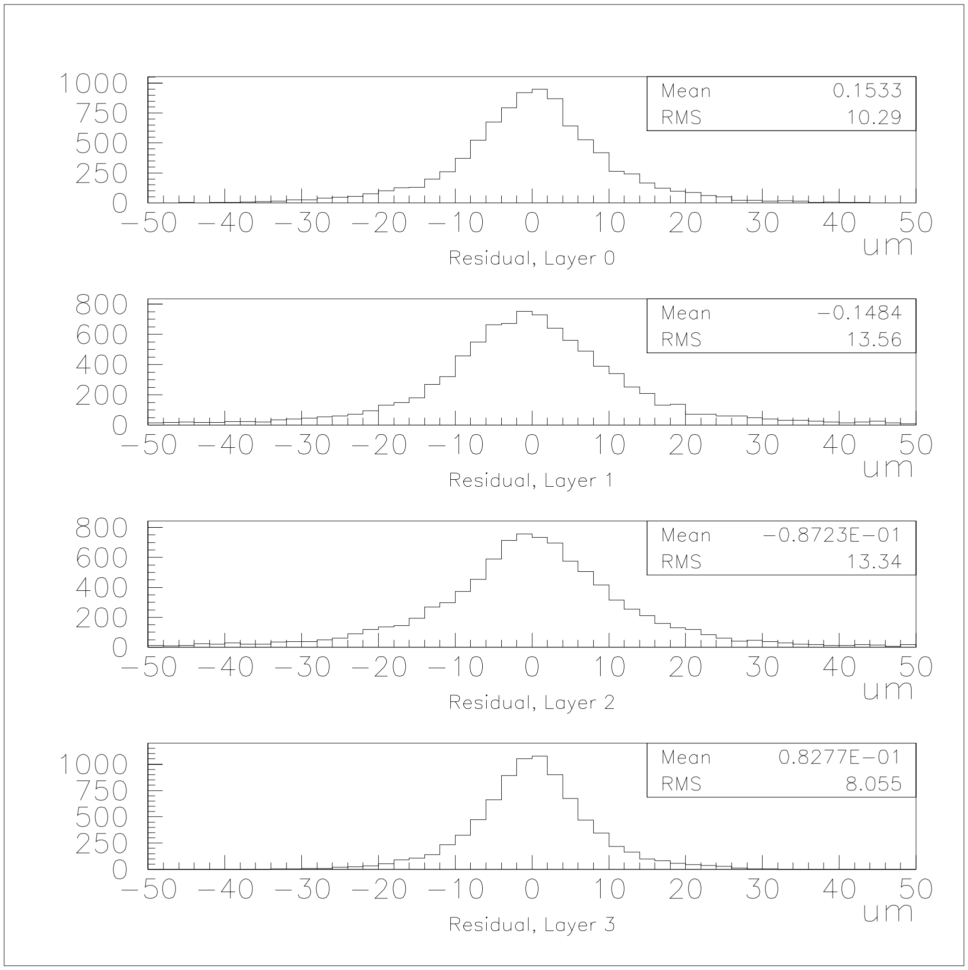

Figure 4.5: The residual distributions of different SVX layers using SVX tracks in the plug $W$ electron sample. The magnitude of the residuals is as expected from the SVX intrinsic spacial resolution of 10 $\mu m$.

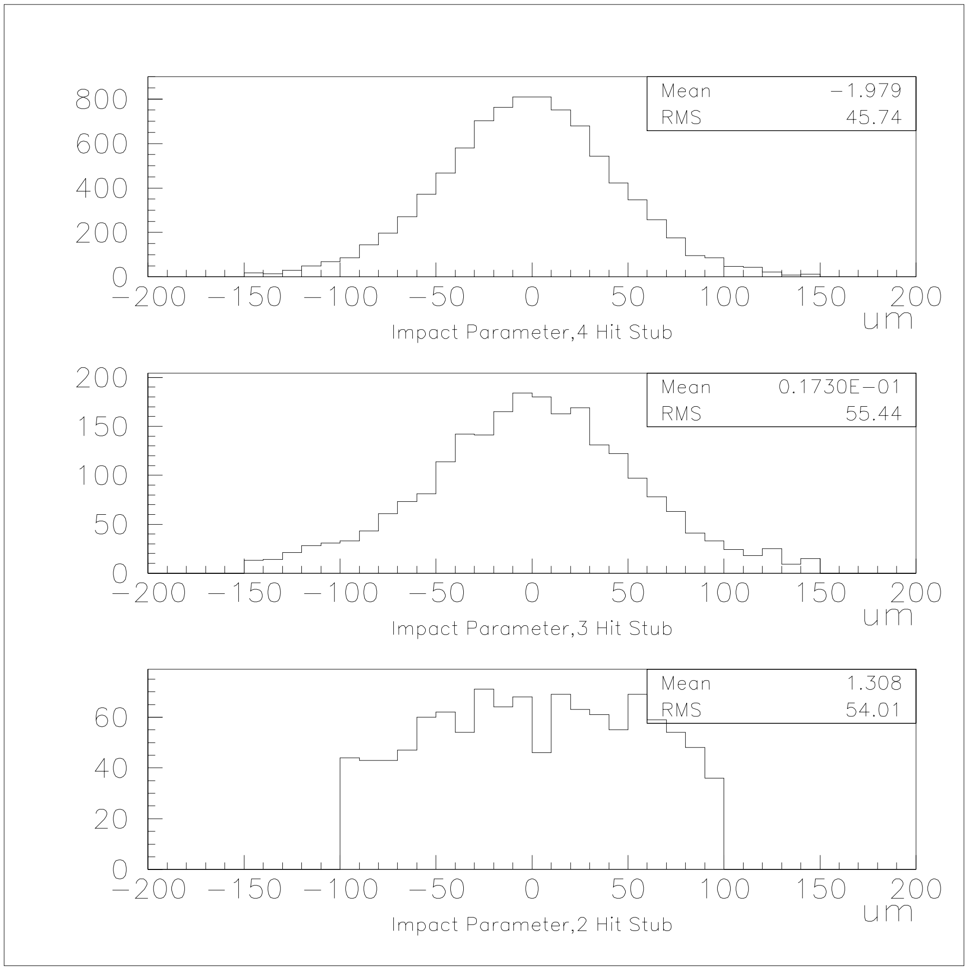

Figure 4.6: The impact parameter distributions for found 4, 3, and 2 hit SVX tracks in the plug $W$ electron sample. The existence of background in the 2 hit SVX track is expected.

the track finding efficiencies for tracks in the plug region ($|\eta| > 1.1$). These are determined from a sample of Central-Plug $Z$'s. The track finding efficiency is defined as the fraction of plug electrons that have an associated track found by the tracking algorithm (either SVX tracking or CTC tracking). The CTC track finding efficiency diminishes quickly as a function of $|\eta|$ and becomes zero at $|\eta| = 1.8$ while the SVX stub finding efficiency is relatively flat up to $|\eta| = 2.3$. The $\approx 60\%$ SVX tracking efficiency is expected from the limited SVX coverage in $Z$.

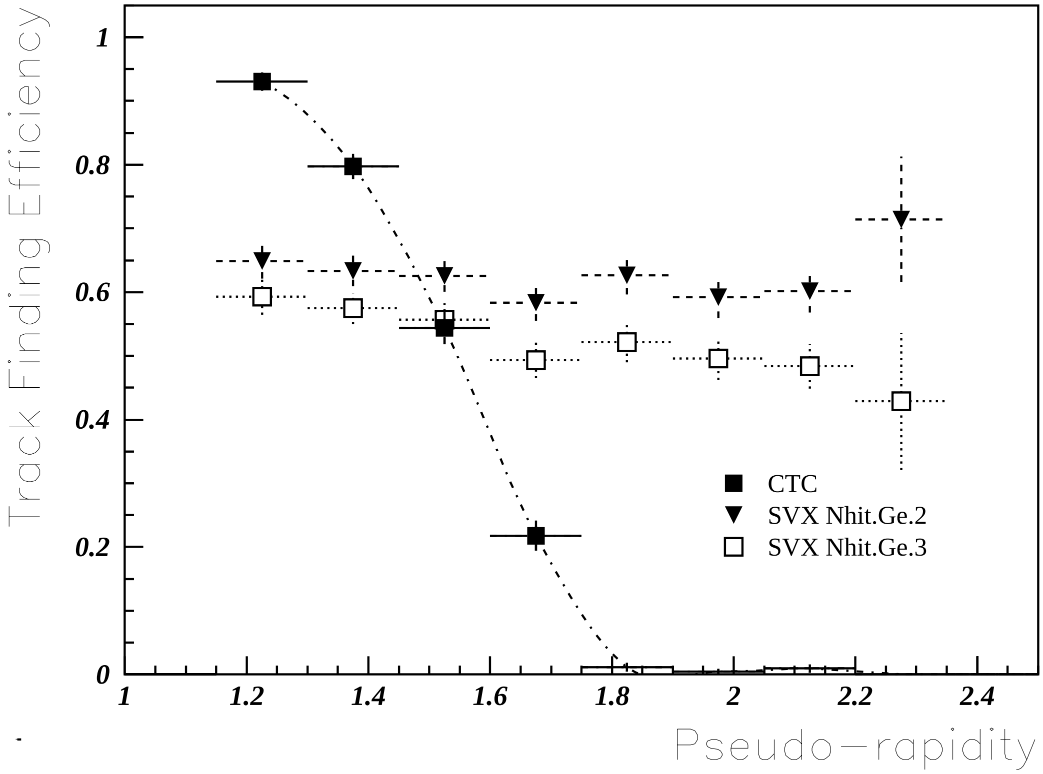

Figure 4.7: The track finding efficiencies for SVX and CTC as measured from a sample of Central-Plug $Z$'s. The CTC track finding efficiency falls quickly as a function of pseudo-rapidity, while the SVX track finding efficiency stays relatively flat over the entire $|\eta|$ region.

The SVX track is matched to the EM cluster in the $r - \phi$ plane, because the

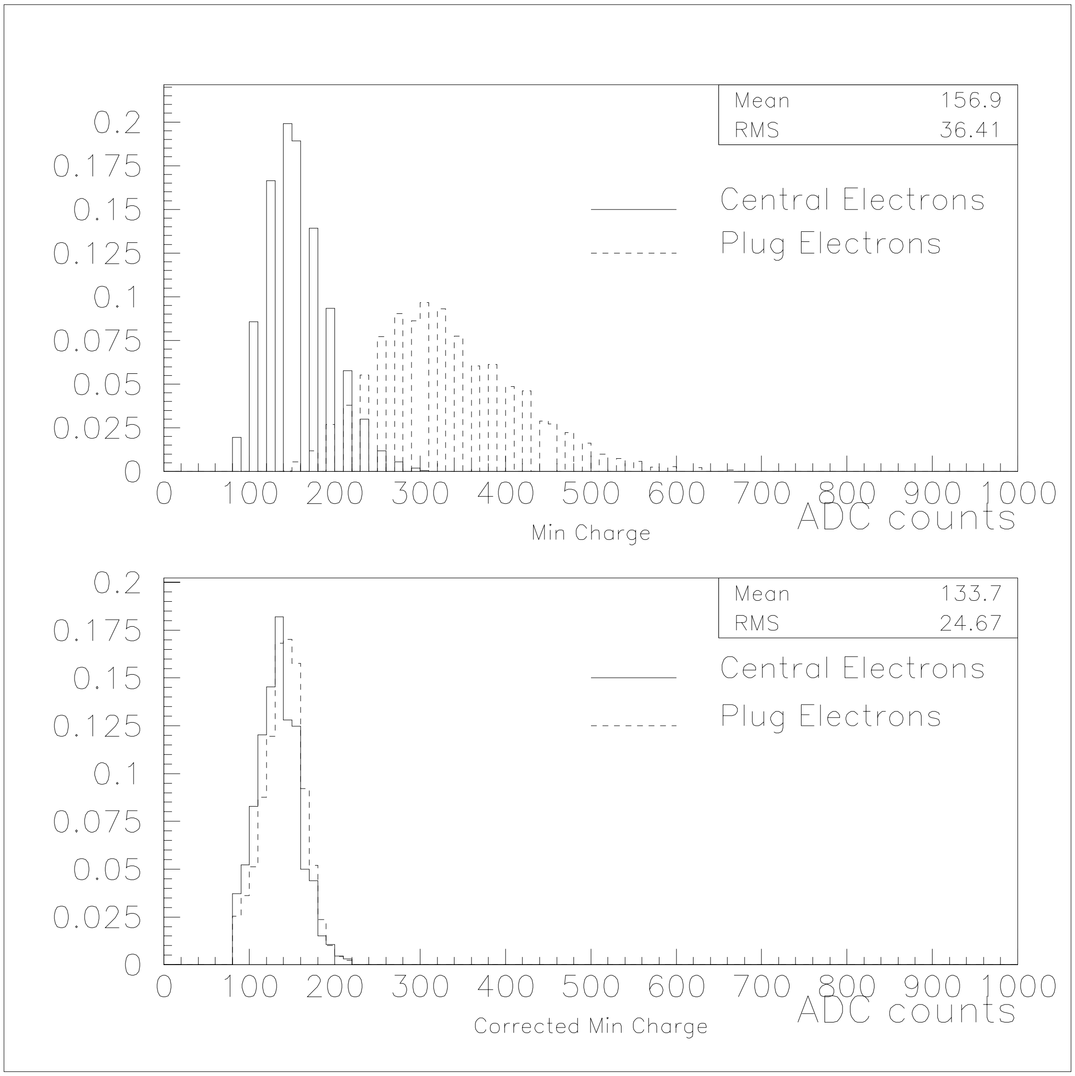

Figure 4.8: The top plot shows the distribution of the minimum ionizing charge deposition of the SVX track as measured from samples of central and plug $W$ electrons. The bottom plot shows the distributions after a correction for track length in the SVX layer. All plots are normalized to the same area. The separation of low and high $|\eta|$ SVX stubs is clearly seen in the uncorrected charge distributions. The corrected charge is required to be between 80 and 220. This reduces the mis-associated SVX tracks that are inconsistent with the electron $\eta$.

SVX detector does not provide $Z$ information. The tracks that cross SVX layers at different angles (traversing different amount of material) deposit different amount of energy through ionization. This fact can be used to determine the $|\eta|$ range of SVX tracks thus making matching of the SVX track and the EM cluster in the $\eta$ direction possible. This reduces the chance of mis-association of the SVX track and the EM cluster. The charge deposition after a correction for track length in the SVX layers is required to be within 80 and 220 ADC counts (which is the expected average charge deposit for a normal incident track). Figure 4.8 displays the charge deposition distributions of SVX tracks measured in the $W$ electron samples. This is an effective way to remove the events that have a SVX track found but is inconsistent with originating from the $\eta$ range of the EM cluster.

## 4.3 Charge Determination

The charge determination is an important part of this analysis. We begin by discussing the charge determination using the SVX-PEM $\delta\phi$ method. It is followed by a discussion of charge determination using CTC tracks. Cross checks between the two methods are made in the overlapping plug $W$ electron samples and are described in the end of the section.

### Charge Determination Using SVX-PEM $\delta\phi$ Method:

In the previous section, a SVX track finder that is efficient in finding an SVX track for plug electrons has been described. At CDF, positively (negatively) charged particles travel in increasing (decreasing) $\phi$ inside the solenoidal magnetic field. This fact can be used to determine the charge for electrons and positrons that have an associated SVX track. The SVX track measures the precise initial track direction (near the vertex point) in $\phi$ while the EM shower centroid measurement combined with the location of the vertex position gives another measurement of track $\phi$. The difference of the two $\phi$ measurements determines the charge of the electron (or positron). The SVX track measures a track $\phi$ to an accuracy of $\approx 0.3$ mrad. When extrapolated to the shower maximum position of the PEM, this corresponds to between $0.2 - 0.4$ mm depending on the pseudo-rapidity. As discussed in the previous section, The shower centroid is measured with strip position detector placed at shower maximum in the pseudo-rapidity region between $1.2 - 1.8$. In the pseudo-rapidity region between $1.8 - 2.4$, where there is no strip detector at the shower maximum location, the centroid is measured from the calorimeter towers. We use the ratio of $\delta\phi_{measured}/\delta\phi_{expected}$ where $\delta\phi_{measured} = \phi_{PEM} - \phi_{SVX}$, and $\delta\phi_{expected}$ is calculated from the calorimeter energy and the radial location of the electron. Since $\delta\phi$ is inversely proportional to the transverse momentum of the track, $\delta\phi_{measured}/\delta\phi_{expected}$ is just the ratio of $E/P$. This ratio is expected to peak at +1 and -1 for positrons and electrons, respectively.

Figures 4.3 and 4.3 show the $\delta\phi_{measured}/|\delta\phi_{expted}|$ distributions. The peaks corresponding to positrons and electrons respectively are clearly seen. The width of peaks in Figures 4.3 and 4.3 is from the $\delta\phi_{measured}$ resolution and is mainly due to the position resolution of the PEM. Because the average $\delta\phi$ of high $|\eta|$ tracks ($1.8 < |\eta| < 2.4$) is about $\frac{1}{3}$ of that of low $|\eta|$ tracks ($1.2 < |\eta| < 1.8$), the resolution of $\delta\phi_{measured}/|\delta\phi_{expected}|$ is worse for high $|\eta|$ tracks though the PEM's position resolution is better. The position resolutions of the PEM can be derived from the widths of peaks in Figures 4.3 and 4.3 and the expected bending. The average position resolution for plug electrons is 1.7 and 1.0 mm measured with PEM strips and towers respectively. The position resolution measured with tower energies is better although strips are segmented five times finer. Strips only sample a part of the EM shower. Therefore, its position measurement is prone to shower fluctuations. This clearly shows that fine segmentation is not important for a single

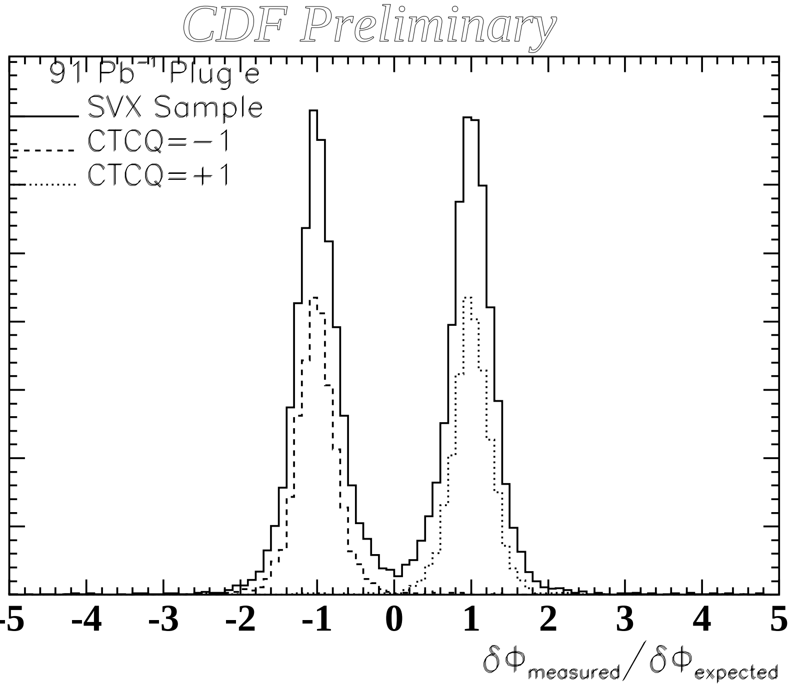

Figure 4.9: The distribution of $\delta\phi_{measured}/|\delta\phi_{expted}|$ from the plug $W$ electron sample with $|\eta| < 1.8$. The $\phi_{PEM}$ is corrected for PEM mis-alignment. The two peaks corresponding to electrons and positrons are clearly seen.

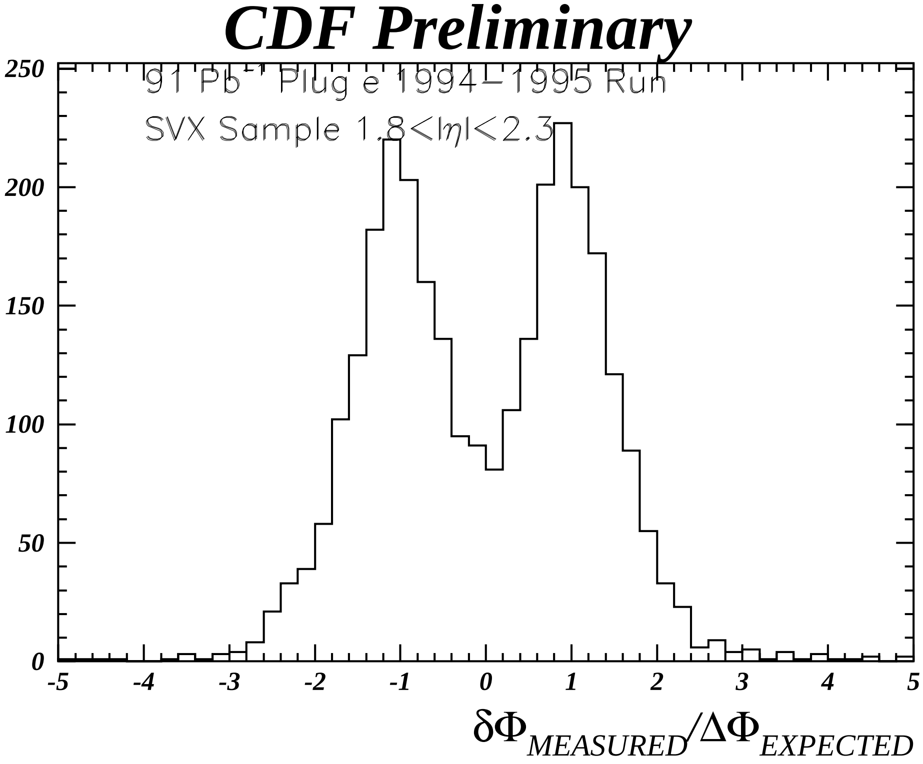

Figure 4.10: The distribution of $\delta\phi_{measured}/|\delta\phi_{expected}|$ from the plug $W$ electron sample with $|\eta| > 1.8$. The $\phi_{PEM}$ is corrected for PEM mis-alignment. The two peaks corresponding to electrons and positrons respectively are clearly seen.

shower position measurement.

Note that the $\phi_{PEM}$ in Figures 4.3 and 4.3 is already corrected for the PEM's mis-alignment relative to the SVX. Although the internal alignment of pads and strips in each quadrant is controlled to within 0.1 mm, the positioning of the EM calorimeters usually have on the order of $\approx 1$ cm mechanical allowance in $r - \phi$ plane. Each time the EM calorimeter is pulled out for shutdown maintenance and put back in, it ends up in a different $r - \phi$ position. Therefore, in situ position alignment calibration is necessary in order for this technique to work. The PEM position in $r - \phi$ plane can be described by three parameters: off-centerness in $\delta$x and $\delta$y directions and a rotation $\delta\phi_o$. The actual $\phi_{cor}$ and local $\phi$ are related in the following formula:

$$\phi_{cor} = \phi - \frac{\delta\ x}{R} sin\phi - \frac{\delta\ y}{R} cos\phi - \delta\phi_o, \tag{4.4}$$

This technique is self-calibrating in that for each local $\phi$ bin $\phi_{cor}$ corresponds to center position of two peaks (e.g. Figure 4.3 and 4.3) and is easily determined. A sample of electrons and positrons are employed for the calibration. Figure 4.11 shows $(\phi_{cor} - \phi)$ as a function of $\phi$ for the west and east PEM separately. The dashed lines are fits to the data. The sine wave displayed in the alignment correction constants clearly indicates that both the west and east PEM are located off-center. The magnitude and direction of the off-center locations can be determined by the amplitudes and phases of the sine function fit to the alignment constants. After some analysis, we find that the West PEM is off-center by -1.3 mm and 4.8 mm in the X and Y directions, respectively. The East PEM is off by 2.8 mm and 0.9 mm in the X and Y directions, respectively. It should be noted that the magnitude of the PEM off-center locations is within the mechanical allowance. Each time the PEM is opened and closed, the alignment is expected to

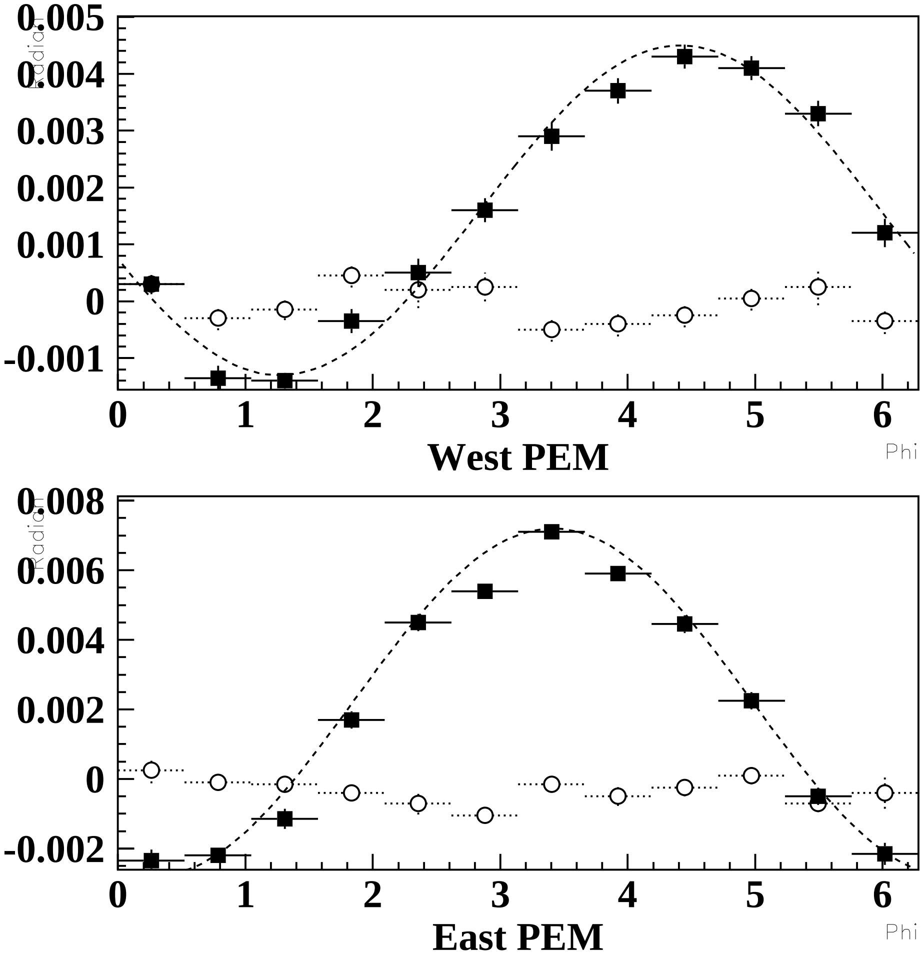

Figure 4.11: The PEM alignment constants as determined by centering the two peaks for each 30$^o$ section at 0. The sine wave of the alignment constants shows that both PEM modules are off-center. The final correction includes an overall off-center correction and additional 24 30$^o$ section corrections which are plotted here in circles.

be different. Fortunately, there was only one opening of the PEM in the very early stage of Run 1B. Therefore, only one set of alignment calibration constants are needed for Run 1B. The final PEM $\phi$ correction includes an overall off-centerness correction plus 24 alignment correction constants, one for each $30^o$ PES section. Using this alignment technique, the position of calorimeters is known to better than 0.5 mm.

The SVX track and the EM cluster can be mis-associated when the incorrect track is taken for the EM cluster. The chance of a mis-identified SVX track (except in 2-hit case) is extremely small because of the precise position resolution of SVX and the above SVX track requirements. When a mis-association happens, in most cases, the right SVX track is actually not expected to be there. There are two possibilities: (1) the primary $Z$ vertex is wrongly associated with the electron, which is actually not in the SVX fiducial region; (2) the EM cluster is not an electron (background events). In both cases, such events are responsible for the events at the tails of the $\delta\phi_{measured}/\delta\phi_{expected}$ plots. Figure 4.12 shows the distribution of the $\phi_{PEM} - \phi_{expected}$ ($\phi_{expected} = \phi_{SVX} + Q * \delta\phi_{expected}$ and Q is sign of the charge) measured from a sample of plug $W$ events. The events with mis-association are flatly distributed while the associated events are sharply peaked at 0. The fraction of mis-associated events in the plug $W$ electron sample is estimated to be $(0.7 \pm 0.1)\%$.

The rate of charge mis-identification affects the asymmetry measurement. The peaks in the $\delta\phi_{measured}/|\delta\phi_{expted}|$ distributions are expected to be symmetric. This fact can be used to derive the charge mis-identification rate. It is determined by counting the events at the tails and extrapolating to the overlapping region. After subtracting the flat background expected from mis-association of SVX tracks, the charge mis-identification fraction is determined to be $0.8 \pm 0.2\%$ for plug electrons with $|\eta| < 1.8$ and $5 \pm 1\%$ for $|\eta| > 1.8$, respectively.

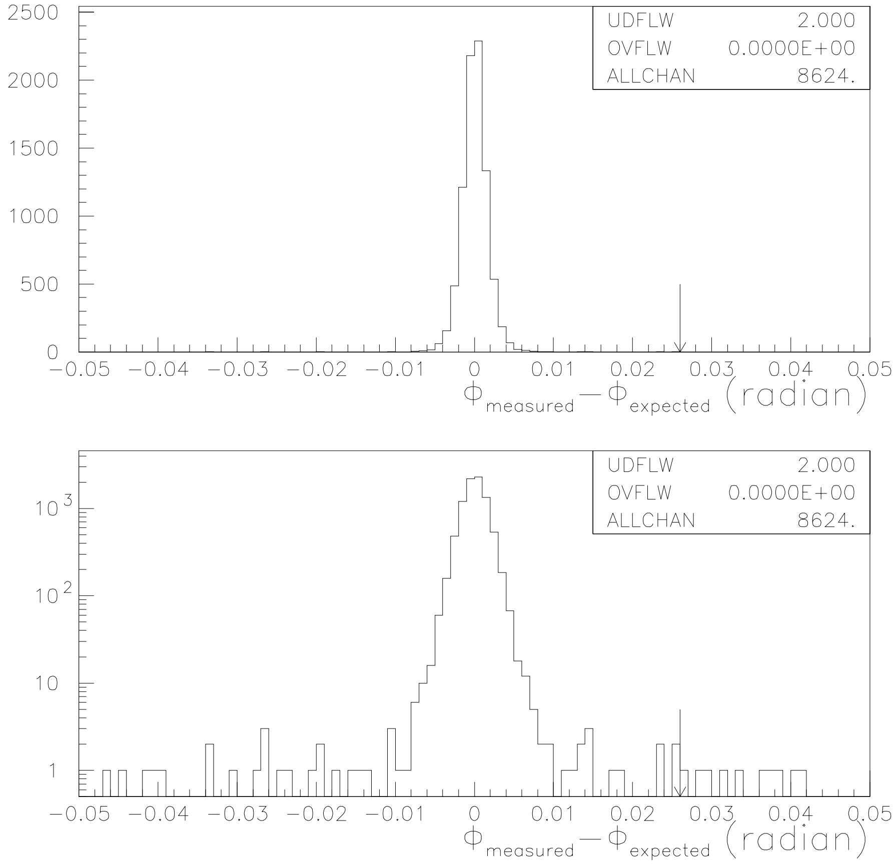

Figure 4.12: The distribution of $\phi_{PEM} - \phi_{expected}$ for a sample of plug $W$ events. The same plot is shown in log scale in the bottom plot. The fraction of mis-associated events is estimated to be $(0.7 \pm 0.1)\%$.

### Charge Determination Using CTC Tracks:

The charge of plug electrons or positrons can be determined from the direction of CTC track curvature. In this analysis, we determine the charge of a CTC track using only the beam constrained track parameters. We estimate the charge misidentification rate for this method from the central-plug $Z$ sample. We apply the $W$ CTC sample cuts (discussed in the $W$ event selection section) to the plug leg and further require that the invariant mass of electron pairs be between 81 and 101 GeV. Out of 783 central-plug $Z$ events passing the cuts, 13 are same sign events. Therefore, the charge misidentification rate is estimated to be $1.7 \pm 0.5\%$ . If we only require a beam constrained CTC track and drop the $W$ CTC sample cuts, we get 41 same sign events out of 887 central-plug $Z's$ . The charge mis-identification rate increases and becomes $4.6 \pm 0.7\%$ .

Because of the presence of multiple interactions along $Z$, an incorrect primary $Z$ vertex for the plug electrons can be chosen. From the central-plug $Z$ sample, we estimate that 2% of time the wrong primary vertex is assigned. In order to estimate this effect on the charge determination, we constrain the plug $W$ electron tracks manually to all primary vertices in each event. We find that less than 1% of tracks have their charge flipped from constraining to a different $Z$ vertex. Therefore, this has a negligible effect on charge determination.

### Comparison Between the Two Charge Determination methods:

For the plug electrons that have both CTC and associated SVX tracks, the charge can be determined in two ways. The dotted and dashed histograms in Figure 4.3 correspond to +1 and -1 charge as determined by the CTC track. The agreement between the two methods is good. Using this sample, the charge misidentification rate of the CTC method can be determined separately for positrons and electrons.

AFTER the application of the $W$ CTC sample cuts, the charge misidentification rate is estimated to be $0.50 \pm 0.2\%$ and $0.2 \pm 0.1\%$, respectively, for plus and minus charges. Taking the average of the two measurements, we get $0.40 \pm 0.2\%$. This is consistent with what we get using the Central-Plug $Z$ sample (with the CTC cuts). From the same sample but without the CTC cuts, the rates are higher as expected ($5.2 \pm 0.4\%$ and $3.5 \pm 0.3\%$ for plus and minus charges, respectively). Taking the average of two, we get $4.4 \pm 0.4\%$ which is consistent with $4.6 \pm 0.7\%$ measured from central-plug $Z$ sample. Note that this high charge mis-identification is BEFORE the application of the track quality cuts. Figure 4.13 is similar to Figure 4.3. The small peaks in the dotted and dashed histograms correspond to the events for which the charge as determined by the CTC track is mis-identified.

## 4.4 Plug $W$ Data Sample

### Plug Electron Triggers

A description of the triggers is given in Chapter 1. The plug electron triggers require energy deposition in $2 \times 3$ ($\Delta\eta \times \Delta\phi = 0.2 \times 15^{\circ}$) trigger towers. At level 1, the trigger tower energy is required to be at least 11 GeV. At level 2, two plug electron triggers are employed; one is an inclusive plug electron trigger which requires a transverse cluster energy $E_T > 20$ GeV; the other is a $W$ electron trigger which requires missing transverse energy $\not\!\!E_T > 15$ GeV in addition to the cluster transverse energy $E_T > 15$ GeV. Both triggers make use of a so-called "spike-killer" algorithm which requires energy sum depositions in both even and odd numbered PEM layers in a quadrant to be greater than some preset threshold (typically 3 Gev). It effectively controls high rate false triggers due to neutrons that deposited all their energy in one single PEM layer. The second trigger is more

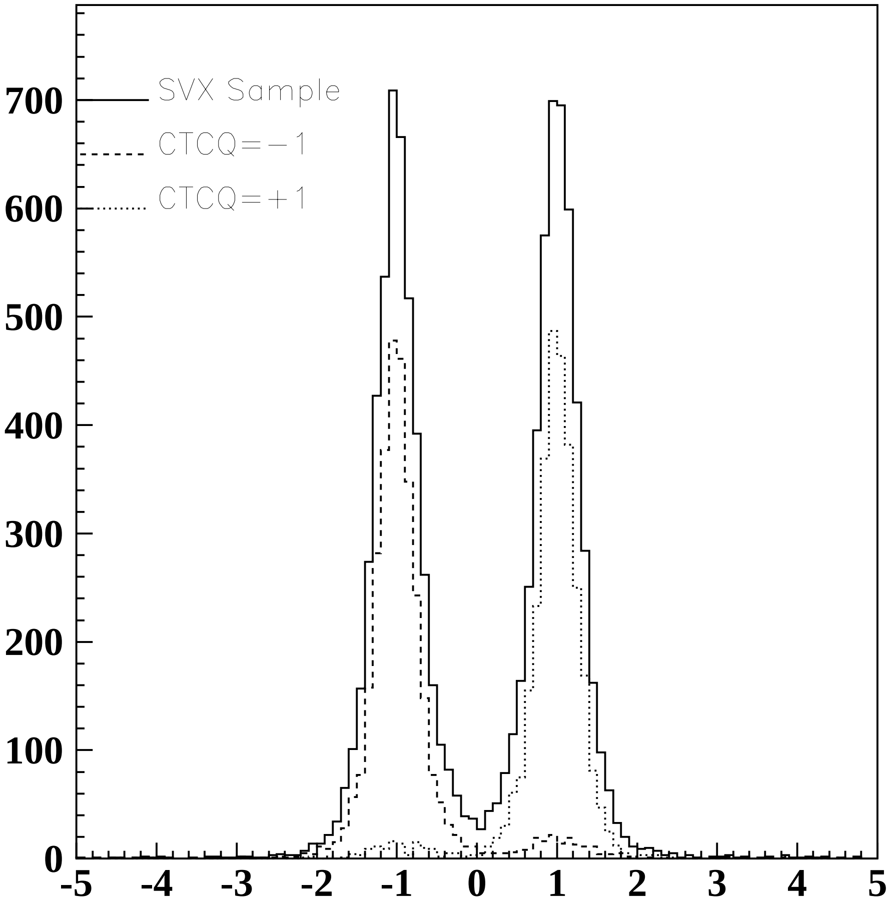

Figure 4.13: The distribution of $\delta\phi_{measured}/|\delta\phi_{expted}|$ for the plug $W$ electron sample. The $W$ CTC sample cuts have not yet been applied to the events with a CTC track. Without the track quality cuts, the CTC charge mis-identification rate is $5.2 \pm 0.4\%$ and $3.5 \pm 0.3\%$ for plus and minus charges, respectively. This is to be compared with the $4.6 \pm 0.7\%$ obtained using the central-plug $Z$ sample. After the applcaiton of the $W$ CTC sample cuts, the charge mis-identification rate is $(0.4 \pm 0.2)\%$.

efficient for plug $W$ electrons. However, because of its high rate at high luminosities in Run 1B, it was prescaled most of the time. The first plug electron trigger was only prescaled in the end of the Run 1B and at very high luminosities ($<5\%$ of total integrated luminosities). At level 3, there are two plug electron triggers with essentially the same requirements as in Level 2. but using a calculation and more accurate information available in Level 3. In Run 1B, the events passing the plug electron triggers are written onto datasets.

### PLug Electron Datasets

Two plug electron datasets are used for the Run 1B part of the analysis. The Stream A plug $W$ dataset include events passing Level 3 trigger "PEM_20_MET_20" which requires $E_T > 20$ GeV and $\not{E}_T > 20$ GeV. Unfortunately, an additional requirement $|\eta| < 1.8$ was present in Stream A. Therefore, the Stream B inclusive plug electron dataset is used for the analysis of the plug electrons with the pseudorapidity between $1.8 < |\eta| < 2.4$.

## 4.5 Plug $W$ Event Selection

The following requirements are applied to the above two datasets to select plug $W$ samples (the plug $W$ sample cuts). The $E_T$,$\not{E}_T$,$E_T^{jet}$,$E_{Had}/E_{EM}$,$Isolation$, $P_T^{high}$, and $|Z_0|$ have been explained in Chapter 3 and are listed without explanation.

$\boldsymbol{E_T > 25}$ **GeV**

$\boldsymbol{\not{E}_T > 25}$ **GeV**

$\boldsymbol{E_T^{jet} < 20}$ **GeV**

$\boldsymbol{E_{Had}/E_{EM} < 0.05}$

$\boldsymbol{Isolation} < \mathbf{0.1}$

$\boldsymbol{P_T^{high}} < \mathbf{10\ GeV}$

$|\boldsymbol{Z_0}| < \mathbf{60\ cm}$

$\boldsymbol{\chi^2_{PEM}} < \mathbf{3.0}$ The $\chi^2$ of 3x3 profile of the EM shower is defined as,

$$\chi^2_{PEM} = 1/9\left(\sum_i^{3\times 3}\left(\frac{E_i^{meas} - E_i^{pred}}{\Delta E_i^{meas}}\right)\right),$$

where $E_i^{pred}$ is the expected energy in a tower based on the transverse shower profiles measured at the testbeam.

$\boldsymbol{VTX_{occ}} > \mathbf{0.5}$ The VTX occupancy is the ratio of expected to found hits on the wires of the vertex detector along the "road" between the calorimeter cluster and the event vertex. This requirement ensures the correct vertex is selected for the plug electron.

In addition, the electron candidate is required to be in the fiducial region of the calorimeter, which is defined as $|\eta_{det}| > 1.2$ and the cluster centroid, as determined by the PES, is greater than 5 cm from the nearest 90° crack (the PEM quadrant boundaries). These requirements result in one plug electron sample from the Stream A dataset ($|\eta| < 1.8$), and one plug electron sample from the Stream B ($1.8 < |\eta| < 2.4$) dataset. We call the plug electron events in the Stream B sample the "High $\eta$ SVX" sample because the electron charge can only be determined by the SVX method. The plug electron events in the Stream A sample which also have an associated SVX track for the electron are called the "Low $\eta$ SVX" sample. The plug electron events in the Stream A which do not have an associated SVX track for the electron but have an associated CTC track are called the "Low $\eta$

CTC" sample. The following additional cuts are further applied to each of the samples.

The additional "Low $\eta$ SVX" sample requirements are:

**A 3 or 4 hit SVX Track**

**A PES $\phi$ Strip Cluster**

**$E_{max} > 5$ GeV** $E_{max}$ is the energy deposition in the center strip of the 11-strip cluster. This reduces the background from strip clusters which are not associated with the plug electron cluster.

**$\chi^2_\phi < 7.5$** The $\phi$ strip cluster energy profile is consistent with that of an electron. The $\chi^2_\phi$ is defined as:

$$\chi^2_\phi = \left( \sum_{i=1}^{11} \left( \frac{E_i^{meas} - E_i^{pred}}{\Delta E_i^{meas}} \right) \right),$$

where $E_i^{meas}$ and $E_i^{pred}$ are the measured and predicted strip energy and $\Delta E_i^{meas}$ is the error on the measured strip energy.

**$\delta\phi_{measured}/|\delta\phi_{expected}| < 2.5$** The $\delta\phi_{measured}$ and $\delta\phi_{expected}$ are defined in the previous section. This removes background from the mis-associated SVX tracks.

The additional "High $\eta$ SVX" sample requirements are:

**A 3 or 4 hit SVX Track**

**PEM $\chi^2_\phi < 3$** This measures the shower fit quality in $\phi$ block energies. The PEM $\chi^2_\phi$ is defined as:

$$\chi^2_\phi = \left( \sum_{i=1}^{5} \left( \frac{E_i^{meas} - E_i^{pred}}{\Delta E_i^{meas}} \right) \right),$$

where $E_i^{meas}$ and $E_i^{pred}$ are the measured and predicted PEM $\phi$ block energy and $\Delta E_i^{meas}$ is the error on the measured energy.

**$\delta\phi_{measured}/|\delta\phi_{expected}| < 3$** This quantity is cut at 3.0 instead of 2.5 because the $\delta\phi_{measured}$ resolution is worse for high $\eta$ electrons.

The additional "Low $\eta$ CTC" sample requirements are:

**1 GeV $< P_T <$ 200 GeV**

**$|\delta\phi| <$ 0.04 rad:** The distance (in radians) between the extrapolated CTC track and the position of the EM energy cluster centroid, as determined by the plug strip chamber (PES), is required to be consistent with a high $P_T$ electron.

**$|\delta R| <$ 10.0 cm:** The distance (in cm) between the extrapolated CTC track and the radial position of the EM energy cluster centroid, as determined by the strip chamber, has a loose cut applied because the stereo reconstruction by the CTC can be very poor in the plug region.

**$CurSig > 2.0$.**

The data are further required to originate from good runs (i.e. no known hardware failures). After applying the above cuts, a total of 16235 events remain in the plug $W$ samples. The number of events is 9509, 2944 and 3782 for the "Low $\eta$ SVX", "High $\eta$ SVX" and "Low $\eta$ CTC" samples, respectively. Figure 4.14 shows the transverse mass distribution of all plug $W$ events.

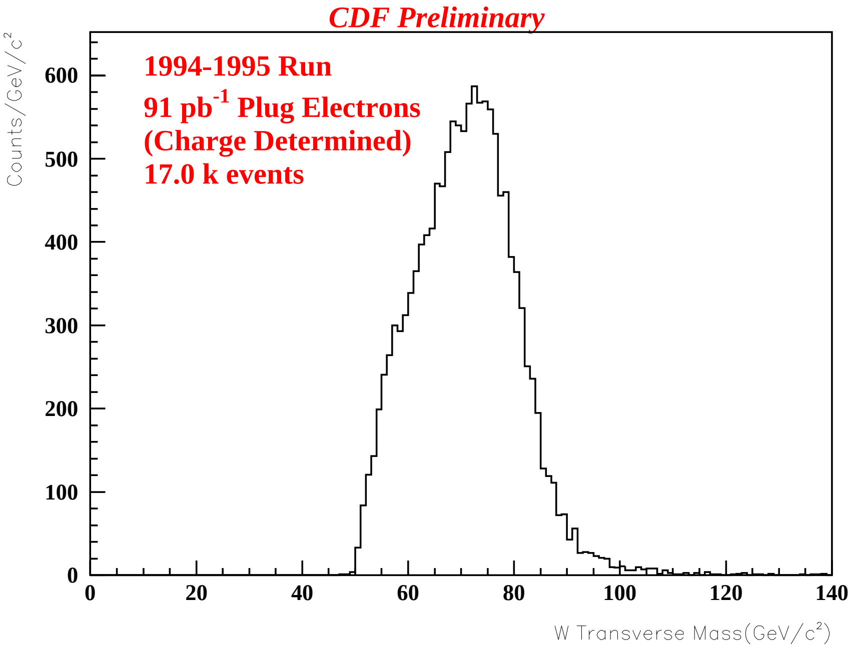

Figure 4.14: *The transverse mass spectrum of plug electron W candidate events.*

## 4.6 Plug $W$ Backgrounds

### QCD Background

The same method is used to determine the fraction of QCD background in the plug $W$ samples. Because the plug isolation variable is less restrictive (the 0.4 cone size in the plug corresponds to smaller physical size than in the central region), the isolation cut is chosen to be half the size (0.15 instead of 0.30). Figure 4.15 shows the $Isolation$ distributions for the QCD background control samples, and for the signal sample.

The QCD background in the CTC $W$ sample is estimated to be $2.9 \pm 0.4\%$ and $2.5 \pm 0.3\%$ using QCD samples I and II, respectively. This gives the fraction of background in the CTC $W$ sample $2.7 \pm 0.5\%$. We estimate the QCD background in the SVX sample to be $1.4 \pm 0.1\%$ and $1.3 \pm 0.1\%$, using QCD samples I and II, respectively. The average of two gives $1.4 \pm 0.1\%$. A larger QCD background is expected in the plug $W$ sample than in the central $W$ sample, because the QCD background is flat as a function of $\eta$, while the $W$ cross section drops quickly. The SVX sample has smaller background as the SVX track requirement reduces the background from photon conversions.

### Other Backgrounds

Similar methods to those used for the central datasets are used to estimate the fractions of the other backgrounds in the plug $W$ samples. The $W \to \tau\nu$ background is estimated to be $(2.0 \pm 0.2)\%$. The $Z \to ee$ background in the plug $W$ sample is $(0.20 \pm 0.06)$. The $Z \to \tau^+\tau^-$ background is $(0.10 \pm 0.06)$.

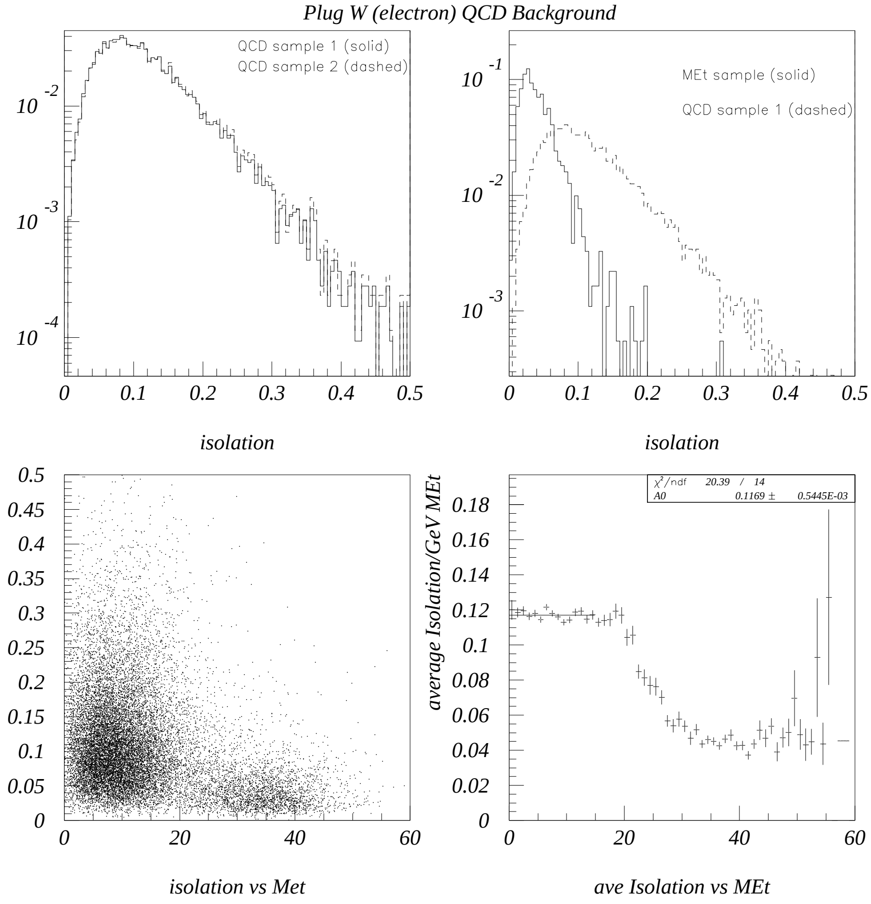

Figure 4.15: (a) Isolation in a cone of $R$=0.4 ($Isolation$) for the two plug $W$ QCD background samples, (b) for the signal sample (minus the isolation cut) and the control sample 1. (c) A scatter plot of $Isolation$ vs $\not{E}_T$ in the inclusive central electron sample and d) the average $Isolation$ as a function of $\not{E}_T$.

## 4.7 Charge Independence Verifications

### Detector Acceptance

As is done for the central region, the detector acceptance for the plug $W$ electron events is checked for any charge bias. Table 4.1 compares the mean and rms of detector rapidity $\eta$ distributions for positrons and electrons in the final asymmetry sample. No charge dependence of detector acceptance is evident.

### Identification Requirements

As in the central $W$ case, the plug electron identification requirements are checked for any charge bias. The distributions of the plug electron identification variables are shown in Figure 4.16. No charge bias in the electron identification requirements is evident.

### Plug Electron Triggers

There are two plug electron triggers, the "PEM_20" and "PEM_15_MET_15". The "PEM_15_MET_15" trigger is prescaled at high luminosity due to its high trigger rate. Figure 4.17 shows the trigger efficiency for the primary plug electron trigger "PEM_20". The trigger efficiency is determined by using events that contains plug electrons but are accepted by triggers other than the plug electron triggers. The $Z$ vertex information is not available in the Level 2 trigger thus $E_T$ is calculated by assuming that event vertex is at $Z = 0$. This results in a slow "turn-on" of the trigger efficiency. The slight difference between the East and West PEM in the trigger efficiency curves is mainly due to the positive $Z$ vertex distribution. The trigger efficiency curve of the OR of two triggers is shown in Figure 4.18. The curves and their errors are used as input to determine the amount of needed

| *Event* $\eta$ | *Detector* $\eta$ | | | |
|---|---|---|---|---|
| | *Positive Charges* | | *Negative Charges* | |
| | *mean* | *rms* | *mean* | *rms* |
| *Low* $\eta$ *SVX Sample* | | | | |
| 1.0∼ 1.2 | 1.235 | 0.026 | 1.236 | 0.036 |
| 1.2∼ 1.4 | 1.306 | 0.064 | 1.305 | 0.063 |
| 1.4∼ 1.7 | 1.511 | 0.101 | 1.510 | 0.100 |
| 1.7∼ 2.0 | 1.719 | 0.058 | 1.716 | 0.057 |
| -1.0∼-1.2 | -1.231 | 0.022 | -1.241 | 0.037 |
| -1.2∼-1.4 | -1.301 | 0.064 | -1.304 | 0.063 |
| -1.4∼-1.7 | -1.506 | 0.101 | -1.500 | 0.102 |
| -1.7∼-2.0 | -1.714 | 0.059 | -1.716 | 0.057 |
| *High* $\eta$ *SVX Sample* | | | | |
| 1.7∼ 2.1 | 1.915 | 0.079 | 1.911 | 0.078 |
| 2.1∼ 2.4 | 2.117 | 0.063 | 2.112 | 0.066 |
| -1.7∼-2.1 | 1.913 | 0.078 | 1.914 | 0.077 |
| -2.1∼-2.4 | 2.105 | 0.071 | 2.106 | 0.069 |
| *Low* $\eta$ *CTC Sample* | | | | |
| 1.0∼ 1.2 | 1.283 | 0.061 | 1.283 | 0.054 |
| 1.2∼ 1.4 | 1.372 | 0.101 | 1.365 | 0.094 |
| 1.4∼ 1.7 | 1.448 | 0.117 | 1.454 | 0.115 |
| 1.7∼ 2.0 | 1.599 | 0.071 | 1.625 | 0.068 |
| -1.0∼-1.2 | -1.274 | 0.044 | -1.272 | 0.046 |
| -1.2∼-1.4 | -1.352 | 0.088 | -1.346 | 0.089 |
| -1.4∼-1.7 | -1.416 | 0.111 | -1.398 | 0.113 |
| -1.7∼-2.0 | -1.601 | 0.064 | -1.589 | 0.062 |

Table 4.1: Comparison of the mean and rms of detector rapidity distributions for positrons and electrons in the final asymmetry sample.

correction and the systematic error of the $E_T$ dependence of the trigger efficiency.

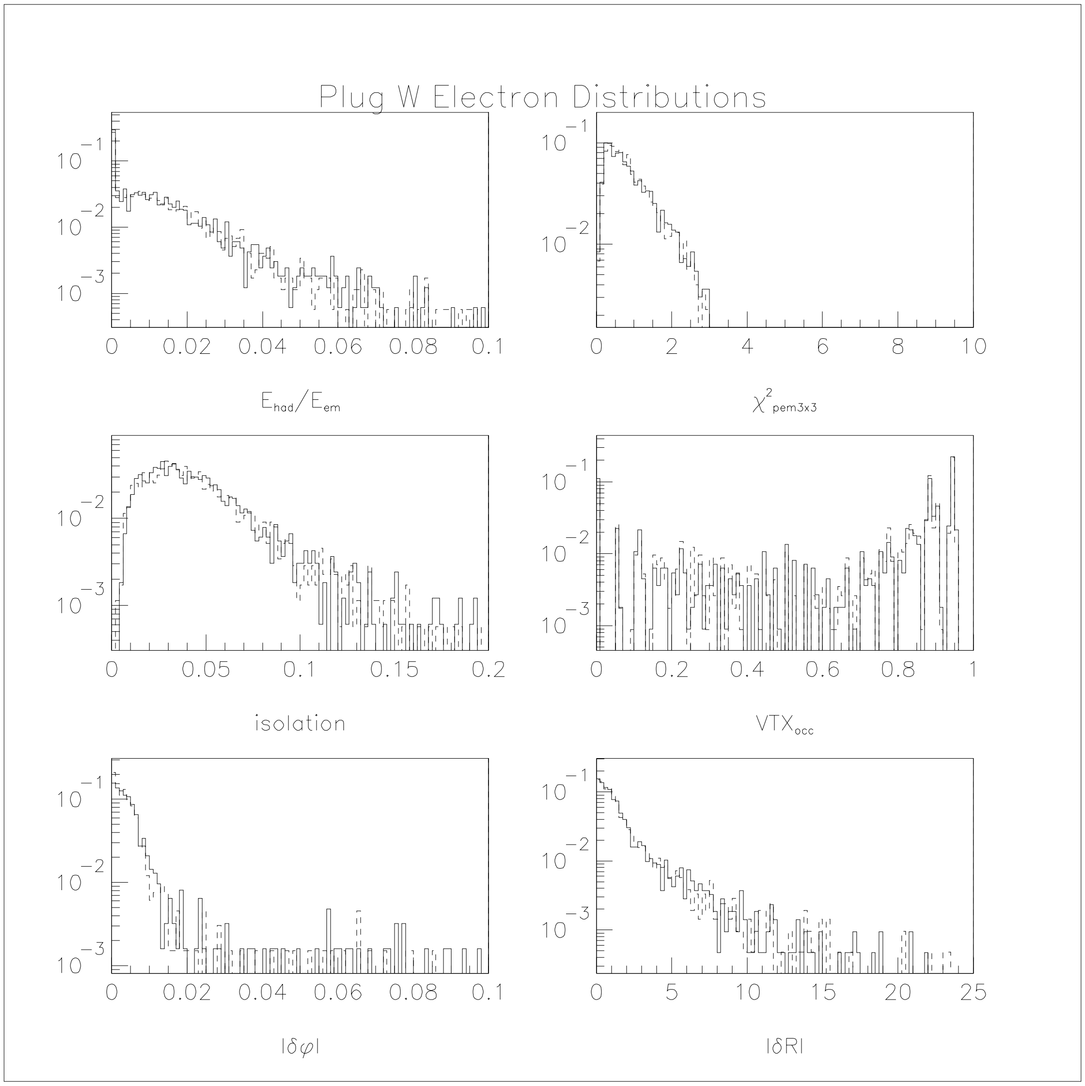

Figure 4.16: The distributions of the plug electron identification variables. The solid histograms and the dashed histograms are from the $e+$ and $e-$ separately. The distributions are the same for the plus and minus charges.

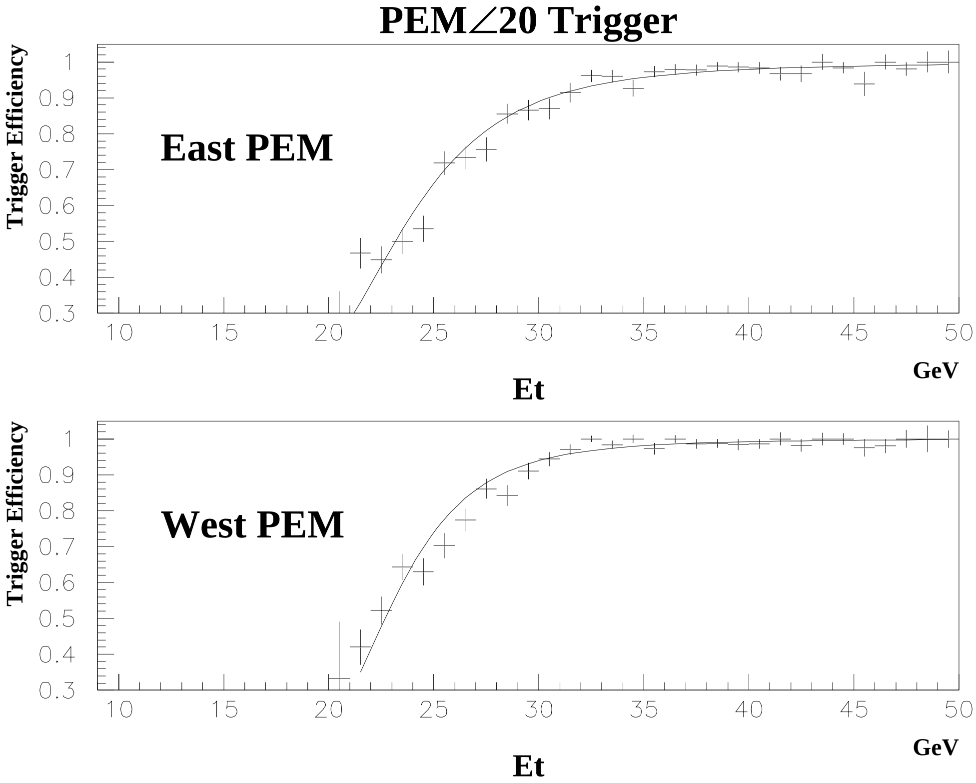

Figure 4.17: The "PEM_20" trigger efficiency requires the presence of a cluster with $E_T > 20$ GeV.

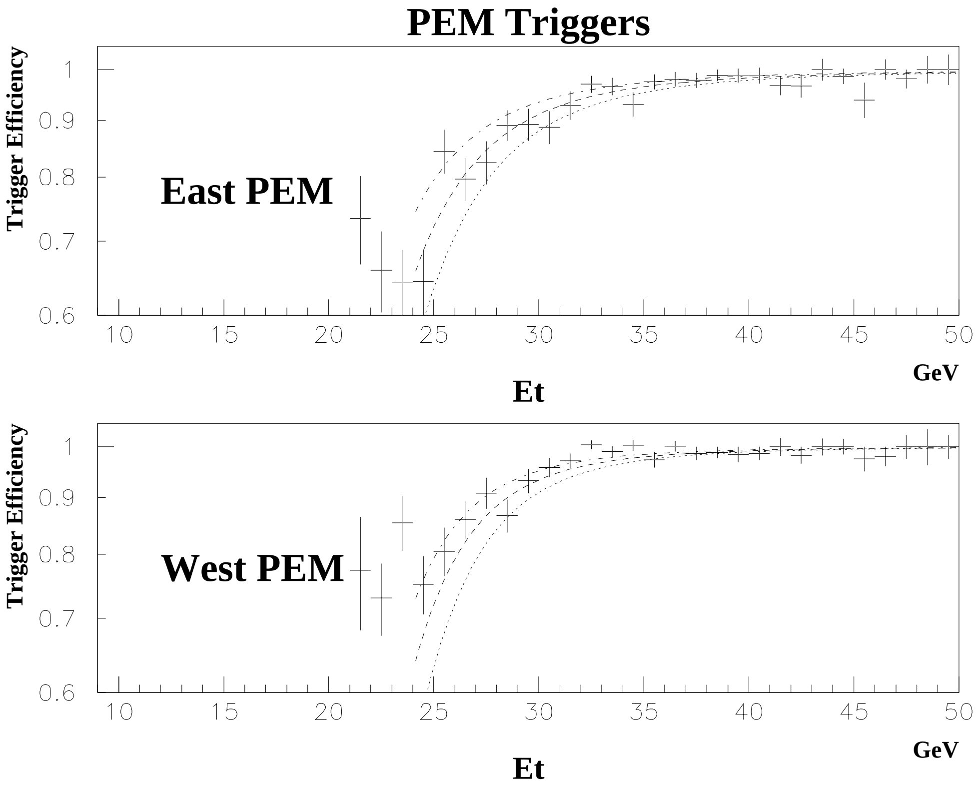

Figure 4.18: The trigger efficiency of the OR of the two plug electron triggers "PEM_15_MET_15" and "PEM_20". (Note that $E_T > 25$ GeV is required in the analysis.)

# Chapter 5

# Foward $W \rightarrow \mu + \nu$

The detailed analysis is documented in [13]. Here only a summary of the analysis is described. The forward muon detector covers the pseudo-rapidity region $1.9 < |\eta| < 3.5$. In the pseudo-rapidity region $2.5 < |\eta| < 3.6$ (uncovered by PHA), charged pions contained in the QCD jets could decay into a muon before reaching FHA. This results in large backgrounds in the forward $W$ muon sample. Therefore, only data from $1.9 < |\eta| < 2.5$ regions of the FMU are used in the $W$ asymmetry analysis. The prescaling in the forward muon trigger due to high trigger rate reduces the total amount of FMU data to approximately 70 $pb^{-1}$. The data sample is selected with the same kinematic cuts, i.e. $E_T > 25$ GeV and $\not{E}_T > 25$ GeV. A total of 2035 $W$ candidates are in the final sample. The $\mu^+$'s and $\mu^-$'s are bent by the toroids into different regions of the detector, which results in the acceptance difference across charge. In addition, the position of the muon detector is known to certain precision in the trigger. In order to cancel the possible charge bias between $\mu^+$'s and $\mu^-$'s in the detector acceptance and trigger efficiency, the data taken with toroids in both polarities are averaged. The asymmetry calculated with Equation 3.9 is $A(2.2) = -0.066 \pm 0.025 \pm 0.016$. The first error is statistical and the second is systematic uncertainty. The correction is made for the $(10 \pm 1)\%$ QCD backgrounds in the $W$ sample.

# Chapter 6

# $W \to l\nu$ Charge Asymmetry

The lepton charge asymmetry is defined in 1.1 as:

$$A(y_l) = \frac{d\sigma^+/dy_l - d\sigma^-/dy_l}{d\sigma^+/dy_l + d\sigma^-/dy_l},$$

where $\sigma^+$ and $\sigma^-$ are simply the cross sections of $W$ decay leptons. Experimentally, we measure the number of leptons within a particular lepton rapidity bin, i.e. $N^+(y_l)$ and $N^-(y_l)$. Because the detection efficiencies as well as acceptances for $l^+$'s and $l^-$'s are equal as shown in Chapters 3 and 4, the lepton asymmetry is simply

$$A(y_l) = \frac{N^+(y_l) - N^-(y_l)}{N^+(y_l) + N^-(y_l)},$$

where $y_l$ is the mean of the lepton rapidity for events in a rapidity bin.

Table 6.1 lists the categories of the 85,347 $W$ lepton candidates in the Run 1B data samples that are discussed in Chapters 3 & 4. Adding 2035 forward $W$ muons and 19,032 events from the Run 1A $W$ samples, a total of 106,414 $W$ candidate events are used in the asymmetry analysis. Figure 6.1 shows the observed charge asymmetry as a function of lepton rapidity from the Run 1B $W$ samples.

| $\lvert\eta\rvert$ bin | $\langle\eta\rangle$ | +Q/+Y | -Q/+Y | $\langle\eta\rangle$ | -Q/-Y | +Q/+Y | Total |
|---|---|---|---|---|---|---|---|
| Central Electrons | | | | | | | |
| 0.0-0.2 | 0.10 | 2030 | 1936 | -0.11 | 1897 | 1897 | 7760 |
| 0.2-0.4 | 0.30 | 2431 | 2218 | -0.30 | 2178 | 2393 | 9220 |
| 0.4-0.6 | 0.50 | 2696 | 2251 | -0.50 | 2087 | 2591 | 9625 |
| 0.6-0.8 | 0.70 | 2543 | 1987 | -0.70 | 1929 | 2596 | 9055 |
| 0.8-1.0 | 0.89 | 1967 | 1486 | -0.89 | 1541 | 2040 | 7034 |
| 1.0-1.2 | 1.05 | 382 | 288 | -1.05 | 368 | 464 | 1502 |
| Central Muons | | | | | | | |
| 0.0-0.2 | 0.11 | 1555 | 1531 | -0.11 | 1359 | 1480 | 5925 |
| 0.2-0.4 | 0.30 | 2027 | 1766 | -0.30 | 1744 | 1862 | 7399 |
| 0.4-0.6 | 0.48 | 1313 | 1112 | -0.48 | 1080 | 1299 | 4804 |
| 0.6-0.8 | 0.71 | 1063 | 751 | -0.71 | 816 | 990 | 3620 |
| 0.8-1.0 | 0.89 | 937 | 710 | -0.90 | 740 | 971 | 3358 |
| 1.0-1.2 | 1.02 | 121 | 83 | -1.03 | 94 | 134 | 432 |
| Plug Electrons (Low $\eta$ CTC) | | | | | | | |
| 1.0-1.2 | 1.13 | 295 | 197 | -1.12 | 137 | 192 | 821 |
| 1.2-1.4 | 1.30 | 434 | 344 | -1.30 | 267 | 329 | 1374 |
| 1.4-1.7 | 1.52 | 376 | 296 | -1.51 | 261 | 297 | 1230 |
| 1.7-2.0 | 1.81 | 57 | 50 | -1.79 | 43 | 49 | 199 |
| Plug Electrons (Low $\eta$ SVX) | | | | | | | |
| 1.0-1.2 | 1.17 | 74 | 52 | -1.16 | 53 | 72 | 251 |
| 1.2-1.4 | 1.31 | 794 | 666 | -1.31 | 604 | 812 | 2876 |
| 1.4-1.7 | 1.55 | 1231 | 953 | -1.54 | 965 | 1283 | 4432 |
| 1.7-2.0 | 1.80 | 374 | 340 | -1.79 | 389 | 457 | 1560 |
| Plug Electrons (High $\eta$ SVX) | | | | | | | |
| 1.7-2.1 | 1.94 | 495 | 487 | -1.95 | 487 | 524 | 1993 |
| 2.1-2.4 | 2.21 | 204 | 230 | -2.20 | 265 | 178 | 877 |

Table 6.1: Number of $W$ lepton candidate events measured from the Run 1B $W$ data samples. There are 44,196 central electrons, 25,538 central muons, 3,624 CTC plug electrons, 9,119 low $\eta$ SVX plug electrons and 2,870 high $eta$ plug electrons. The total number of $W \rightarrow e, \mu + \nu$ candidate events is 85,347.

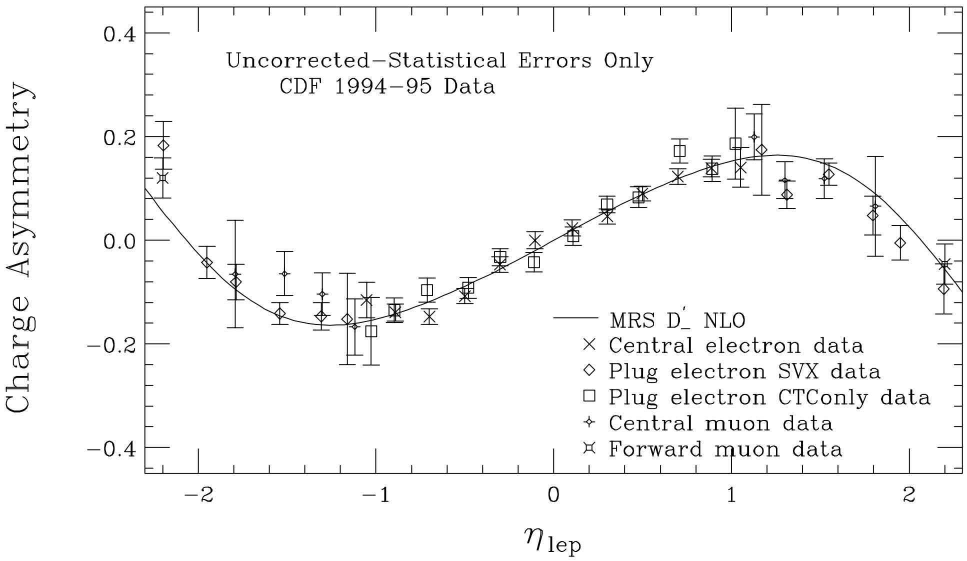

Figure 6.1: The observed lepton charge asymmetry from the Run 1B $W$ samples.

## 6.1 The Corrections and the Systematic Errors

There are several sources of experimental effects which modify the observed lepton asymmetry. The backgrounds remaining in the $W$ data samples act to dilute the lepton asymmetry. Similarly the presence of charge misidentification also dilutes the measurement. The "turn-on" effect (versus transverse energy) in the plug electron triggers discussed in Chapter 4 results in a small modification of the observed asymmetry as well. Therefore, the measured asymmetry in Equation 3.9 needs to be corrected for the known effects. The dominant uncertainty in the measurement is the statistical error. The uncertainties in the estimation of backgrounds as well as other experimental effects are included in the systematic errors.

### 6.1.1 Trigger

The trigger efficiencies for $l^+$'s and $l^-$'s are shown to be equal and therefore cancel in the measurement of the asymmetry. The central lepton triggers have no $E_T$ or $P_T$ dependence for leptons with $E_T > 25$ GeV. Therefore, no correction is needed in the central $W$ lepton triggers. There is an $E_T$ dependence in the plug $W$ electron triggers. Therefore, a correction on the observed asymmetry is needed. The DYRAD Monte Carlo is employed in which the measured plug electron trigger efficiency curves are used as input. By comparing the calculated asymmetries with and without taking into account the $E_T$ dependence of the trigger efficiency, a correction on the asymmetry is determined. The uncertainty on the correction is estimiated from change in asymmetry by varying the estimated trigger efficiency curves within 1 $\sigma$ of the best fit. The correction extracted using different PDFs is only slightly different, and is included in the uncertainty. The correction and its uncertainty as a function of lepton rapidity are shown in Figure 6.2.

### 6.1.2 Energy/Momentum Scale

The uncertainty in the lepton energy or momentum scale affects the asymmetry through the lepton transverse energy or momentum requirement. As discussed in Chapters 3 & 4, there is a 1% uncertainty in the energy or momentum scale. The uncertainty in the jet energy scale has a small effect on the asymmetry measurement. In both cases, the uncertainties on the asymmetry is estimated from the DYRAD Monte Carlo calculation. The magnitude of these uncertainties are shown in Figure 6.3.

### 6.1.3 Charge Mis-identification

The charge mis-identification rate is defined as the probability of a positively

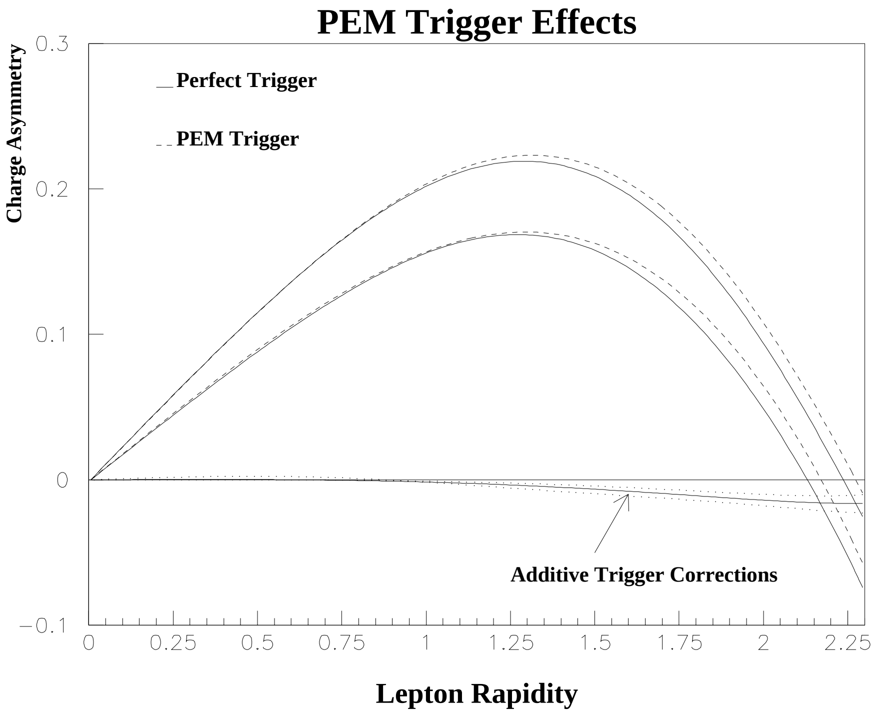

Figure 6.2: The corrections needed to account for the PEM electron trigger effects. The uncertainty on the correction is mainly determined by the uncertainty in the measured trigger efficiency curve. The upper and lower curves are the asymmetry predictions using different PDFs. The third curves is the overall correction to the measured asymmetry.

(negatively) charged track being wrongly identified as a negatively (positively) charged track. For the central $W \rightarrow e/\mu + \nu$ events, the good momentum resolution of CTC tracking ensures charge identification with high certainty. The charge is mis-identified in the rare case when a wrong CTC track is associated with the EM cluster. The CTC tracking does not provide as good momentum resolution for the plug $W$ electrons as in the central region, but is still sufficiantly good to provide charge identification. The charge identification using the SVX method is limited by the PEM's position resolution in the high $\eta$ region ($|\eta| > 1.8$), as discussed in Chapter 4. In the presence of charge mis-identification, the relation between the

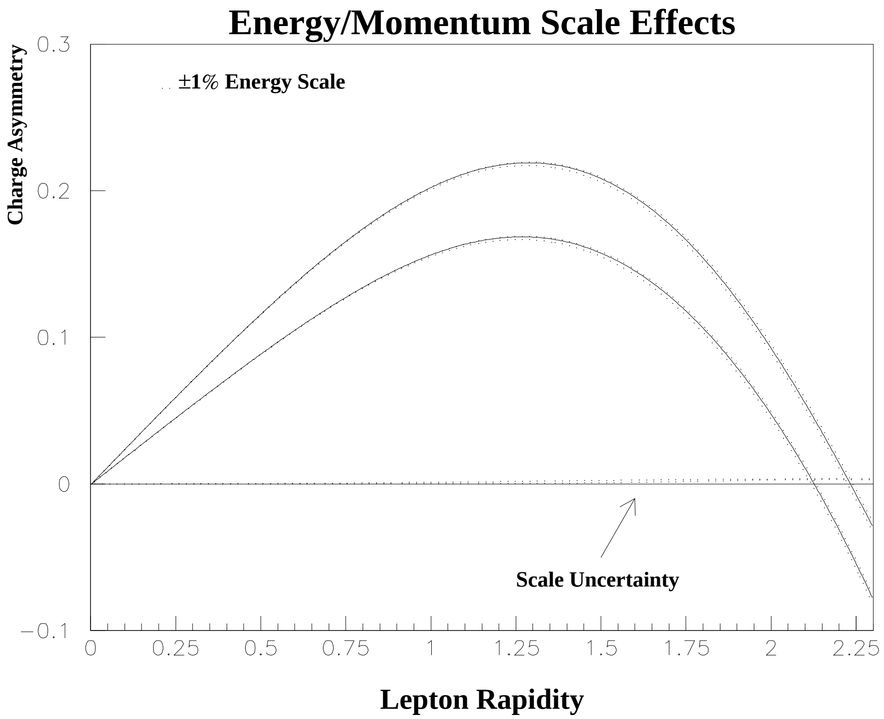

Figure 6.3: The uncertainty in asymmetry caused by the uncertainty in the energy/momenum scale of the detector is small.

observed charge asymmetry $A_{obs}$ and the true asymmetry $A_{true}$ is:

$$A_{true} = \frac{A_{obs}}{1 - 2\epsilon},$$

where $\epsilon$ is the charge mis-identification rate. The magnitude of the correction is shown in Table 6.2.

### 6.1.4 PEM Alignment

After applying the alignment corrections discussed in Chapter 4, the PEM is aligned to better than 0.5 mrad in $\phi$. In the case of using the SVX method to identify the plug electron charge, a possible residual mis-alignment left in the

| Data Sample | $\|y_l\|$ Range | Charge Mis-id Rate | $\delta A/A_{obs}$ |
|---|---|---|---|
| Central $e/\mu$ | $\|y_l\| < 1.2$ | $(0.2 \pm 0.1)\%$ | $(0.4 \pm 0.2)\%$ |
| Plug e (Low $\eta$ CTC) | $1.0 < \|y_l\| < 2.0$ | $(0.4 \pm 0.2)\%$ | $(0.8 \pm 0.4)\%$ |
| Plug e (Low $\eta$ SVX) | $1.0 < \|y_l\| < 2.0$ | $(0.8 \pm 0.2)\%$ | $(1.6 \pm 0.2)\%$ |
| Plug e (High $\eta$ SVX) | $1.7 < \|y_l\| < 2.1$ | $(2.0 \pm 0.2)\%$ | $(4.0 \pm 0.4)\%$ |
|  | $2.1 < \|y_l\| < 2.4$ | $(10 \pm 1)\%$ | $(25 \pm 3)\%$ |

Table 6.2: The charge asymmetry corrections due to charge mis-identification for the different asymmetry samples.

PEM can cause a charge bias thus affect the charge asymmetry. This effect is negligible for the "Low $\eta$ SVX" plug electron sample, because the two charges are well separated in $\phi$. For the "High $\eta$ SVX" plug electron sample, the two charges are not completely separated. Therefore, the effect on the asymmetry measurement is estimated using a Monte Carlo simulation. A total of 20 sets of alignment constants are randomly generated with each constant varying according to a gaussian distribution with a rms of 0.5 mrad. The measured asymmetry is re-extracted using each new set of alignment constants. The variation in the observed asymmetry is taken as the systematic error in the asymmetry from the uncertainty in the alignment of the PEM. The errors corresponding to the two rapidity bins (1.7,2.1) and (2.1,2.4) are 0.009 and 0.017 separately.

### 6.1.5 Backgrounds

Table 6.1.5 summarizes the various sources of backgrounds remaining in the $W$ samples. In the presence of background, the relation between the observed charge asymmetry $A_{obs}$ and the true asymmetry $A_{true}$ is:

$$A_{true} = (1 + \epsilon)(A_{obs} - \epsilon A^b),$$

| Source | Central $e$ | Plug-CTC $e$ | Plug-SVX $e$ | Central $\mu$ | Forward $\mu$ |
|---|---|---|---|---|---|
| $W \to \tau\nu$ | $\mathbf{2.0 \pm 0.2}$ | $\mathbf{2.0 \pm 0.2}$ | $\mathbf{2.0 \pm 0.2}$ | $\mathbf{2.0 \pm 0.2}$ | $\mathbf{2.0 \pm 0.2}$ |
| QCD | $\mathbf{0.7 \pm 0.2}$ | $\mathbf{2.7 \pm 0.5}$ | $\mathbf{1.4 \pm 0.1}$ | $\mathbf{0.6 \pm 0.2}$ | $\mathbf{10 \pm 1}$ |
| $Z \to ee$ *or* $\mu\mu$ | $< 0.2$ | $< 0.2$ | $< 0.2$ | $\mathbf{4.7 \pm 0.7}$ | $6.5 \pm 0.6$ |

Table 6.3: Backgrounds (%) in the $W \to e\nu$ and $W \to \mu\nu$ charge asymmetry event samples. The values in boldface are used to correct the measurement in conjunction with the background's charge asymmetry.

where $\epsilon$ is the fraction of the background in the $W$ sample and $A^b$ is the charge asymmetry in the background. The observed asymmetry is corrected.

### QCD

The charge asymmetry in the backgrounds from mis-identified QCD jets is expected to be zero. This agrees with a check with a sample of QCD jet events. The effect of QCD backgrounds in the $W$ sample on the asymmetry is removed by increasing the observed asymmetry by a factor of $\epsilon$, the fraction of the mis-identified QCD jet events in the $W$ sample.

### $W \to \tau\nu \to l\nu\nu$

The charge asymmetry in this contribution is calculated from Monte Carlo. Figure 6.4 shows the expected charge asymmetry for this source. The two dashed lines indicate the range of asymmetry due to different PDFs. The effect of $\tau$ background is small, because the asymmetry is similar to that in the $W \to l\nu$ process.

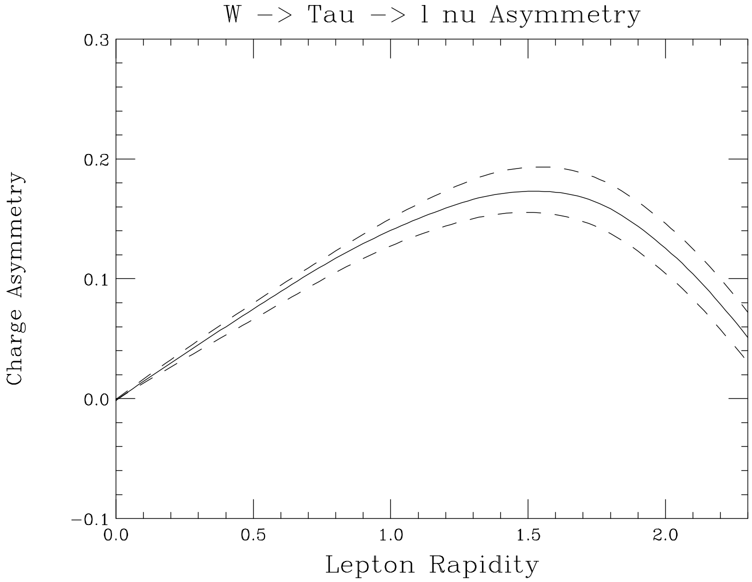

Figure 6.4: The calculated lepton charge asymmetry in the $W \rightarrow \tau\nu \rightarrow l\nu\nu$ process. The two dashed lines indicate the range of asymmetry predicted by different PDFs.

### $Z \rightarrow \mu + lost\ \mu$

The asymmetry in the process $Z \rightarrow \mu + lost\ \mu$ is calculated using the DYRAD Monte Carlo. The CTC tracking efficiency is assumed 100% in the central region ($|\eta| < 1.2$). In the plug region ($1.2 < |\eta| < 1.8$), the tracking efficiency is taken from the Figure 4.7, where a 10% uncertainty is assumed. The $Z$ asymmetry is not sensitive to the PDFs. Therefore, the error on the asymmetry is entirely due to the 10% uncertainty in tracking efficiency. Figure 6.5 shows the expected lepton charge asymmetry in $Z \rightarrow \mu\mu$ events, where one of the $\mu$'s is undetected.

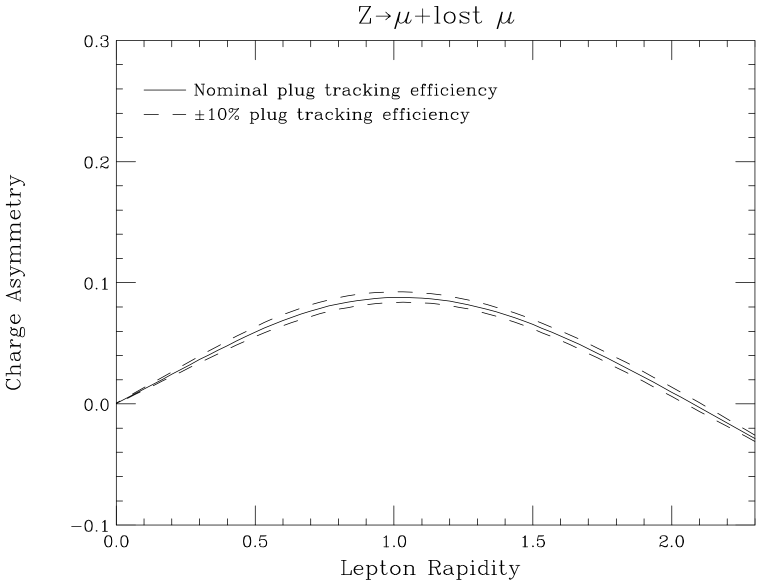

Figure 6.5: The calculated lepton charge asymmetry in the $Z \to \nu\nu$ process where one of the $\mu$'s is lost. The two dashed lines indicate the range of asymmetry affected by the ±10% change in the CTC tracking efficiency.

## 6.2 The Corrected Charge Asymmetry

Because the asymmetry at positive rapidity is equal in magnitude and opposite in sign to that at negative rapidity, the asymmetry value at positive $y_l$ is combined with that at negative $y_l$. The above corrections are then applied as a function of rapidity. The Run 1B asymmetry values are further combined with the published Run 1A measurements. Figure 6.7 shows the corrected asymmetry as a function of lepton rapidity $|y|$ after all the data have been combined. The asymmetry measured from the Run 1B data before and after the above corrections are shown in Table 6.4. The statistical error remains the dominated uncertainty.

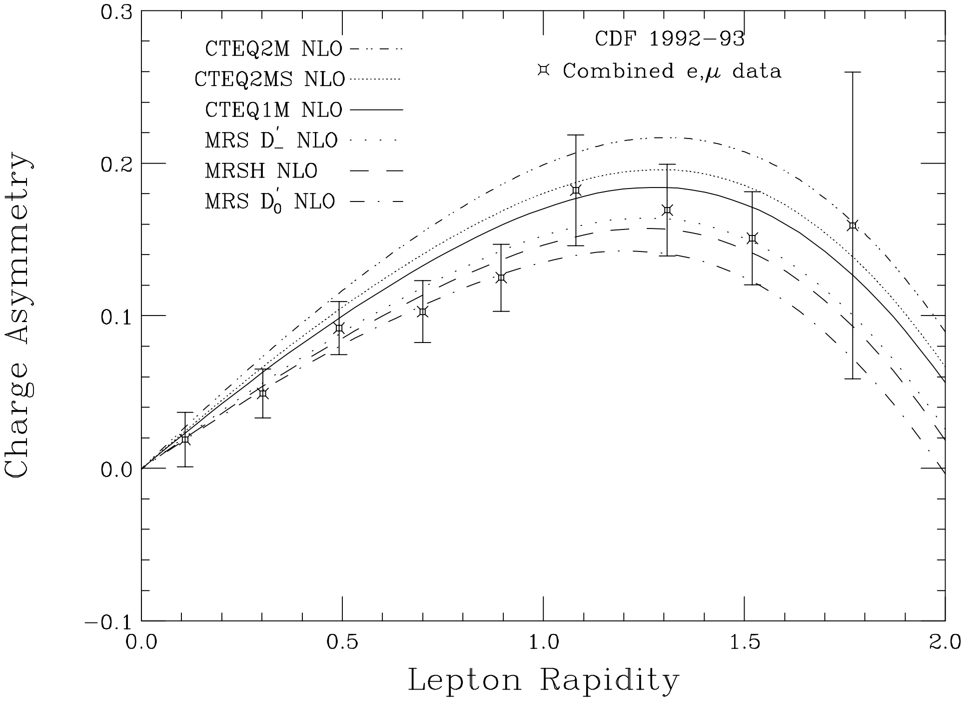

Figure 6.6: The asymmetry predictions , compared to predictions of the old PDF's. Also shown are the previous CDF data fully corrected for trigger and backgrounds (systematic errors are included).

## 6.3 The Theorectical Predictions

The Dyrad $W/Z$ Monte Carlo is used to calculate the theorectical predictions for the lepton charge asymmetry using different input PDFs. The Dyrad Monte Carlo calculates the process $p\overline{p} \rightarrow W + X \rightarrow l + \nu + X$ at next-to-leading order (NLO). It includes the production of $W$ plus 0 and 1 jet followed by the leptonic decay of the $W$. The clustering of the jet energy in a $R = 0.7$ cone is included in the calculation. The determination of $\not{E}_T$ takes into account of the detector limitation in in terms of the $\eta$ coverage (at CDF, $\not{E}_T$ is calculated from all energy within $|\eta| < 3.6$). The NLO calculations do not reproduce the $W$ $P_T$ correctly especially at very low

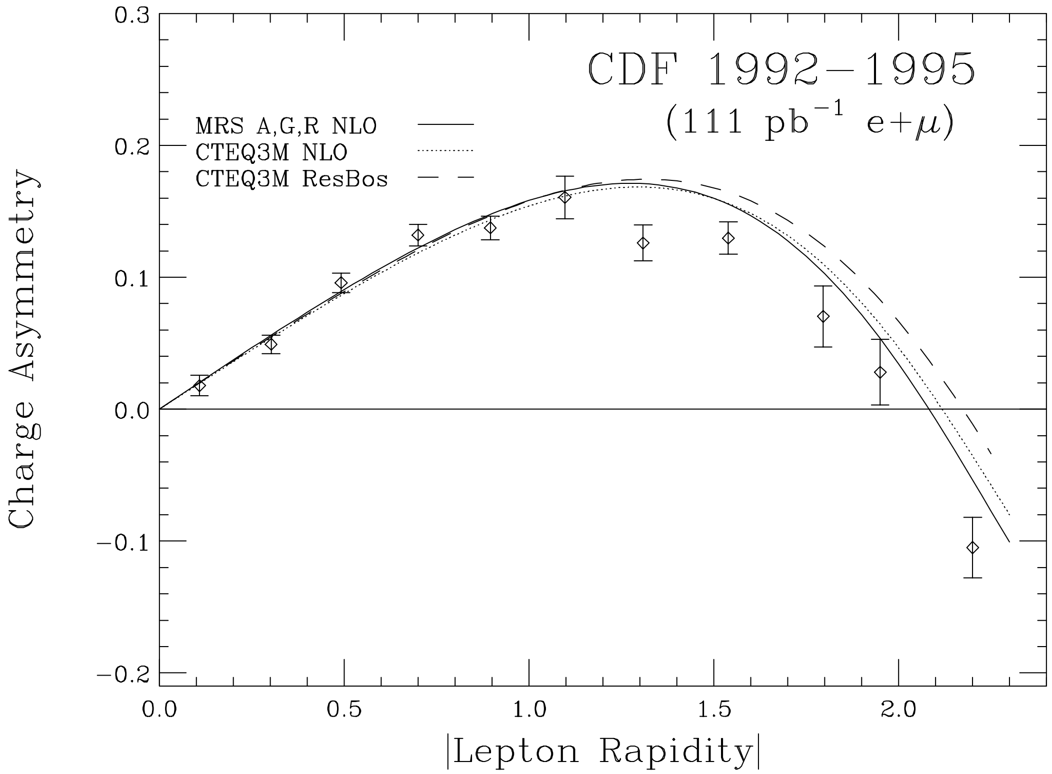

Figure 6.7: The fully corrected charge asymmetry. Data from all the various detectors for positive and negative $y$ have been combined.

$P_T$. Because the $W$ lepton charge asymmetry may be somewhat affected by the $W$ production $P_t$ spectrum, it is necessary to check how well NLO DYRAD calculation compares to an independent calculation. The DYRAD prediction is compared to a calculation using a gluon resummation technique [5] (ResBos) . The resummation calculation takes into account of soft gluon radiation which (at Tevatron energies) is mainly responsible for the $P_T$ of $W's$ in the range of $P_t < 30$ GeV. Figure 6.7 also shows the comparison between predictions from DYRAD NLO and ResBos for the CTEQ3M [25] structure functions. The difference between two calculations is mainly at $|y_l| > 1.7$. It's worth noting that the disagreement between our data

| $\|\eta\|$ bin | $\langle\|\eta\|\rangle$ | $A^{raw}(y_l)$ | $A^{cor}(y_l)$ | $\sigma_{stat}$ | $\sqrt{\sigma^2_{stat}+\sigma^2_{sys}}$ |
|---|---|---|---|---|---|
| 0.0-0.2 | 0.105 | 0.017 | 0.018 | ±0.009 | ±0.009 |
| 0.2-0.4 | 0.302 | 0.049 | 0.049 | ±0.008 | ±0.008 |
| 0.4-0.6 | 0.500 | 0.095 | 0.097 | ±0.008 | ±0.008 |
| 0.6-0.8 | 0.699 | 0.135 | 0.138 | ±0.009 | ±0.009 |
| 0.8-1.0 | 0.887 | 0.138 | 0.141 | ±0.010 | ±0.010 |
| 1.0-1.2 | 1.052 | 0.154 | 0.157 | ±0.018 | ±0.018 |
| 1.2-1.4 | 1.313 | 0.115 | 0.114 | ±0.015 | ±0.015 |
| 1.4-1.7 | 1.548 | 0.126 | 0.123 | ±0.013 | ±0.013 |
| 1.7-2.0 | 1.796 | 0.065 | 0.056 | ±0.024 | ±0.024 |
| 1.7-2.1 | 1.947 | 0.023 | 0.010 | ±0.022 | ±0.022 |
| 1.9-2.5 | 2.204 | -0.095 | -0.118 | ±0.022 | ±0.022 |

Table 6.4: Measured Run 1B charge asymmetry in the combined $e$ and $\mu$ channels.

and the resummed Monte Carlo calculation is even bigger at high lepton rapidity than the disagreement with NLO DYRAD calculation.

The theoretical uncertainties arising from effect of the finite charm quark mass have been investigated and are found to be negligible. The asymmetry calculated with GRV92 [27] and massive charm is slightly higher than calculated with GRV92 and massless charm by 0.002, 0.003 and 0.002 at $y_l$ of 0.55, 1.05 and 1.55 respectively [26]. The differences are much smaller than the measurement error of 0.007,0.016 and 0.012 respectively.

## 6.4 Comparison with Predictions

The rapidity of $W$'s which contribute to the lepton rapidity bin are estimated using the DYRAD Monte Carlo and is summarized in Table 6.4. The CDF asymmetry data probe the slope of $d(x)/u(x)$ of the proton structure in the $x$ range between 0.006-0.34.

| | $W^+$ | | $W^-$ | |
|---|---|---|---|---|
| $< y_l >$ | $< x_u >$ | $< x_d >$ | $< x_d >$ | $< x_u >$ |
| -2.20 | 0.009 | 0.219 | 0.335 | 0.006 |
| -1.54 | 0.016 | 0.129 | 0.225 | 0.009 |
| -1.10 | 0.021 | 0.088 | 0.165 | 0.012 |
| -0.49 | 0.038 | 0.051 | 0.099 | 0.021 |
| 0.49 | 0.099 | 0.021 | 0.038 | 0.051 |
| 1.10 | 0.165 | 0.012 | 0.021 | 0.088 |
| 1.54 | 0.225 | 0.009 | 0.016 | 0.129 |
| 2.20 | 0.335 | 0.006 | 0.009 | 0.219 |

Table 6.5: The $x$ ranges of $d$ and $u$ in the nucleon that are probed by CDF $W$ asymmetry data.

Figure 6.6 shows the previous CDF 1992-1993 $W$ lepton charge asymmetry data along with DYRAD predictions with some of the old PDFs. The predictions essentially have the same shape but a different overall level, which is related to the slope of the d/u ratio as shown in Chapter 1. These PDFs were extracted from DIS data before the CDF 1992-1993 data were published. This is in contrast to the predictions of the recent PDFs which have been extracted with the inclusion of the CDF 1992-1993 asymmetry data. As shown in Figure 6.7, the predictions from the recent MRS PDFs (i.e., the MRSA [28] and later ones), and from the recent CTEQ PDFs (i.e., the CTEQ3M [25]) differ to a much smaller extent. This shows the unique power of $W$ charge asymmetry data in constraining the proton structure functions. The difference between the predictions of the recent PDFs and the CDF 1992-1995 data at large lepton rapidity ($|y_l| > 1.2$) exists. This figure illustrates the unique power of the $W$ charge asymmetry data in constraining proton structure functions. The difference between the predictions of the recent PDFs and the CDF 1992-1995 data at large lepton rapidity ($|y_l| > 1.2$) remains. The new data imply that the slope of the d/u ratio in the proton at small x needs to be further tuned even for these most recent PDFs.

# Bibliography

[1] F. Abe *et al.*, Phys Rev. Lett. **74**, 850 (1995).

[2] R.Hamberg *et al.*, Nuclear Physics **B359** 343 (1991).

[3] E.L.Berger *et al.*, Phys. Rev. D **40**,83 (1989).

[4] A.D.Martin, R.G.Roberts and W.J.Stirling, Mod. Phys. Lett. A **4**,1135(1989).

[5] C. Balazs, J. Qiu and C.P. Yuan, Phys.Lett. **B355** 548-554 (1995).

[6] W. Giele, E. Glover and D.A. Kosower, Nucl. Phys. **B403**, 633 (1993).

[7] M.Arneodo *et al.*, Phys. Letts. B **364** 107 (1995).

[8] M.R.Adams *et al.*, Phys. Rev. **D54** 3006 (1996).

[9] L. Whitlow *et al.*, Phys. Lett. B **282**, 475 (1992); M. Arneodo *et al.*, Phys. Lett. B **309**, 222 (1993); M. Virchaux and M. Milsztajn, Phys. Lett. B **274**, 221 (1992).

[10] B. Badelek, J. Kwiecinski, Nucl. Phys. B **370**, 278 (1992); Note that these deuteron shadowing corrections are model dependent and it is not clear whether they should or should not be applied to the data.

[11] F. Abe *et al.*, Phys Rev. Lett. **75**, 11 (1995).

[12] For a detailed description, see F. Abe *et al.*, Nucl. Instrum. Methods Phys. Res., Sect. A **271**, 387 (1988), and references therein.

[13] Lee Pondrom, "*W* Charge Asymmetry with Forward Muon ", CDF Internal Note 3410.

[14] F. Abe *et al.*, Phys. Rev. **D50**, 5535 (1994).

[15] Kevin Einsweiler and Young-Kee Kim, private communication. The CDF implementation of the UA2 LO W/Z Radiative Monte Carlo.

[16] G. Marchesini and B. R. Webber, Nucl. Phys. **B310**, 461 (1988).

[17] M. Krasberg and T. LeCompte, CDF Note #2032 (1993).

[18] A. Byon-Wagner *et al.*, CDF Note #1260 (1990).

[19] K. Pitts, CDF Note #4010 (1996).

[20] Mark Dickson's thesis, 1994.

[21] T.Baumann *et al.*, "Testbeam 1991: PEM Calibrations", CDF Internal Note 1694.

[22] M.Dickson *et al.*, "Testbeam 1991: Determination of the PEM Response Map", CDF Internal Note 1777.

[23] T.Ino *et al.*, "1991/1992 PEM Dead Layer Corrections", CDF Internal Note 1780.

[24] G.A.Akopdjanov *et al.*, NIM **140**, 441 (1977).

[25] H.L.Lai *et al.*, Phys. Rev. D, **51**,4763-4782 (1995)

[26] S.Kretzer,E.Reya and M.Stratmann, Phys. Lett. **B348** 628-632,(1995).

[27] M. Glück, E. Reya and A. Vogt, Z. Phys. **C48**, 471 (1990), **C53**, 127 (1992); Phys. Lett. **B306**, 391 (1993).

[28] A.D.Martin,W.J.Stirling and R.G.Roberts, Phys. Rev. D, **50**,6734-6752 (1994)

# Appendix A

# The CDF Collaboration

F. Abe,[15] H. Akimoto,[34] A. Akopian,[29] M. G. Albrow,[7] S. R. Amendolia,[25] D. Amidei,[18] J. Antos,[31] C. Anway-Wiese,[4] S. Aota,[34] G. Apollinari,[29] T. Asakawa,[34] W. Ashmanskas,[16] M. Atac,[7] F. Azfar,[24] P. Azzi-Bacchetta,[23] N. Bacchetta,[23] W. Badgett,[18] S. Bagdasarov,[29] M. W. Bailey,[20] J. Bao,[37] P. de Barbaro,[28] A. Barbaro-Galtieri,[16] V. E. Barnes,[27] B. A. Barnett,[14] E. Barzi,[8] G. Bauer,[17] T. Baumann,[10] F. Bedeschi,[25] S. Behrends,[3] S. Belforte,[25] G. Bellettini,[25] J. Bellinger,[36] D. Benjamin,[33] J. Benlloch,[17] J. Bensinger,[3] D. Benton,[24] A. Beretvas,[7] J. P. Berge,[7] J. Berryhill,[5] S. Bertolucci,[8] B. Bevensee,[24] A. Bhatti,[29] K. Biery,[13] M. Binkley,[7] D. Bisello,[23] R. E. Blair,[1] C. Blocker,[3] A. Bodek,[28] W. Bokhari,[17] V. Bolognesi,[2] G. Bolla,[23] D. Bortoletto,[27] J. Boudreau,[26] L. Breccia,[2] C. Bromberg,[19] N. Bruner,[20] E. Buckley-Geer,[7] H. S. Budd,[28] K. Burkett,[18] G. Busetto,[23] A. Byon-Wagner,[7] K. L. Byrum,[1] J. Cammerata,[14] C. Campagnari,[7] M. Campbell,[18] A. Caner,[25] W. Carithers,[16] D. Carlsmith,[36] A. Castro,[23] D. Cauz,[25] Y. Cen,[28] F. Cervelli,[25] P. S. Chang,[31] P. T. Chang,[31] H. Y. Chao,[31] J. Chapman,[18] M. -T. Cheng,[31] G. Chiarelli,[25] T. Chikamatsu,[34] C. N. Chiou,[31] L. Christofek,[12] S. Cihangir,[7] A. G. Clark,[9] M. Cobal,[25] E. Cocca,[25] M. Contreras,[5] J. Conway,[30] J. Cooper,[7] M. Cordelli,[8] C. Couyoumtzelis,[9] D. Crane,[1] D. Cronin-Hennessy,[6] R. Culbertson,[5] T. Daniels,[17] F. DeJongh,[7] S. Delchamps,[7] S. Dell'Agnello,[25] M. Dell'Orso,[25] R. Demina,[7] L. Demortier,[29] B. Denby,[25] M. Deninno,[2] P. F. Derwent,[7] T. Devlin,[30] J. R. Dittmann,[6] S. Donati,[25] J. Done,[32] T. Dorigo,[23] A. Dunn,[18] N. Eddy,[18] K. Einsweiler,[16] J. E. Elias,[7] R. Ely,[16] E. Engels, Jr.,[26] D. Errede,[12] S. Errede,[12] Q. Fan,[27] C. Ferretti,[25] I. Fiori,[2] B. Flaugher,[7] G. W. Foster,[7] M. Franklin,[10]

M. Frautschi,[33] J. Freeman,[7] J. Friedman,[17] H. Frisch,[5] T. A. Fuess,[1] Y. Fukui,[15] S. Funaki,[34] G. Gagliardi,[25] S. Galeotti,[25] M. Gallinaro,[23] M. Garcia-Sciveres,[16] A. F. Garfinkel,[27] C. Gay,[10] S. Geer,[7] D. W. Gerdes,[14] P. Giannetti,[25] N. Giokaris,[29] P. Giromini,[8] G. Giusti,[25] L. Gladney,[24] D. Glenzinski,[14] M. Gold,[20] J. Gonzalez,[24] A. Gordon,[10] A. T. Goshaw,[6] K. Goulianos,[29] H. Grassmann,[25] L. Groer,[30] C. Grosso-Pilcher,[5] G. Guillian,[18] R. S. Guo,[31] C. Haber,[16] E. Hafen,[17] S. R. Hahn,[7] R. Hamilton,[10] R. Handler,[36] R. M. Hans,[37] K. Hara,[34] A. D. Hardman,[27] B. Harral,[24] R. M. Harris,[7] S. A. Hauger,[6] J. Hauser,[4] C. Hawk,[30] E. Hayashi,[34] J. Heinrich,[24] K. D. Hoffman,[27] M. Hohlmann,[5] C. Holck,[24] R. Hollebeek,[24] L. Holloway,[12] A. Hölscher,[13] S. Hong,[18] G. Houk,[24] P. Hu,[26] B. T. Huffman,[26] R. Hughes,[21] J. Huston,[19] J. Huth,[10] J. Hylen,[7] H. Ikeda,[34] M. Incagli,[25] J. Incandela,[7] G. Introzzi,[25] J. Iwai,[34] Y. Iwata,[11] H. Jensen,[7] U. Joshi,[7] R. W. Kadel,[16] E. Kajfasz,[23] H. Kambara,[9] T. Kamon,[32] T. Kaneko,[34] K. Karr,[35] H. Kasha,[37] Y. Kato,[22] T. A. Keaffaber,[27] L. Keeble,[8] K. Kelley,[17] R. D. Kennedy,[30] R. Kephart,[7] P. Kesten,[16] D. Kestenbaum,[10] R. M. Keup,[12] H. Keutelian,[7] F. Keyvan,[4] B. Kharadia,[12] B. J. Kim,[28] D. H. Kim,[7a] H. S. Kim,[13] S. B. Kim,[18] S. H. Kim,[34] Y. K. Kim,[16] L. Kirsch,[3] P. Koehn,[28] K. Kondo,[34] J. Konigsberg,[10] S. Kopp,[5] K. Kordas,[13] A. Korytov,[17] W. Koska,[7] E. Kovacs,[7a] W. Kowald,[6] M. Krasberg,[18] J. Kroll,[7] M. Kruse,[28] T. Kuwabara,[34] S. E. Kuhlmann,[1] E. Kuns,[30] A. T. Laasanen,[27] N. Labanca,[25] S. Lammel,[7] J. I. Lamoureux,[3] T. LeCompte,[1] S. Leone,[25] J. D. Lewis,[7] P. Limon,[7] M. Lindgren,[4] T. M. Liss,[12] N. Lockyer,[24] O. Long,[24] C. Loomis,[30] M. Loreti,[23] J. Lu,[32] D. Lucchesi,[25] P. Lukens,[7] S. Lusin,[36] J. Lys,[16] K. Maeshima,[7] A. Maghakian,[29] P. Maksimovic,[17] M. Mangano,[25] J. Mansour,[19] M. Mariotti,[23] J. P. Marriner,[7] A. Martin,[12] J. A. J. Matthews,[20] R. Mattingly,[17] P. McIntyre,[32] P. Melese,[29] A. Menzione,[25] E. Meschi,[25] S. Metzler,[24] C. Miao,[18] T. Miao,[7] G. Michail,[10] R. Miller,[19] H. Minato,[34] S. Miscetti,[8] M. Mishina,[15] H. Mitsushio,[34] T. Miyamoto,[34] S. Miyashita,[34] N. Moggi,[25] Y. Morita,[15] J. Mueller,[26] A. Mukherjee,[7] T. Muller,[4] P. Murat,[25] H. Nakada,[34] I. Nakano,[34] C. Nelson,[7] D. Neuberger,[4] C. Newman-Holmes,[7] M. Ninomiya,[34] L. Nodulman,[1] S. H. Oh,[6] K. E. Ohl,[37] T. Ohmoto,[11] T. Ohsugi,[11] R. Oishi,[34] M. Okabe,[34] T. Okusawa,[22] R. Oliveira,[24] J. Olsen,[36] C. Pagliarone,[2] R. Paoletti,[25] V. Papadimitriou,[33] S. P. Pappas,[37] N. Parashar,[25] S. Park,[7] A. Parri,[8] J. Patrick,[7] G. Pauletta,[25] M. Paulini,[16] A. Perazzo,[25] L. Pescara,[23] M. D. Peters,[16] T. J. Phillips,[6] G. Piacentino,[2] M. Pillai,[28] K. T. Pitts,[7] R. Plunkett,[7] L. Pondrom,[36] J. Proudfoot,[1] F. Ptohos,[10] G. Punzi,[25] K. Ragan,[13] D. Reher,[16] A. Ribon,[23] F. Rimondi,[2] L. Ristori,[25] W. J. Robertson,[6] T. Rodrigo,[25] S. Rolli,[25] J. Romano,[5] L. Rosenson,[17] R. Roser,[12] W. K. Sakumoto,[28] D. Saltzberg,[5] A. Sansoni,[8] L. Santi,[25] H. Sato,[34] P. Schlabach,[7] E. E. Schmidt,[7] M. P. Schmidt,[37] A. Scribano,[25] S. Segler,[7] S. Seidel,[20] Y. Seiya,[34] G. Sganos,[13] M. D. Shapiro,[16] N. M. Shaw,[27] Q. Shen,[27] P. F. Shepard,[26] M. Shimojima,[34]

M. Shochet,[5] J. Siegrist,[16] A. Sill,[33] P. Sinervo,[13] P. Singh,[26] J. Skarha,[14] K. Sliwa,[35] F. D. Snider,[14] T. Song,[18] J. Spalding,[7] T. Speer,[9] P. Sphicas,[17] F. Spinella,[25] M. Spiropulu,[10] L. Spiegel,[7] L. Stanco,[23] J. Steele,[36] A. Stefanini,[25] K. Strahl,[13] J. Strait,[7] R. Ströhmer,[7a] D. Stuart,[7] G. Sullivan,[5] A. Soumarokov,[31] K. Sumorok,[17] J. Suzuki,[34] T. Takada,[34] T. Takahashi,[22] T. Takano,[34] K. Takikawa,[34] N. Tamura,[11] F. Tartarelli,[25] W. Taylor,[13] P. K. Teng,[31] Y. Teramoto,[22] S. Tether,[17] D. Theriot,[7] T. L. Thomas,[20] R. Thun,[18] M. Timko,[35] P. Tipton,[28] A. Titov,[29] S. Tkaczyk,[7] D. Toback,[5] K. Tollefson,[28] A. Tollestrup,[7] J. F. de Troconiz,[10] S. Truitt,[18] J. Tseng,[14] N. Turini,[25] T. Uchida,[34] N. Uemura,[34] F. Ukegawa,[24] G. Unal,[24] J. Valls,[7a] S. C. van den Brink,[26] S. Vejcik, III,[18] G. Velev,[25] R. Vidal,[7] M. Vondracek,[12] D. Vucinic,[17] R. G. Wagner,[1] R. L. Wagner,[7] J. Wahl,[5] N. Wallace,[25] A. M. Walsh,[30] C. Wang,[6] C. H. Wang,[31] J. Wang,[5] M. J. Wang,[31] Q. F. Wang,[29] A. Warburton,[13] T. Watts,[30] R. Webb,[32] C. Wei,[6] C. Wendt,[36] H. Wenzel,[16] W. C. Wester, III,[7] A. B. Wicklund,[1] E. Wicklund,[7] R. Wilkinson,[24] H. H. Williams,[24] P. Wilson,[5] B. L. Winer,[21] D. Winn,[18] D. Wolinski,[18] J. Wolinski,[19] S. Worm,[20] X. Wu,[9] J. Wyss,[23] A. Yagil,[7] W. Yao,[16] K. Yasuoka,[34] Y. Ye,[13] G. P. Yeh,[7] P. Yeh,[31] M. Yin,[6] J. Yoh,[7] C. Yosef,[19] T. Yoshida,[22] D. Yovanovitch,[7] I. Yu,[7] L. Yu,[20] J. C. Yun,[7] A. Zanetti,[25] F. Zetti,[25] L. Zhang,[36] W. Zhang,[24] and S. Zucchelli[2]

[1] *Argonne National Laboratory, Argonne, Illinois 60439*

[2] *Istituto Nazionale di Fisica Nucleare, University of Bologna, I-40126 Bologna, Italy*

[3] *Brandeis University, Waltham, Massachusetts 02254*

[4] *University of California at Los Angeles, Los Angeles, California 90024*

[5] *University of Chicago, Chicago, Illinois 60637*

[6] *Duke University, Durham, North Carolina 27708*

[7] *Fermi National Accelerator Laboratory, Batavia, Illinois 60510*

[8] *Laboratori Nazionali di Frascati, Istituto Nazionale di Fisica Nucleare, I-00044 Frascati, Italy*

[9] *University of Geneva, CH-1211 Geneva 4, Switzerland*

[10] *Harvard University, Cambridge, Massachusetts 02138*

[11] *Hiroshima University, Higashi-Hiroshima 724, Japan*

[12] *University of Illinois, Urbana, Illinois 61801*

[13] *Institute of Particle Physics, McGill University, Montreal H3A 2T8, and University of Toronto, Toronto M5S 1A7, Canada*

[14] *The Johns Hopkins University, Baltimore, Maryland 21218*

[15] *National Laboratory for High Energy Physics (KEK), Tsukuba, Ibaraki 305, Japan*

[16] *Ernest Orlando Lawrence Berkeley National Laboratory, Berkeley, California 94720*

[17] *Massachusetts Institute of Technology, Cambridge, Massachusetts 02139*

[18] *University of Michigan, Ann Arbor, Michigan 48109*

[19] *Michigan State University, East Lansing, Michigan 48824*

[20] *University of New Mexico, Albuquerque, New Mexico 87131*
[21] *The Ohio State University, Columbus, OH 43210*
[22] *Osaka City University, Osaka 588, Japan*
[23] *Universita di Padova, Istituto Nazionale di Fisica Nucleare, Sezione di Padova, I-35131 Padova, Italy*
[24] *University of Pennsylvania, Philadelphia, Pennsylvania 19104*
[25] *Istituto Nazionale di Fisica Nucleare, University and Scuola Normale Superiore of Pisa, I-56100 Pisa, Italy*
[26] *University of Pittsburgh, Pittsburgh, Pennsylvania 15260*
[27] *Purdue University, West Lafayette, Indiana 47907*
[28] *University of Rochester, Rochester, New York 14627*
[29] *Rockefeller University, New York, New York 10021*
[30] *Rutgers University, Piscataway, New Jersey 08854*
[31] *Academia Sinica, Taipei, Taiwan 11529, Republic of China*
[32] *Texas A&M University, College Station, Texas 77843*
[33] *Texas Tech University, Lubbock, Texas 79409*
[34] *University of Tsukuba, Tsukuba, Ibaraki 305, Japan*
[35] *Tufts University, Medford, Massachusetts 02155*
[36] *University of Wisconsin, Madison, Wisconsin 53706*
[37] *Yale University, New Haven, Connecticut 06511*

# Appendix B

# A Compilation of Particle Physics and CDF Terminology

**Beam constrained fit** The beam position in the transverse plan of the CDF detector is known better than 50 $\mu m$ on a run by run basis. This information if added to the CTC track fit improves the CTC track momentum resolution by 100%.

**CDF** The Collider Detector at Fermilab.

**CEM** The Central Electromagnetic Calorimeter.

**CES** The Central Electron Strip Chambers.

**CHA** The Central Hadron Calorimeter.

**CMP** The Central Muon Upgrade Chambers.

**CMX** The Central Muon Extension Chambers.

**CMU** The Central Muon Chambers.

**CTC** The Central Tracking Chamber.

**Depth of the Calorimeter** A measure of the amount of material of the calorimeter in the direction of the incident particle (or particles). The electromagnetic calorimeter is characterized by the radiation length, which is the mean distance over which a high energy electron loses all but $\frac{1}{e}$ of its energy. The hadronic calorimeter is measured by the interaction length, and is the corresponding variable for high energy hadrons. The depth of the calorimeter is just the number of radiation length or interaction length. Since the showers (EM or hadronic) is characterized by their tail and large flunctuation in the energy at the tail, the adequate depth of the calorimeter is important for both the linearity and the resolution of the calorimeter's energy response.

**DIS** Deep inelastic scattering.

**EM** Electromagnetic.

**EGS** A Monte Carlo program which similates electron and photon showers in the material.

**FEM** The Forward Electron Calorimeter.

**PDFs** Parton Density Functions, the parameterized distributions of momentum densities of constituent quarks and gluons in a hadron.

**PEM** The Plug Electron Calorimeter.

**FHA** The Forward Hadron Calorimeter.

**Fiducial** The geometric region of a detector where the normal performance is expected.

**FMU** The Forward Muon Chambers.

**Integrated Luminosity** A measure of the total number of collisions that have occurred during the run.

**Interaction Length** See **depth of the calorimeter**.

**Minimum Ionizing Particle** The ionization energy loss by heavy particles is a function of the speed of particles. When the speed reaches a certain value, the energy loss reaches its minimum (minimum ionization). In practical cases, most relativistic particles (e.g., cosmic-ray muons) have energy loss rate close to the minimum, and are said to be minimum ionization particles, or mips.

**MIP** Minimum ionizing particle.

**PES** The Plug Electron Strip Detector.

**Primary $Z$ Vertex** The $Z$ vertex where particles from the $p\overline{p}$ collisions of interest originate.

**Ratiation Length** See **depth of the calorimeter**.

**Run 1A** Tevatron Run during period of 1992-1993. A total of $\approx$ $88pb^{-1}$ data are colloected at CDF.

**Run 1B** Tevatron Run during period of 1994-1995. A total of $\approx$ $20pb^{-1}$ data are colloected at CDF.

**The Standard Model** The collection of theories describing the electromagnetic, weak and strong interactions between particles, including Quantum Chromodynamics (QCD), the Glashow-Weinberg-Salam theory of electroweak processes.

**SVX** The Silicon Vertex Detector.

**Tower** The calorimeters in a hadron experiment is usually segmented in the $\eta - \phi$ space, and in a projective manner logitudinally. Each element is called a tower.

**Tracking** Charged particles lose energy in the material it traverses (ionization energy loss). The energy loss is localized along the particle track. Experimentalists construct tracking devices to detect the location of the energy loss thereby reconstructing the particle track. This process is called tracking.

**Track Finding Efficiency** A measure of probability of reconstructing a particle track.

**Trigger** The set of conditions for selecting physics events of interest.

**VTX** The Vertex Time Projection Chambers.

**WHA** The Wall Hadron Calorimeter.